Progress in Materials Science 165 (2027) 101865

Contents lists available at ScienceDirect

Progress in Materials Science

journal homepage: www.elsevier.com/locate/pmatsci

Snapshot Reviews in Emerging Fields

From embrittlement to enhancement: pathway toward using hydrogen as a beneficial interstitial solute element in austenitic steels

Vahid Javaheri [a,*], Mahsa Barati Mahyari [a], Mohammad Moallemi [a], Pentti Karjalainen [a], Lisa Claeys [b], Liese Vandewalle [b], Rebecca Janisch [c], Hosni Idrissi [d], Yuhei Ogawa [e], Jukka Kömi [a], Kim Verbeken [b]

[a] Materials and Mechanical Engineering, Centre for Advanced Steels Research, University of Oulu, P.O. Box 3000, Oulu, FIN-90014, Finland
[b] Ghent University, Department of Materials, Textiles and Chemical Engineering, Research Group of Sustainable Materials Science, Technologiepark 46, Zwijnaarde, 9052, Belgium
[c] Interdisciplinary Centre for Advanced Materials Simulations (ICAMS), Ruhr-University Bochum, Bochum, 44801, Germany
[d] Institute of Mechanics, Materials and Civil Engineering, UCLouvain, Louvain-la-Neuve, B-1348, Belgium
[e] Research Center for Structural Materials, National Institute for Materials Science (NIMS), 1-2-1 Sengen, Tsukuba, 305-0047, Japan

ARTICLE INFO

Keywords:
Hydrogen embrittlement
Hydrogen-enhanced plasticity
Austenitic steels
Stacking fault energy
Twinning

ABSTRACT

Hydrogen has long been regarded as a detrimental interstitial element in metallic alloys, primarily owing to its role in hydrogen embrittlement. However, recent experimental and computational studies, principally involving austenitic steels including Fe–Cr–Ni stainless steels, high-Mn TWIP alloys, and low-density steels (alloyed with aluminum) have revealed that hydrogen can, under carefully controlled conditions of alloy composition, microstructure, stacking fault energy, and hydrogen concentration, act as a functional and beneficial interstitial solute element that can enhance strength, ductility, or even both. This review critically examines the fundamental mechanisms underlying this paradoxical yet promising behavior, with particular emphasis on hydrogen-enhanced twinning, hydrogen-enhanced densified twinning, hydrogen-enhanced microbanding, and hydrogen solid-solution strengthening. The roles of stacking fault energy, grain size, precipitation (κ-carbide, B2 intermetallic), and hydrogen charging protocol (electrochemical vs. gaseous charging; pre-charging vs. in-situ) on the operative mechanism and net mechanical response are systematically discussed. A key conclusion is that the transition from hydrogen embrittlement to hydrogen-enhanced mechanical properties is governed by a multi-dimensional parameter space that has not yet been fully mapped. These findings provide a scientific basis for a conceptual reorientation in designing alloy compositions and microstructures that may promote beneficial hydrogen–defect interactions under controlled or even in-service hydrogen exposure while suppressing embrittlement.

1. Introduction

Hydrogen has been regarded as a detrimental element in metallic systems, in which its interaction with the microstructure can

* Corresponding author.
E-mail address: Vahid.javaheri@oulu.fi (V. Javaheri).

https://doi.org/10.1016/j.pmatsci.2026.101865
Received 19 February 2026; Received in revised form 10 October 2026; Accepted 12 October 2026
Available online 15 October 2026
0079-6425/© 2026 The Author(s). Published by Elsevier Ltd. This is an open access article under the CC BY license (http://creativecommons.org/licenses/by/4.0/).

Nomenclature

AFM	atomic force microscopy
AM	additive manufacturing
APT	atom probe tomography
ASS	austenitic stainless steel
at.ppm	atomic parts per million
B2	ordered body-centered cubic intermetallic phase
BCC	body-centered cubic
BF-STEM	bright-field scanning transmission electron microscopy
CG	coarse-grained
CTS	critical twinning stress
DB	omain Boundary
DDW	dense dislocation wall
DFT	density functional theory
DIC	digital image correlation
DO_3	ordered Fe_3Al-type intermetallic crystal structure
E_A	activation energy
E_B	binding energy
EBSD	electron backscatter diffraction
EC	electrochemical charging
ECCI	electron channeling contrast imaging
E_T	trapping energy
FCC	face-centered cubic
FG	fine-grained
GB	grain boundary
GNB	geometrically necessary boundary
GND	geometrically necessary dislocation
GS	grain size
HAA	hydrogen-affected area
HCP	hexagonal close-packed crystal structure
HE	hydrogen embrittlement
HEA	high-entropy alloy
HEDB	hydrogen-enhanced deformation banding
HEDE	hydrogen-enhanced decohesion
HEDT	hydrogen-enhanced densified twinning
HEH	hydrogen-enhanced hardening
HEI	hydrogen embrittlement index
HELP	hydrogen-enhanced localized plasticity
HEMB	hydrogen-enhanced microbanding
HEP	hydrogen-enhanced plasticity
HET	Hydrogen-enhanced twinning
HIPT	hydrogen-induced phase transformation
HISC	hydrogen in-situ charging
HPC	hydrogen pre-charging
HPG	high-pressure gaseous hydrogen charging
HPT	high-pressure thermal charging
IDB	incidental dislocation boundary
IG	intergranular fracture mode
L1	ordered FCC intermetallic
MB	microband
MBIP	microband-induced plasticity
MEA	medium-entropy alloy
QC	quasi-cleavage
R	universal gas constant
SFE	stacking fault energy
SFP	stacking fault probability
SPD	shockley partial dislocation
SSRT	slow strain rate tensile
TEM	transmission electron microscopy

TRIP	transformation-induced plasticity
TWIP	twinning-induced plasticity
UFG	ultra-fine-grained
UTS	ultimate tensile strength
WBDF	weak-beam dark-field
w.ppm	weight parts per million
XRD	X-ray diffraction
YS	yield strength
α'	body-centered cubic martensite
ε	hexagonal close-packed martensite
κ-carbide	Kappa carbide
γ	austenite phase.

cause undesired embrittlement. In steel physical metallurgy, it also has long been regarded as a harmful interstitial element. Its presence is linked to a wide range of mechanical degradation phenomena, notably hydrogen embrittlement (HE) [1,2], hydrogen-induced cracking [3], and hydrogen-assisted stress corrosion cracking [4]. These effects are especially noticeable in body-centered cubic (BCC) steels such as martensitic and ferritic grades due to their low hydrogen solubility and high diffusion rates, which promote the rapid local segregation of hydrogen at microstructural defects, leading to (quasi-) cleavage, delayed fracture, or intergranular early and premature failure [5].

In contrast to BCC steels, austenitic face-centered cubic (FCC) steels, including Fe-Cr-Ni austenitic stainless steels and high-Mn austenitic steels (Fe–Mn–C–Al–and/or Si), show higher hydrogen solubility and lower diffusivity, mostly due to their denser atomic packing and larger octahedral interstitial sites that modify how hydrogen interacts with their microstructure [5]. This reduces the risk of HE in FCC materials, though they are not immune to hydrogen-related damage and degradation [6]. Unexpected crack initiation has been observed for hydrogen-charged (H-charged) FCC steels at features such as deformation twin boundaries, phase and precipitate interfaces, and grain boundary junctions [6]. Many studies have reported hydrogen-facilitated premature fracture in twinning-induced plasticity (TWIP) steels, often showing transitions from ductile to brittle fracture modes [7–10]. A foundational work by Louthan et al. [11] systematically demonstrated that hydrogen absorption substantially reduces tensile ductility in austenitic stainless steels (ASS), e.g., Cr–Ni grades 304 and 316, even at relatively low bulk hydrogen concentrations. The degradation was attributed to hydrogen-enhanced dislocation mobility and localized plasticity near stress concentrators.

In general, the principal embrittlement mechanisms include: i) Hydrogen-Enhanced Decohesion (HEDE) [12], meaning the weakening of interatomic bonding particularly along grain boundaries, where hydrogen can segregate, ii) Hydrogen-Enhanced Localized Plasticity (HELP) [13], wherein dislocation motion potentially becomes faster (via shielding of the elastic stress field by a hydrogen atmosphere) and unstable, leading to highly localized stress, accelerated void formation and coalescence, and early failure, iii) Hydrogen-Induced Phase Transformations (HIPT) [14], where ε-martensite or α′-martensite formation acts as crack initiation sites, iv) Strain localization near defects [14], where hydrogen stabilizes excessive vacancies or dislocation pile-ups, leading to microvoids coalescence, hydride formation or local lattice dilatation, though uncommon in FCC steels, where local hydride-like phases or expansion zones may act as crack nucleation sites.

However, some recent studies have unexpectedly revealed a contrasting trend in certain FCC systems where hydrogen can, under well-defined conditions, act as a ductility or even strength enhancer, or sometimes both [15–28]. For example, hydrogen has been shown to increase both ductility and strength in a lightweight (Fe–1C–25Mn–5.5Al–3Si) TWIP steel (all compositions in wt.% unless stated otherwise) by altering stacking fault energy (SFE) and promoting plasticity mechanisms such as mechanical twinning [28]. The key factor was the optimized SFE of $\sim 49.5\ mJ/m^2$, which was slightly reduced by hydrogen, allowing enhanced surface twin formation due to higher hydrogen content at the surface, while avoiding embrittlement.

In this context, an early report of a positive effect of hydrogen on mechanical properties came from Astafurova et al. [26] (year 2010), who observed that H-charged single crystals of Hadfield steel (Fe–13Mn–1C) showed increased ductility under tensile loading along the $< 001 >$ axis at 77 and 300 K. The mechanism was attributed to hydrogen-promoted deformation twinning, which allowed greater elongation prior to fracture. This concept was later extended from single crystal to polycrystalline structures by Yamada et al. [27] (year 2015), who showed that Fe–30Mn–6Al alloys pre-charged with hydrogen exhibited improved elongation and enhanced work-hardening, linked to a hydrogen-induced reduction in SFE and promotion of twinning. Later, the same phenomenon was reported for an FCC high entropy alloy [20,23]. This was significant because it extended the concept of hydrogen-enhanced plasticity from austenitic steel systems to the developing class of complex concentrated alloys. Ogawa et al. [25] (year 2020) were the first to describe the concept of solute hydrogen as an alloying element after observing an improved strength-ductility balance in a Fe–24Cr–19Ni austenitic steel at ambient temperature. More recently (year 2025), Ito et al. [21] reported that solute hydrogen has a minimal influence on the evolution of dislocation structures in the same Fe–24Cr–19Ni steel, even at hydrogen concentrations as high as ~ 7600 at.ppm. They found that deformation twinning initiated at a lower strain in the H-charged condition compared to the H-free state. The increase in flow stress resulting from hydrogen-induced solid-solution strengthening was proposed as the main driving factor for this accelerated twin activation. Consequently, the earlier onset of twinning enhances the work-hardening rate at intermediate to large strains, delaying plastic instability, and leading to improved uniform elongation.

Beyond these pioneering works, several additional studies have further expanded our understanding of the mechanistic landscape of hydrogen–austenite interactions. Gutierrez-Urrutia et al. [24] reported that in a Fe–Mn–Al–C low-density austenitic steel, hydrogen

promoted the formation of denser microband (MB) arrays and, critically, improved the resistance to HE by redistributing plastic strain more homogeneously. Kong et al. [22] employed in-situ neutron diffraction during tensile testing to directly observe the influence of hydrogen on deformation mechanisms in high-Mn steels over a broad range of SFEs. Their results demonstrated that the transition from hydrogen-enhanced plasticity to embrittlement is gradual rather than abrupt, and that the stacking fault probability (SFP), not just bulk-averaged SFE, is also a controlling parameter. Cho et al. [29] similarly used neutron diffraction and diffraction line profile analysis to show that hydrogen promotes dislocation cell refinement and suppresses dynamic strain aging in a high-Mn austenitic steel, contributing to improved work-hardening under specific charging conditions. Collectively, these studies establish that hydrogen-enhanced plasticity is a robust and reproducible phenomenon, not an isolated experimental artifact.

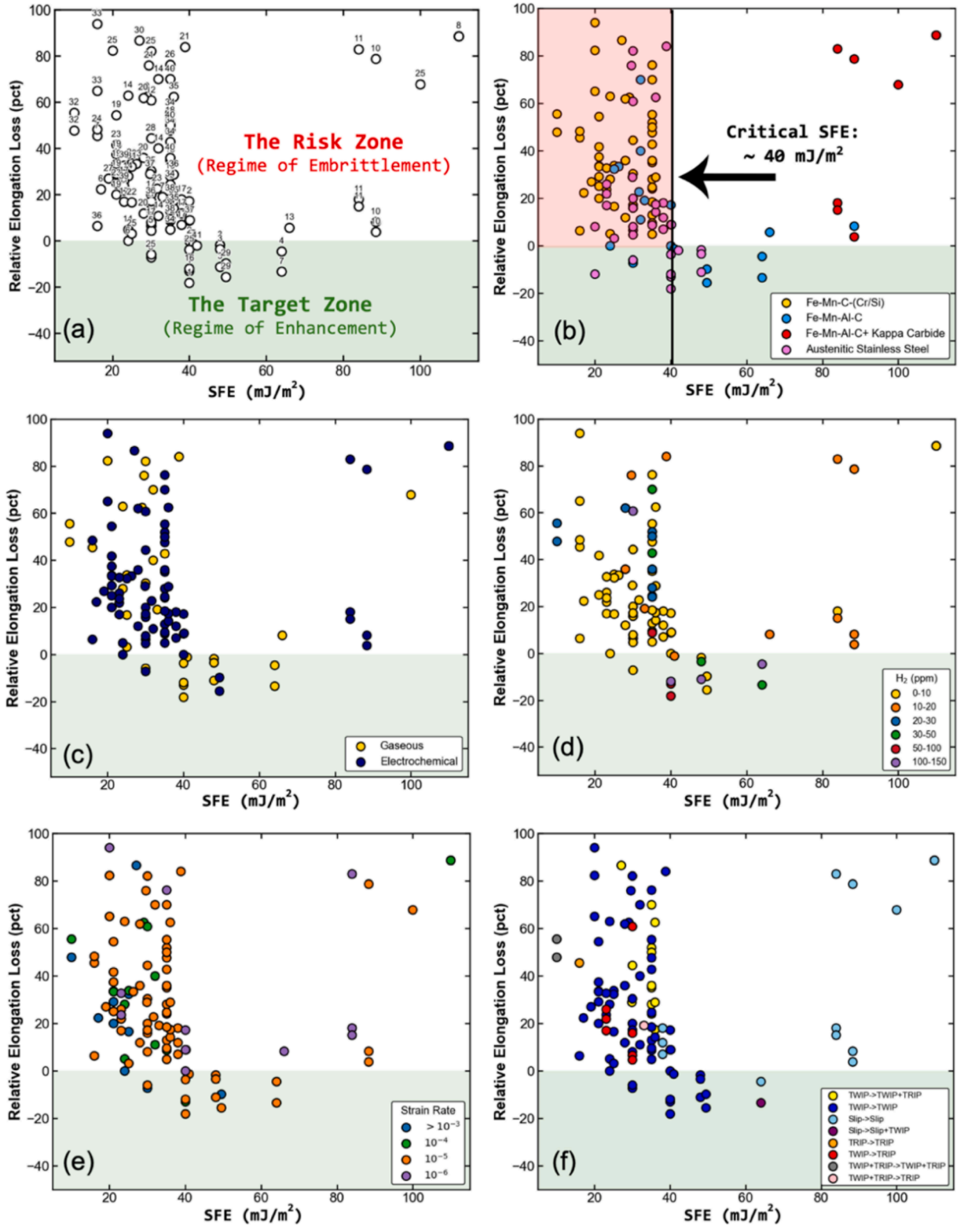
This duality, acting as an embrittling cause in some alloys while enhancing ductility in others, may represent a shift in alloy design strategy. The underlying mechanisms proposed for this ductility enhancement are: i) Hydrogen-Enhanced Twinning (HET) [28] and Hydrogen-Enhanced Densified Twinning (HEDT) [30], where hydrogen increases the number and density of twins, improving work-hardening, ii) Hydrogen-Enhanced Deformation Banding (HEDB) [31] and iii) Hydrogen-Enhanced Microbanding (HEMB) [24], where hydrogen boosts the activity of dislocation slip bands, refining deformation structures, and iv) Hydrogen-Enhanced Hardening (HEH) [17], in which hydrogen occupies lattice interstitial sites and contributes to strength enhancement through solid-solution effects, rather than primarily promoting lattice defects or damage precursors.

However, as demonstrated in Fig. 1, this ductility enhancement is not universal; rather, the response of austenitic steels to hydrogen depends critically on alloy composition, charging condition, strain rate, hydrogen content, and particularly on SFE, a key microstructural parameter and a thermodynamic descriptor that governs the activation of deformation twinning, dislocation cross-slip, and ε- or α'-martensitic transformation [22,32,33]. In high-SFE steels, when hydrogen moderately reduces SFE, deformation twinning can be promoted, enhancing ductility. However, when SFE after hydrogen absorption/charging drops below a critical threshold (around 20 mJ/m2), the steel becomes prone to strain-induced martensitic transformation, a main trigger for crack initiation and HE [34]. This dependency of hydrogen effect on tensile properties of presented dataset against the SFE is illustrated in Fig. 1**a**, where hydrogen-affected relative elongation loss in FCC steels is shown across a broad range of SFEs. The elongation loss is further categorized according to Fig. 1**: b)** composition family, **c)** charging method, **d)** absorbed hydrogen content, **e)** strain rate, and **f)** correlated change in main deformation mechanism. Fig. 1 suggests that SFE provides a useful first-order framework for distinguishing the regime of hydrogen-assisted ductility ("The Target Zone", Regime of Enhancement shaded in green) from a regime associated with increased susceptibility to HE ("The Risk Zone"). In systems where SFE is tuned appropriately, and twins can become additional carriers of plasticity, hydrogen can suppress strain localization, promote more uniform deformation, and extend elongation to failure. This behavior is particularly observed in certain highly alloyed FCC materials with modified microstructures that helps maintain relatively high SFE. The different categories and trends highlighted in Fig. 1 will be referred to and discussed in more detail in later sections.

Fig. 2 illustrates the general evolving understanding of how hydrogen acts as a functional solute element by schematically connecting hydrogen concentration to the mechanical performance of an FCC alloy in a Cr–Mn–Fe–Co–Ni system, reproduced from the experimental results reported in Ref. [23]. Beginning from the H-free baseline, moderate hydrogen charging can cause simultaneous increases in both ultimate tensile strength (UTS) and elongation, indicating a regime of hydrogen-enhanced plasticity (HEP). At certain hydrogen concentrations, the total elongation reaches an optimum point where the strength–ductility balance is maximized. With further hydrogen uptake, the positive effect gradually decreases, and mechanical performance eventually begins to deteriorate. The related fracture morphologies highlight the microstructural features of this transition from conventional HE to hydrogen-assisted plastic deformation. These findings raise a key question about the mechanisms that control hydrogen's beneficial influence in austenitic steels and how particular alloy system and microstructural conditions can shift the balance from embrittlement toward improved plasticity. Addressing this question forms the conceptual link to the objectives of the present review.

Within this context, it is important to clarify how hydrogen and its effect are described throughout this review. The term "functional interstitial solute element" is used specifically to describe hydrogen's demonstrated, condition-dependent capacity to modify dislocation kinetics, stacking-fault stability, and solid-solution strengthening in a way that can be net beneficial to strength and/or ductility under defined charging and testing conditions. This framing does not imply that hydrogen can be treated as a permanent, stable alloying addition similar to C or N; rather, it reflects hydrogen's higher mobility and reversibility, which distinguish it mechanistically from conventional interstitial solutes (**Section 4.4**) while still allowing its effect to be engineered through alloy composition, SFE, and microstructure. This distinction is also important when interpreting HEP from a mechanistic perspective. HEP is not proposed as a fundamentally new hydrogen-mediated mechanism that contradicts HELP. Rather, HELP-type hydrogen–dislocation interactions may still operate locally, while the surrounding microstructure determines whether their macroscopic consequence is enhanced plasticity or embrittlement (**Section 4**).

On this basis, this work aims to critically examine the fundamental mechanisms by which hydrogen affects deformation behavior and the strength–ductility relationship in austenitic steels, with particular emphasis on conditions under which hydrogen may promote enhanced plasticity rather than conventional embrittlement. We systematically discuss these mechanisms and assess recent progress in hydrogen–austenite interactions that can contribute to improved mechanical properties. It should be noted that several comprehensive reviews [1,3,5,6,14,35] have already addressed the embrittlement mechanisms in metals and steels. Therefore, the present work deliberately avoids repeating those discussions in detail and instead focuses, as much as possible, on the beneficial aspects of hydrogen. Accordingly, this work is a targeted critical review rather than a formal systematic or exhaustive review and any apparent boundaries or frequency of detrimental/beneficial response shown here should be interpreted within the selected dataset; the literature-search, screening, and study-selection procedures are detailed in Supplementary Section S1. In doing so, we aim to identify the alloy compositions, microstructures, and exposure conditions under which interstitial hydrogen may improve mechanical performance without activating dominant embrittlement pathways.



(caption on next page)

Fig. 1. Hydrogen affected relative elongation loss of FCC steels across (a) a wide range of stacking fault energy categorized according to (b) composition family, (c) charging method, (d) hydrogen content, (e) applied strain rate, and (f) changes in deformation mechanisms. Fig. 1 is constructed from 106 individual data points extracted from 39 independent studies according to the method described in **Supplementary 1**. Since the data showing elongation loss were purposively selected to represent a wide range of material families and SFE, the trend observed here should be interpreted as specific to this selected dataset, whereas all identified eligible studies reporting beneficial or minimal hydrogen effects were included comprehensively. The numerical labels assigned to each data point in Fig. 1a correspond to the associated reference numbers listed in **Supplementary 2**.

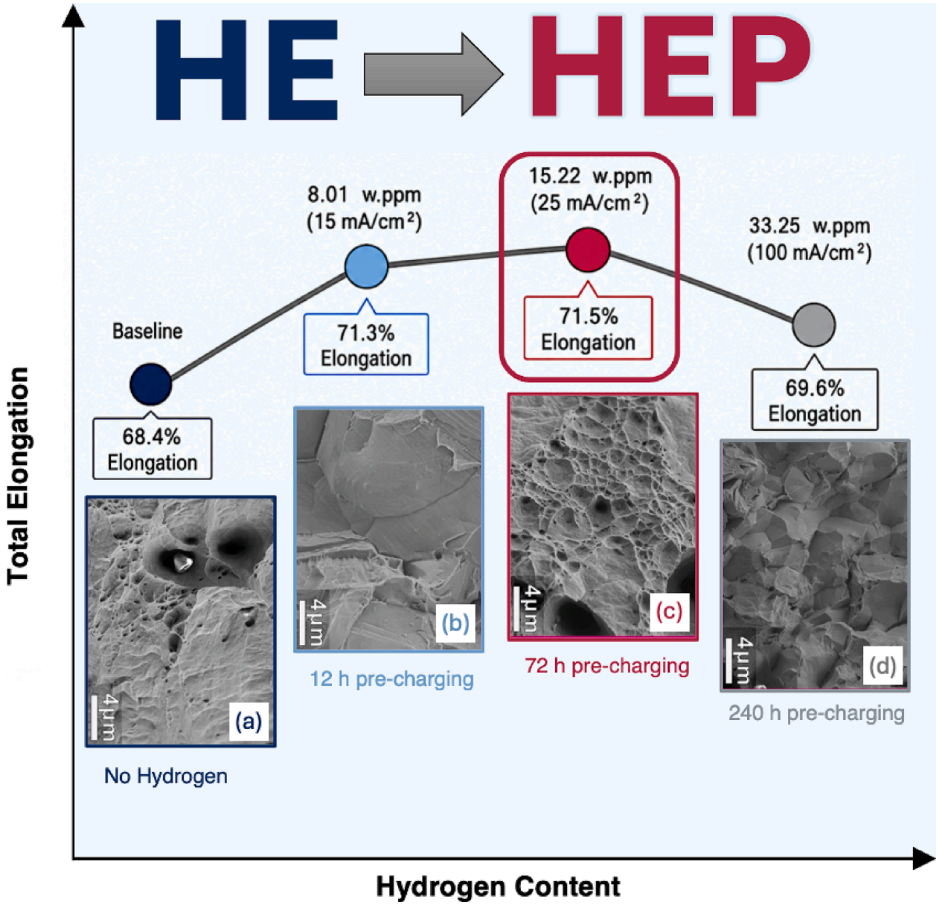


Fig. 2. Schematic representation of the pathway from Hydrogen Embrittlement to Hydrogen-Enhanced Plasticity: Images of fractured Cr–Mn–Fe–Co–Ni HEA samples after in-situ tensile testing under various hydrogen charging conditions. (a) Ductile dimpled fracture morphology for samples without hydrogen. (b–d) shows samples fractured after hydrogen pre-charging conditions of 12 h at 15 mA/cm^2, 72 h at 25 mA/cm^2, and 240 h at 100 mA/cm^2, respectively. Created based on the results reported by Luo et al. [23].

To address this aim, the review is organized to move from phenomenology to mechanism and finally to future perspectives. **Section 2** summarizes the fundamental interactions between hydrogen and FCC austenitic lattices, including hydrogen solubility, diffusion, trapping, and the role of alloy chemistry. **Section 3** discusses the dual effect of hydrogen on slow strain-rate tensile properties and establishes experimental evidence for both hydrogen embrittlement and hydrogen-enhanced plasticity. **Section 4** examines the main mechanisms proposed for hydrogen-assisted property enhancement, including hydrogen-enhanced twinning, densified twinning, deformation banding, microbanding, and solid-solution hardening. **Section 5** evaluates the microstructural sensitivity of these mechanisms, with emphasis on grain size, κ-carbides, and B2 precipitates that may either support plasticity or trigger damage. **Section 6** addresses the role of experimental protocol, including charging routes, gaseous versus electrochemical charging as well as in-situ and ex-situ methods, which are essential for comparing literature data. Finally, the review closes with a discussion of opportunities and future research direction s (Section 7), highlighting key knowledge gaps, emerging experimental and computational approaches, and alloy-design strategies for better understanding how to shift hydrogen–austenite interactions from embrittlement toward controlled plasticity enhancement.

2. Hydrogen in austenitic systems: states, mobility, and interactions

2.1. Hydrogen solubility and segregation

Hydrogen solubility and segregation behavior are foundational to understanding its influence on the mechanical response of austenitic steels. In contrast to BCC alloys, where hydrogen solubility is low, but mobility is high, austenitic alloys offer high solubility but kinetically limited hydrogen mobility. In FCC austenite, hydrogen may exist either as an interstitial solute within the austenite lattice or become enriched at microstructural defects and heterogeneities. These include FCC-relevant planar defects, such as stacking faults and twin boundaries, as well as more general hydrogen-trapping sites in crystalline metals, such as grain boundaries, phase interfaces, vacancies, and precipitate/matrix interfaces. In this context, rather than treating hydrogen only in terms of reversible and irreversible trapping, which is strongly dependent on time and hydrogen mobility, it is more appropriate to distinguish between weak, moderate and strong hydrogen segregation sites according to their binding energy, defect density and ability to locally enrich hydrogen.

As an interstitial in FCC austenite, hydrogen preferentially occupies octahedral sites [1]. This lattice hydrogen should be regarded as the reference solid-solution state rather than as a microstructural trap. The amount of hydrogen dissolved in the lattice (i.e., solubility) is governed by the hydrogen chemical potential, temperature, charging/exposure condition, alloy chemistry, and the strain field associated with interstitial hydrogen. Alloying elements such as Mn, Ni, Al, and C can modify hydrogen solubility by changing the lattice parameter, local chemical environment, austenite stability, and SFE [36–38].

Hydrogen segregation/trapping occurs when atomic hydrogen is immobilized and becomes enriched at microstructural heterogeneities. These sites differ widely in binding energy (E_B). Weak segregation sites, such as the austenite lattice or coherent low-misfit interfaces, have relatively low binding energies and mainly influence the apparent solubility and short-range redistribution of hydrogen. Moderate sites, including dislocations, grain boundaries and γ/ε or γ/α' phase interfaces, can increase local hydrogen concentration and influence deformation mechanisms such as hydrogen-enhanced localized plasticity, planar slip, twinning, or martensitic transformation. Strong segregation sites, including twin boundaries, vacancy clusters, void-like defects and some carbide

Table 1
Summary of main hydrogen-segregation sites and hydrogen–microstructure interactions in austenitic steels.

Trap Type	Trapping/ Detrapping energy (E_T), eV	Binding Energy (E_B), eV	Note	Ref.
FCC austenite lattice (weak lattice-related traps/ octahedral interstitial sites)	Not a true trap	0.08–0.2	Hydrogen occupies mainly octahedral interstitial sites in the FCC austenite lattice. This should be treated as the reference lattice solution state, not as a microstructural trap.	[43,44]
Dislocations (average/ mixed population)	0.20–0.35	0.14–0.27	Ref. [45] calculated hydrogen binding energy of dislocations in austenitic stainless steel using a local equilibrium model to be 0.27 eV. Ref. [46] experimentally measured a hydrogen– dislocation binding energy of 0.14 eV in Fe–18Cr–Ni alloy.	[45–48]
Dislocation core	0.50–0.60	–	This is more often from general iron/steel data than direct FCC-austenite measurement.	[47,49]
Dislocation elastic strain field	~0.29	–	This is more often from general iron/steel data than direct FCC-austenite measurement.	[50,51]
Grain boundaries (FCC systems)	0.18–0.26	0.27–0.47	Boundary character is very important. In general, ordered/low-misorientation boundaries can have a higher trap energy, while high-angle random boundaries with relatively low binding may act as diffusion paths. Higher E_T values of ~ 0.30–0.50 eV are also reported, especially in BCC systems like pure iron [52,53].	[47,54,55]
Coherent twin boundaries, Σ3 / deformation twins	0.62–0.83	0.64	Binding energy for twin boundaries is often reported as detrapping/binding-type energy.	[55–57]
ε-Martensite Interfaces (HCP-FCC interfaces)	~0.23	–	For the γ/α' martensite interface, E_T is reported to be around 0.36 eV [47].	[53,58,59]
Precipitates & carbides (interface)	0.11–0.35	0.04–0.20	Values depend strongly on carbide type, coherency, carbon vacancies, and interface structure. Ref. [39] reported the hydrogen trapping by a wide range of different carbides.	[39,47]
Precipitates & carbides (vacancies at the interface)	0.40–0.94	0.03–1.38	See the note for precipitates & carbides (Interface)	[39,47]
Precipitates & carbides (strain field)	0.10–0.24	0.12–0.24	See the note for precipitates & carbides (Interface)	[39,47]
Vacancies (monovacancy–H)	–	~0.23–0.29 (per H atom)	Up to six H atoms can be trapped by one monovacancy.	[60–62]
Vacancy clusters (void-like defects)	0.50–0.7	0.50–0.70	Should be separated from isolated monovacancies. These are deeper traps and closer to irreversible trapping behavior.	[47,60–62]
B2 phase (vacancies at the interface)	~0.55	–	B2-NiAl located close to the precipitate/matrix interface contribute to the deep trapping of hydrogen (~50 kJ/mol). In general, coherent B2-NiAl precipitates with low misfit have limited trapping capability (trapping energy of around 0.17 eV).	[47]

or precipitate interfaces, can retain higher local hydrogen concentrations and may either reduce long-range hydrogen mobility or promote local decohesion and crack initiation, depending on their density, morphology and spatial distribution [1,39].

Traps are classified by their E_B and trapping or detrapping energy (E_T). These energies govern hydrogen mobility and play a critical role in determining whether hydrogen facilitates deformation (e.g., via dislocation shielding) or causes embrittlement (e.g., by aiding decohesion or promoting martensite). Usually, traps with an E_B of 0.2–0.5 eV are considered weak traps and those with E_B above 0.5 eV are strong traps [1]. The classic Oriani equilibrium model [40] and kinetic trapping models such as the McNabb–Foster/Krom formulations [41,42] provide useful frameworks for describing hydrogen partitioning between lattice and trap sites. However, as mentioned before, the terms reversible and irreversible should be used cautiously, because apparent reversibility depends on temperature, timescale, heating rate in thermal desorption spectroscopy, as well as specimen thickness and hydrogen chemical potential. In this work, trap sites are therefore classified mainly by their approximate binding or detrapping energies, as summarized in Table 1, while recognizing that the measured values may vary depending on experimental methods and microstructural state.

It is also important to distinguish between E_B and E_T, because these quantities are sometimes used interchangeably in the literature. As schematically presented in Fig. 3, E_B describes the energetic preference for hydrogen to occupy a trap site rather than a normal lattice interstitial site; in other words, it represents the energy difference between the trapped state and the lattice solid-solution state. A higher E_B therefore indicates a stronger tendency for hydrogen segregation at that microstructural feature. By contrast, E_T is the energy required to release hydrogen from a trap site and allow it to return to lattice diffusion. In the energy description used by Bestaute et al. [47], E_T includes both the binding energy E_B and the activation energy (E_A) required for hydrogen to jump between the lattice and the trap, so that $E_T = E_B + E_A$. Therefore, E_T values obtained from thermal desorption spectroscopy or permeation modeling should not always be directly compared with calculated E_B values unless the definition and reference state are clearly specified.

As listed in Table 1, several compositional and microstructural features can affect hydrogen trapping behavior:

- *Dislocation Density*: Cold working or deformation increases the dislocation density and therefore the density of moderate hydrogen segregation sites. Hydrogen associated with dislocation cores and strain fields can promote localized slip and dislocation mobility, consistent with HELP-type mechanisms, while also reducing long-range hydrogen transport by increasing the number of available trapping/segregation sites [45–48].
- *Grain Boundaries*: Grain boundaries in austenitic steels act as moderate hydrogen segregation sites, but their role depends strongly on boundary character, local chemistry and stress state. Random high-angle boundaries, special boundaries and solute-decorated boundaries may show different segregation behavior. At high local hydrogen activity, grain boundary segregation can promote decohesion and intergranular cracking, particularly when combined with strain localization or impurity segregation [47,54,55,63].
- *Twin Boundaries*: Coherent twin boundaries and deformation twin boundaries are important hydrogen segregation sites in FCC steels. They should not simply be described as weak traps, because reported energies for twin-boundary-associated hydrogen trapping can be relatively high compared with dislocations and random grain boundaries. Their effect on ductility depends on whether hydrogen segregation assists stable twinning and work-hardening or promotes twin boundary decohesion and crack propagation [9,55–57].
- *Vacancies and Vacancy Clusters*: Isolated monovacancies in FCC steels should be considered moderate traps, with first-principles calculations indicating that one monovacancy can accommodate up to six hydrogen atoms and that the incremental E_B is approximately 0.23–0.29 eV per hydrogen atom. Vacancy clusters and void-like defects should be treated separately, because they represent deeper hydrogen traps and are more directly connected to nanovoid formation, local damage accumulation, and crack nucleation [47,60–62].
- *Precipitates and Carbides*: Precipitates and carbides influence hydrogen behavior through their interfaces, coherency strain fields, misfit dislocations and structural vacancies. Their effectiveness as hydrogen traps depends strongly on chemistry, size, coherency, and spatial distribution. For Fe–Mn–Al–C steels, direct quantitative hydrogen-binding data for κ-carbides remain limited; therefore,

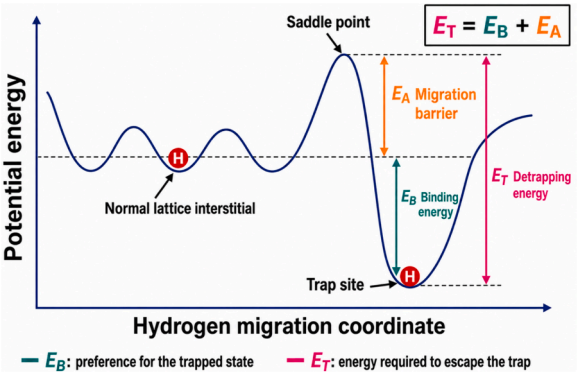


Fig. 3. Schematic distinction between hydrogen binding energy (E_B) and detrapping energy (E_T). E_B is the energy difference between hydrogen at a normal lattice interstitial site and at a trap site. E_A is the migration barrier above the lattice reference state, whereas E_T is the total energy required for hydrogen to escape the trap.

κ-carbides should not be assigned a universal high E_B without caution. Fine coherent κ-carbides may mainly modify SFE, slip planarity and austenite chemistry, whereas coarse or incoherent κ-carbides, grain-boundary carbides and inclusions such as MnS may promote local hydrogen accumulation and crack initiation. For the B2 precipitates, coherent, low-misfit B2-NiAl-type precipitates appear to have limited hydrogen trapping capability compared with incoherent carbide interfaces or vacancy-rich defects. However, B2-related interfaces, interfacial vacancies or misfit-dislocation structures may contribute to stronger trapping when coherency is lost or when the interface is chemically or structurally decorated. Therefore, the role of B2 in Fe–Mn–Al–C–Ni steels should be discussed in terms of interface structure rather than phase identity alone [1,39,47].

In addition, alloying elements affect hydrogen solubility, segregation and damage tolerance through both chemical and microstructural pathways. Mn stabilizes austenite and can increase the solubility of hydrogen in Fe–Mn–C systems, while also reducing the tendency for α'-martensitic transformation. Mn expands the FCC lattice, thereby increasing the size of interstitial sites where hydrogen atoms can reside. As a result, hydrogen solubility tends to rise with Mn content. In general, solubility values are higher in Fe–Mn–C systems than in Fe–Cr–Ni ASSs. Al generally increases SFE and suppresses ε-martensite formation, but its effect on hydrogen solubility in Fe–Mn–Al–C steels is composition-dependent and should be described cautiously [28]. Density functional theory (DFT) studies show a repulsive Al–H interaction in Fe–Mn–Al alloys ($\leq$ 5.4 wt% Mn; $\leq$ 4 wt% Al), while at the same time a stronger binding of hydrogen to Fe if Al is a second nearest neighbor. This suggests that Al could enhance hydrogen trapping and reduce its diffusivity by altering its diffusion path [64]. Al also promotes κ-carbide precipitation during aging, which can alter hydrogen transport indirectly through changes in austenite chemistry, slip behavior, coherency strain and precipitate/interface density. Ni stabilizes austenite and may increase hydrogen solubility, but it does not necessarily introduce strong trapping sites unless Ni-rich phases, segregation zones or secondary interfaces are formed. In Fe–Cr–Ni ternary alloys, a competitive effect of Cr and Ni on hydrogen solubility has been reported [38,65]. Under electrochemical charging, both elements increase hydrogen solubility, while the effect of Cr is much stronger than that of Ni. Therefore, the final hydrogen content is determined by the relative proportions of Cr and Ni.

Overall, hydrogen effects in FCC steels arise from the competition between hydrogen in solid solution and hydrogen segregated at weak, moderate, and strong microstructural sites. The local balance between these populations determines whether hydrogen enhances plasticity, promotes localized deformation, or triggers embrittlement. Therefore, alloy and microstructure design should aim not only to control total hydrogen uptake, but also to optimize microstructural characteristics where hydrogen can reside during deformation.

2.2. Hydrogen mobility under deformation

The FCC crystal structure of austenitic steels is intrinsically characterized by a significantly lower hydrogen diffusivity compared with BCC steels (the activation energy for hydrogen diffusion is approximately 45–55 kJ/mol in FCC austenite [66] vs. 5–15 kJ/mol in BCC ferrite [67]), which impacts the HE sensitivity in a positive way. Moreover, by and large, the influence of alloy composition on the hydrogen mobility in austenitic stainless steels is not as significant as in BCC metals. The following equation for the temperature dependence of hydrogen diffusivity D (m^2/s) which was found for six different undeformed austenitic stainless steels [68] provides a rough estimation:

$$D = 5.76 \times 10^{-7} \exp\left(\frac{-53620}{RT}\right) \quad (1)$$

where R is the universal gas constant (8.314 J/mol. K) and T is absolute temperature (K).

Upon mechanical deformation, hydrogen transport in austenitic steels becomes a highly dynamic process influenced by various metallurgical variables such as phase stability and defect density. Although classical hydrogen diffusion is driven by macroscopic concentration gradients, mechanical deformation introduces a host of complex effects, including dislocation motion, twin formation, and phase transformation, which collectively alter the kinetics and directionality of hydrogen migration on a microscopic scale.

Upon plastic deformation, hydrogen atoms become increasingly mobile, not only by lattice diffusion but also via interaction with mobile dislocations. Hydrogen is attracted to the strain fields surrounding dislocations, leading to the formation of Cottrell atmospheres that may locally reduce the dislocations' glide resistance according to the framework of the HELP mechanism. Although the true hydrogen effects on the mobility of dislocations are still under debate in terms of the macroscopic hardening (see **Section 4.4**), this phenomenon is believed to arise from the ability of a hydrogen atmosphere to shield the elastic stress fields around dislocations, thereby facilitating their motion [13]. Takai et al. [69] measured hydrogen evolution upon the application of plastic strain to 316 L and 304 type Cr–Ni ASSs and observed that hydrogen desorption increased rapidly when plastic deformation started. The observation was explained by dislocations dragging hydrogen along with their movement towards the surface. Notably, this behavior contrasts with that of C, whose interaction with dislocations typically strengthens the material. This divergence stems from the significantly lower diffusivity of C compared with hydrogen, which limits C's dynamic response during deformation.

When localized deformation is promoted in austenitic steels, hydrogen is attracted to stress concentrations formed, for instance, by deformation bands impinging at twin or grain boundaries or intersecting each other. The degree of localized deformation therefore determines the directionality of hydrogen diffusion [70].

In metastable austenitic steels, strain-induced martensitic transformation (specifically the FCC-austenite → α'-martensite transformation) can dramatically alter hydrogen transport. α'-martensite, with its BCC structure, exhibits much higher diffusivity and lower solubility for hydrogen, effectively acting as a fast pathway and local source of mobile hydrogen. When the parent austenite phase

transforms during deformation, the freshly formed α'-martensite is supersaturated with hydrogen due to its significantly lower solubility. Hydrogen can subsequently diffuse to the austenite/α'-martensite phase boundary resulting in easier crack formation [71]. The distribution and size of the martensitic islands is most important with respect to the overall hydrogen diffusivity within the austenitic steel. For instance, if α'-martensite is present at the crack tip, local hydrogen accumulation is facilitated by the fast diffusion pathways leading to faster crack propagation [72]. Strain-induced martensitic transformation can also result in ε-martensite. Due to its HCP crystal structure, ε-martensite has an advantage over α'-martensite as it is characterized by a low hydrogen diffusivity, which might even be lower than the hydrogen diffusivity of FCC-austenite [53]. Nevertheless, its effect on hydrogen embrittlement cannot be assessed from diffusivity alone, since hydrogen solubility/partitioning and trapping at γ/ε interfaces, stacking faults, and ε-martensite plates may still lead to local hydrogen enrichment.

2.3. Modulation of stacking fault energy by hydrogen

It has long been observed that hydrogen can reduce the SFE in FCC steels, thereby fundamentally altering their deformation mechanisms. This effect is hypothesized to originate from alterations in the local bonding environment and distribution of electron density, which weaken the restoring force opposing partial dislocation separation and thereby promote the formation of stacking faults and twins. Early evidence dates back to the 1960 s, when Holzworth and Louthan [73] noted that H-charged 304 L-type austenitic stainless steels exhibited ε-martensite (HCP) platelets, a sign of low SFE enabling the FCC → HCP phase transformation. This contrasted with the behavior of the same steels in H-free conditions, where ε-martensite might not form as readily. The SFE reduction by hydrogen has important consequences for mechanical properties: it increases slip planarity (reducing cross-slip) [31], promotes deformation twinning and martensitic transformations, and often exacerbates HE [6].

Over the decades, a combination of experimental studies, theoretical models, and atomistic simulations has confirmed that absorbed hydrogen indeed tends to lower the SFE of austenite [74]. Direct measurements and indirect indicators clearly show this hydrogen impact. For example, Pontini and Hermida [75] used X-ray diffraction line-broadening techniques with the aid of TEM to measure SFE in a 304-type ASS with and without hydrogen. Their results demonstrated a measurable reduction in SFE upon hydrogen charging (cathodic charging at room temperature), consistent with the appearance of ε-martensite and α'-martensite in the H-charged sample.

Quantitatively, the magnitude of hydrogen-induced SFE reduction in FCC materials has been reported in the range of roughly 15–50% [31], determined either directly through in-situ and ex-situ TEM observations of stacking faults and their spatial distribution [76–78], or indirectly by X-ray diffraction analyses that estimate fault probability [75,79] with and without hydrogen. The wide range reflects methodological differences: the lower bound typically comes from direct TEM observations of partial dislocation separation or stacking fault node geometry (which give the local SFE at the measurement point), while the upper bound is more often reported from X-ray diffraction SFP measurements (which reflect an averaged microstructural response and are sensitive to texture and grain

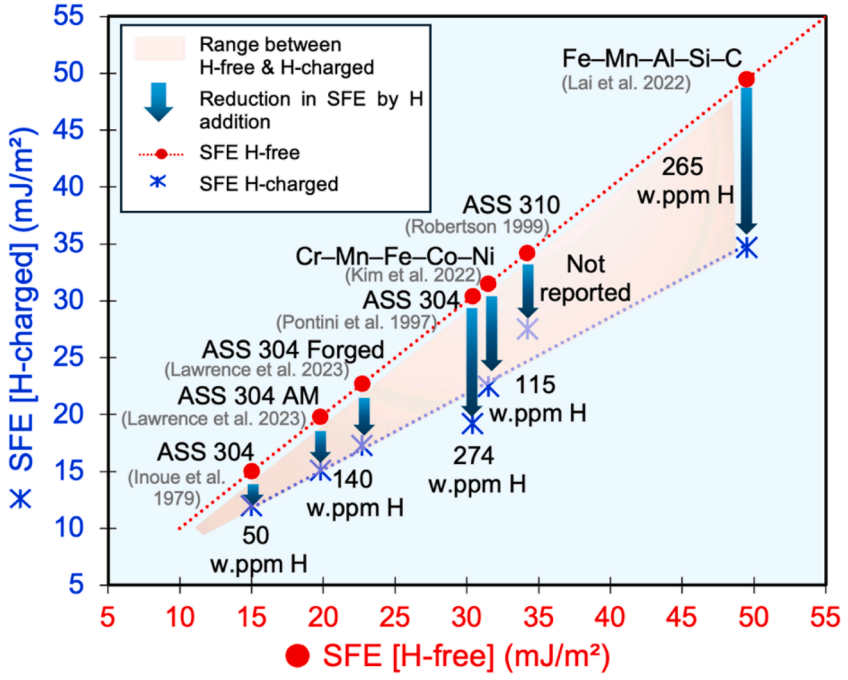


Fig. 4. SFE reduction by hydrogen for different alloys. The x-axis gives the SFE of each H-free alloy, and the y-axis gives the corresponding SFE after hydrogen charging.

statistics).

This range should not be interpreted as a universal hydrogen effect because the underlying measurements are active across different length scales and represent different physical quantities. TEM-based estimates generally reflect local partial-dislocation configurations, whereas diffraction methods provide a more spatially averaged response and remain sensitive to texture, strain, defect density, and the adopted analysis model. Atomistic calculations additionally depend on local hydrogen occupancy, alloy configuration, magnetic state, and the definition of the stable or unstable fault energy. The compiled paired measurements therefore demonstrate that substantial hydrogen-associated changes in fault stability can occur, but they do not establish that hydrogen invariably decreases bulk equilibrium SFE. Hence, Fig. 4 and Table 2 compare the available SFE measurements of different H-charged and H-free FCC alloys. The red symbols in Fig. 4 represent the SFE in the absence of hydrogen, while the blue symbols show the corresponding values in the presence of hydrogen at various concentrations. The downward arrows indicate the magnitude of SFE reduction caused by hydrogen charging. The red dotted line marks the ideal case of no hydrogen effect (H-free SFE), whereas the blue dotted line represents the lower bound trend of hydrogen-induced SFE reduction. The compiled results demonstrate that hydrogen decreases the SFE in the included paired measurements, with the magnitude of reduction depending on both the alloy composition and hydrogen content. Depending on the original SFE (H-free SFE), the exact reduction percentage could be very significant, as it can potentially shift an alloy from above a critical SFE threshold to below it, thereby changing the active deformation mechanism and the resulting effect of hydrogen as an enhancer or detrimental alloying element.

As shown in Fig. 1b, the compiled dataset suggests an approximate empirical crossover near 40 mJ/m^2: alloys below this SFE range exhibit broad scatter and include many cases of pronounced degradation, whereas alloys above this value are more frequently associated with limited ductility loss or hydrogen-assisted enhancement. This crossover should be regarded as a guide to the observed dataset and may serve as a first-order organizing descriptor rather than a strict mechanistic threshold. Deviations are expected when other factors, such as hydrogen distribution, phase stability, grain-boundary character, precipitates, or other microstructural features, dominate the response. For example, the red data points in Fig. 1b correspond to high-SFE Fe–Mn–Al–C alloys containing κ-carbides that nevertheless exhibit significant elongation loss. This behavior is attributed to coarse κ-carbide precipitation, which can promote localized hydrogen accumulation and facilitate crack initiation and propagation. Previously, Gibbs et al. [81] also reported a threshold SFE of 39 mJ/m^2 for Cr–Ni and Cr–Mn stainless steels, below which pronounced hydrogen degradation on tensile ductility was observed for most materials. However, in their screening, there were no alloys with improved properties. It should also be noted that several related but distinct quantities must be separated when discussing hydrogen and stacking faults. Intrinsic or equilibrium SFE is a thermodynamic quantity governed principally by alloy composition, temperature, and the magnetic and thermodynamic state. The generalized SFE landscape describes the complete energy pathway associated with shear and includes both stable and unstable fault energies. Stacking-fault probability is a strain- and microstructure-dependent measure of the fault population and does not provide a direct measurement of equilibrium SFE. In this review, “effective SFE” is used only as a phenomenological description of the local tendency for partial-dislocation separation, stacking-fault persistence, twinning, or phase transformation under a particular combination of hydrogen occupancy, stress, strain, and defect structure. It should not be interpreted as a unique bulk thermodynamic material constant.

The above qualitative experimental evidence of an SFE reduction by hydrogen can be further analyzed by means of theoretical calculations, including DFT and molecular dynamics simulations. Atomistic simulations allow to isolate the effect of hydrogen on fault energies and dislocation behavior. For instance, Li et al. [82] reported that a single hydrogen atom in a perfect γ–Fe lattice significantly increases the stable SFE for a $\{1\,1\,1\} < 1\,1\,2 >$ slip system, while, depending on the interstitial site, H atoms decrease (in the tetrahedral site) or respectively increase (in the octahedral site) the unstable SFE (the energy barrier for creating a fault). The latter finding is also supported by earlier results of He et al. [83]. Thus, H in different sites may have different effects on the ease of stacking fault formation [82]. Both works describe a weakening of the Fe–Fe interactions across the slip plane, but at the same time the Fe–H bonds are

Table 2
Detailed summary of hydrogen-induced SFE reduction values presented in Fig. 4. Additional details on hydrogen content and charging method are provided in Supplementary Table S3.2.

Alloy System	SFE H-free, mJ/m^2	SFE H-charged, mJ/m^2	H Content, w.ppm	SFE Reduction, %	Method	Ref.
ASS 304 Fe–18.2Cr–9Ni–1.2Mn–0.2Mo–0.04C	30.4	19.2	274	36	XRD & TEM	Pontini et al. [75]
Fe–Mn–Al–Si–C Fe–25Mn–5.5Al–3Si–1C	49.5	34.7	265	30	TEM	Lai et al. [28]
ASS 304 L AM* Fe–18.4Cr–9.8Ni–1.5Mn–0.015C	19.8	15.1	140	23	HE X-ray**	Lawrence et al. [80]
ASS 304 Forged Fe–19.6Cr–10.6Ni–1.6Mn–0.028C	22.7	17.3	140	23	HE X-ray**	Lawrence et al. [80]
Cr–Mn–Fe–Co–Ni 20Cr–20Mn–20Fe–20Co–20Ni	31.5	22.5	115	28	TEM	Kim et al. [18]
ASS 304 Fe–18.5Cr–8.5Ni–1.4Mn–0.083C	15	12	50	20	TEM	Inoue et al. [76]
ASS 310 Fe–25.2Cr–19.2Ni–1.6Mn–0.018C	34.2	27.5	***	19	XRD & TEM	Robertson [77]

* Additive manufacturing; ** High Energy Synchrotron X-Ray, *** Not reported, gaseous charging at 40 torr pressure.

speculated to hinder the growth of the stacking fault. These findings partially differ from the results of other FCC metals. For instance, ab initio DFT calculations by Tang and El-Awady [84] examined hydrogen in FCC Ni and found that hydrogen atoms have a negative E_B to stacking faults, meaning that hydrogen is energetically drawn to the fault and stabilizes it. As a result, the presence of hydrogen reduces the stable SFE in the material. Interestingly, the same study noted that hydrogen increases the unstable SFE (the energy barrier for creating a fault) even as it lowers the energy of an already formed fault. In total, the net effect of hydrogen on dislocation slip via formation and growth of stacking faults in pure FCC Fe needs further investigation. However, these effects are rather mild anyhow compared with the E_B of vacancies, and most likely hydrogen-induced vacancies might play a larger role in decreasing the SFE [61,83].

Another level of complexity is added by the alloying elements in austenitic steel. To this end, Jin et al. [85] studied the combined effect of Mn, C, and H on the SFE in austenitic steel and found that Mn decreases the stable SFE, while H and C increase it. This effect was an order of magnitude larger for C than for H. In the ternary Mn–C–H system, the net effect is a significant decrease with increasing Mn content, while the counteracting increase of the SFE with both H and C was much less pronounced.

Movchan et al. [86] found that in a 50Fe–25Cr–25Mn solid solution, hydrogen non-monotonously affects the γ / ε transformation, which is controlled by the SFE. Hydrogen slightly promotes this transformation, thereby lowering the SFE, at low hydrogen contents but suppressing it at higher contents (about 50 at.%). In comparison, hydrogen destabilizes the FCC structure more strongly in Fe–50Cr–25Ni [86], an alloy, which was also investigated by Zhou et al. [74]. These authors developed a Fe–Ni–Cr–H interatomic potential and computed SFE statistics for thousands of local compositions representative of stainless steels, with and without hydrogen. Their statistical, time-averaged molecular dynamic simulations clearly showed a drop in intrinsic SFE distribution due to hydrogen: with internal hydrogen, the average SFE was lower, and the spread of SFE values shifted toward the low end. In practical terms, they concluded that hydrogen reduces SFE and impacts deformation mechanisms. This was confirmed by the authors by running regular MD simulations, which showed increased stacking fault widths under hydrogen influence. Another atomistic study on a high-entropy austenitic Fe–Co–Ni–Cr–Mn alloy showed that hydrogen reduces both unstable and stable SFE in that alloy as well, due to charge transfer effects that weaken metal–metal bonds [87]. This was predicted to promote deformation twinning in an HEA under hydrogen.

These atomistic studies show that the exact impact of hydrogen on the magnitude of the stable and unstable SFE in multi-component alloys significantly depends on the composition and defect–defect interactions including those with vacancies. Nevertheless, for real steels (with multiple impurities and defects), the results from modeling point towards a general tendency of hydrogen to segregate to planar faults and to lower their energy. In an in-situ constant-loading experiment by Shi et al. [88], electron channeling

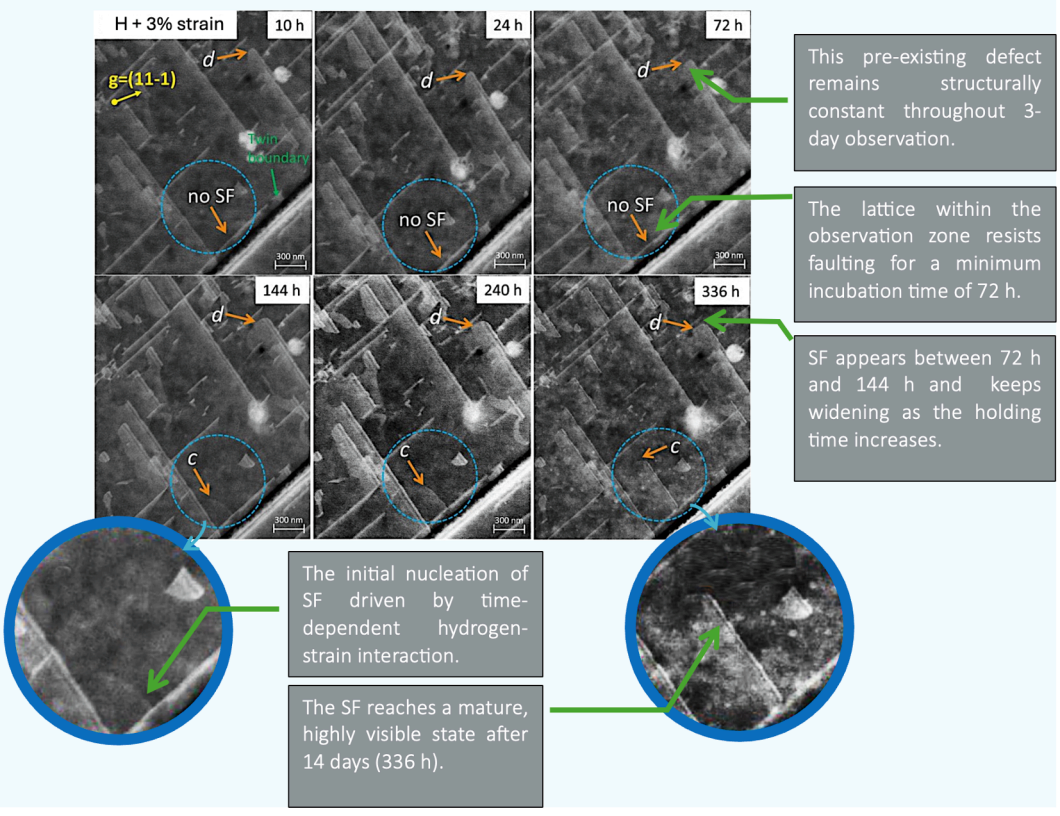


Fig. 5. Time-resolved ECCI observations of defect evolution in a hydrogen pre-charged sample subjected to 3% global strain. Early stages (10–72 h) show dislocation activity without detectable stacking faults, whereas prolonged exposure promotes local fault formation. SF stands for stacking fault. Adapted from Shi et al. [88].

contrast imaging (ECCI) and electron backscatter diffraction (EBSD) were used to directly observe how hydrogen affects the time-dependent evolution of stacking faults in a pre-charged TWIP steel (Fe–18Mn–0.5C) subjected to 3% strain. As shown in Fig. 5, no stacking fault was detected in the selected region during first 72 h. However, between 72 h and 144 h a new stacking fault, marked as c, nucleated from the twin boundary and subsequently widened with increasing exposure time, becoming more evident at 240 h and 336 h. These observations indicate that hydrogen segregation progressively reduces both the SFE and local shear modulus, stabilizing and broadening stacking fault ribbons over time. To exclude extrinsic effects such as stress relaxation or room-temperature creep, a parallel experiment without hydrogen pre-charging was conducted under identical conditions, in which no extension or shrinkage of any stacking fault was detected even after 168 h. This comparison confirms that the time-dependent expansion and nucleation of stacking faults under constant load arises from local evolution of hydrogen concentration near the notch tip regions, rather than mechanical relaxation.

Hydrogen's influence on SFP is another key factor in dictating deformation mechanisms and mechanical behavior in FCC steels. Recent in-situ neutron diffraction and diffraction line profile analysis studies have revealed nuanced but sometimes contradictory effects of hydrogen on SFE and faulting tendencies by quantifying the strain-dependent evolution of SFP, dislocation density and phase stability during deformation in hydrogen pre-charged austenitic steels [21,22,29]. For instance, investigations of Fe–30Mn–2.70Cr–(3Ni)–(1.75Al)–0.25C alloy systems revealed that hydrogen charging at ambient conditions did not produce a significant change in the bulk SFE but increased the SFP during the early stages of deformation [22]. The SFP evolution, as shown in Fig. 6, suggested enhanced dissociation of perfect dislocations into Shockley partials, leading to a higher population of stacking faults, even though the bulk-averaged SFE remained effectively constant. This discrepancy suggests that hydrogen may primarily affect dislocation mobility and stacking fault nucleation kinetics rather than the equilibrium SFE in certain cases. The observed increase in SFP without a corresponding reduction in SFE implies a hydrogen-assisted kinetic facilitation of stacking fault formation, likely due to increased strain localization, enhanced dislocation planarity, and suppressed cross-slip. Furthermore, localized SFE variations may arise near hydrogen-enriched regions, which are not captured by bulk-averaged measurements but are influential at the microscale. In bulk measurements on uniformly hydrogen-charged Fe–24Cr–19Ni ASS, Ito et al. [21] found that hydrogen increased yield and flow stresses mainly through solid-solution strengthening, while its direct effect on SFP, SFE and dislocation storage was minimal. This indicates that hydrogen may promote twinning at a lower strain indirectly, by raising the flow stress needed to reach the twinning stress earlier in the deformation path, rather than by substantially reducing the intrinsic SFE [22,29].

Fig. 6 summarizes these contrasting responses. In the low-SFE high-Mn steel, Fe–30Mn–2.7Cr–0.25C with an estimated SFE of approximately 29 mJ/m^2, hydrogen charging accelerates the early increase in SFP (Fig. 6**a**). The H-charged specimen shows a rapid rise in SFP at low true strains and fractures at a much lower strain than in the non-charged condition. This behavior is consistent with the high tendency of low-SFE austenite to form planar deformation structures, where hydrogen-assisted localization, enhanced dislocation planarity and twin/stacking fault interactions can promote premature fracture. Cho et al. [29] showed that, for this alloy, hydrogen pre-charging led to an apparent increase in both dislocation density and stacking fault density, contributing to macroscopic hardening and embrittlement. Their neutron diffraction analysis also confirmed that the alloy remained essentially austenitic during testing, indicating that the dominant hydrogen effect was associated with defect evolution rather than extensive martensitic transformation.

In contrast, the Al- and Ni-containing high-SFE Fe–30Mn–2.7Cr–1.7Al–3Ni–0.25C alloy with an estimated SFE of approximately 49 mJ/m^2 shows a delayed and more gradual development of SFP (Fig. 6**b**). Although hydrogen still increases SFP compared with the non-charged state, the onset of rapid stacking fault accumulation is shifted to higher strains, and the specimen tolerates much larger deformation before failure. Kong et al. [22] attributed the superior HE resistance of this alloy to its high SFE, increased by Al and Ni alloying, which reduces the propensity for deformation twinning and stacking fault formation under hydrogen pre-charged conditions. In the same study, the high-SFE alloy exhibited a smaller hydrogen-induced loss in notch tensile strength than its low-SFE counterpart. Therefore, the comparison between Fig. 6**a** and Fig. 6**b** supports the idea that the baseline SFE determines whether hydrogen-assisted planar faulting becomes a dominant embrittlement pathway.

The Fe–24Cr–19Ni alloy in Fig. 6**c** presents a different case. Here, both the H-free and H-charged specimens show a nearly monotonic increase in SFP with strain, and the difference between the two conditions remains modest compared with that of the high-Mn alloys. Ito et al. [21] reported that a uniformly H-charged Fe–24Cr–19Ni ASS containing approximately 139 mass ppm hydrogen exhibited increased yield stress, flow stress and uniform elongation, but only minor changes in SFP, SFE, and dislocation density evolution. This result suggests that, in relatively stable Fe–Cr–Ni austenitic steels, hydrogen-induced strengthening can enhance twinning indirectly by increasing the flow stress (i.e., assisting to reach the critical twinning stress), without necessarily producing a strong direct increase in stacking fault density or a measurable reduction in bulk SFE (discussed further in **Section 4.4**). The apparent contradiction between this result and earlier TEM/XRD-based reports may arise from differences in charging method, hydrogen distribution, surface stress, local versus bulk measurement volume and whether SFE is inferred from stress-affected stacking fault widths. Ito et al. [21] specifically argued that localized stresses generated during electrochemical charging may contribute to apparent SFE reductions in surface-sensitive measurements, whereas neutron diffraction provides a bulk-averaged assessment in uniformly H-charged specimens. Taken together, available studies do not support a universal hydrogen-induced reduction in SFE, and it should be regarded as a common but not universal tendency in FCC alloys. Both the sign and magnitude of the reported effect depend on alloy chemistry, magnetic and thermodynamic state, hydrogen concentration and site occupancy, temperature, stress or strain state, and the experimental conditions used. Changes in stacking-fault probability or partial-dislocation separation should therefore not be interpreted automatically as a change in bulk equilibrium SFE.

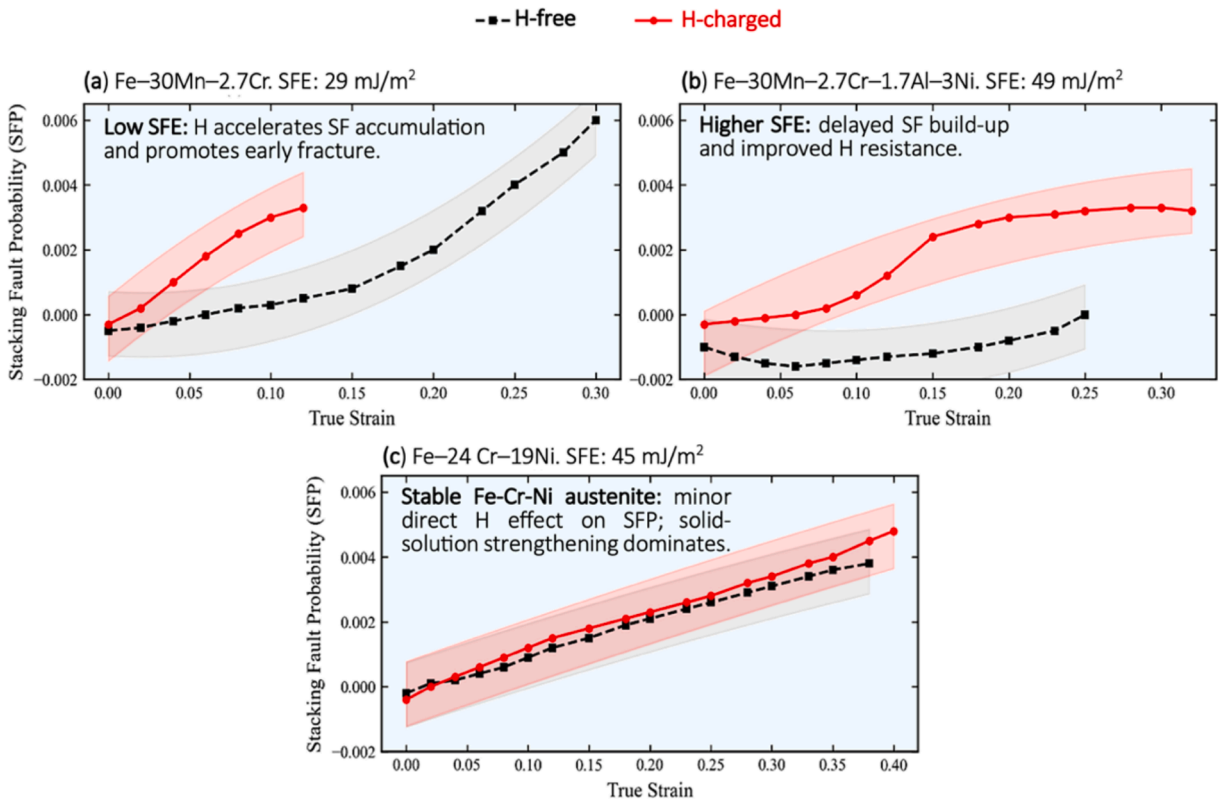


Fig. 6. Stacking fault probability as a functional of true strain for (a) Fe–30Mn–2.7Cr–0.25C [22,29], (b) Fe–30Mn–2.7Cr–1.7Al–3Ni–0.25C [22], and (c) Fe–24Cr–19Ni–0.02C [21]. SF stands for stacking fault.

3. Dual role of hydrogen in slow-strain rate tensile properties

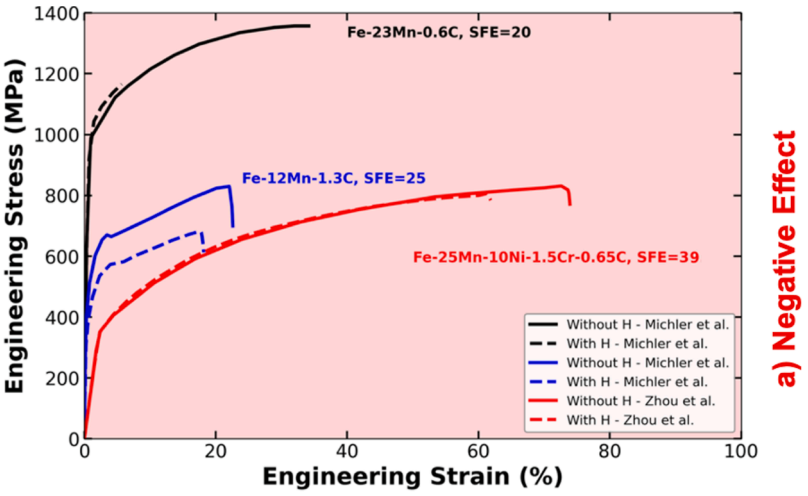
The slow strain rate tensile (SSRT) test is a well-established and one of the most widely used method for evaluating the mechanical response of metallic alloys under hydrogen exposure, either after pre-charging or during in-situ charging. In conventional HE studies, the effect of hydrogen and the extent of embrittlement are commonly assessed by the loss in tensile ductility or fracture strain from reduction in total elongation or cross-sectional area after hydrogen charging. However, it should be noted that elongation loss and reduction of cross-sectional area describe different aspects of hydrogen-affected mechanical response. Elongation loss is more suitable for evaluating the overall tensile response and is useful for assessing the effect of hydrogen on total plastic deformation. However, it can be strongly influenced by gauge length, specimen geometry, strain-hardening capacity, necking behavior, and whether fracture occurs within or outside the hydrogen-affected region. In contrast, reduction of area is more directly related to local fracture resistance and HE susceptibility. It reflects the ability of the material to sustain localized plastic deformation before final fracture and is often more sensitive to hydrogen-assisted cracking. For example, a specimen may still exhibit moderate total elongation while showing a pronounced decrease in reduction of area, indicating a substantial loss of local fracture ductility. Nevertheless, elongation loss is more commonly reported in the literature and is therefore used as the main comparative parameter in this work. Accordingly, the relative elongation loss, also referred to as HE index (HEI), is calculated as:

$$HEI = \frac{El._{H-free} - El._{H-charged}}{El._{H-free}} \times 100 \quad (2)$$

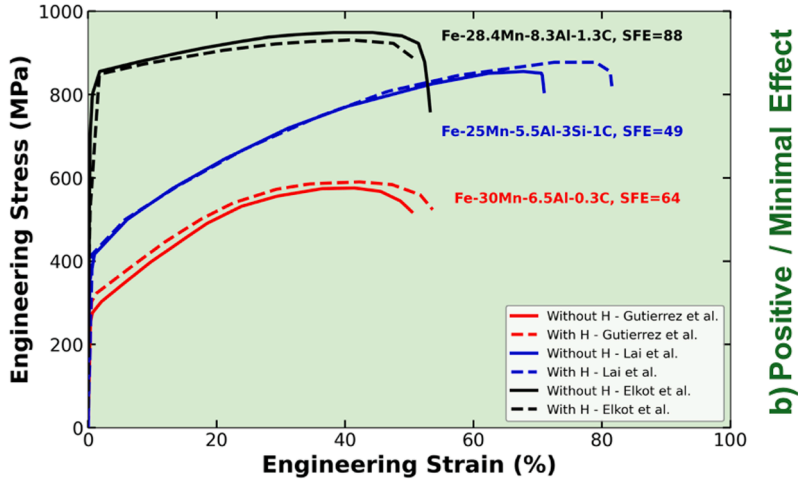
where $El._{H\text{-free}}$ and $El._{H\text{-charged}}$ are the elongation at the fracture in the H-free and H-charged conditions, respectively. A positive HEI indicates ductility loss, whereas a negative value indicates hydrogen enhanced ductility. In this work, HEI is defined based on elongation loss and is equivalent to the relative elongation loss, and they are used interchangeably throughout the manuscript.

As already seen in Fig. 1, most FCC steels exhibit a measurable reduction in tensile ductility after hydrogen exposure, typically reflected by positive HEI. However, it also reveals that several alloys fall within the enhancement zone where hydrogen exposure produces negative HEI.

Fig. 7 highlights this controversial role of hydrogen and exemplifies some representative stress–strain curves selected from studies conducted at comparable slow strain rates, on the order of 10^{-5} s^{-1}. The examples cover different alloy systems and tensile strength levels, categorized here as low yield strength (YS $<$ 400 MPa), medium strength (400 $\leq$ YS $<$ 800 MPa), and high strength (YS $\geq$ 800 MPa).



Strength Level	Alloy	SFE, mJ/m²	UTS, MPa		Total Elongation, %		Change in El% by H
			H Free	With H	H Free	With H	
High	Fe–23Mn–0.6C	20	1370	1170	34	7	↓79%
Medium	Fe–12Mn–1.3C	25	820	650	22	17	↓23%
Low	Fe–25Mn–10Ni–1.5Cr–0.65C	38.79	790	700	74	61	↓18%



Strength Level	Alloy	SFE, mJ/m²	UTS, MPa		Total Elongation, %		Change in El% by H2
			H Free	With H	H Free	With H	
High	Fe–28.4Mn–8.3Al–1.3C	88.4	950	940	54	52	↓3%
Medium	Fe–26.7Mn–5.5Al–3Si–1C	49.5	860	882	71	81.7	↑10.7%
Low	Fe–30Mn–6.5Al–0.3C	64	580	595	51	55	↑4%

Fig. 7. Representative slow-strain-rate tensile responses showing the dual effect of hydrogen on FCC austenitic steels. (a) Classical negative effect of hydrogen, where hydrogen charging reduces elongation in austenitic steels with different strength levels. (b) Positive or minimal hydrogen effect, where selected stable or high-SFE austenitic steels maintain or improve ductility after hydrogen charging. Created based on the results reported by Michler et al. [89], Zhou et al. [90], Gutierrez et al. [24], Lai et al. [28], Elkot et al. [91].

Fig. 7**a** represents the classical negative effect of hydrogen. In these examples, hydrogen exposure decreases elongation and, in some cases, also reduces the apparent strain-hardening capacity before fracture. The high-strength Fe–23Mn–0.6C steel in Fig. 7**a**, with relatively low SFE of about 20 mJ/m^2, shows a pronounced elongation loss after hydrogen exposure. Such low-SFE high-Mn steels are prone to intense planar deformation and twin/grain boundary interactions, all of which can provide favorable sites for hydrogen-assisted crack initiation [89,92]. The medium-strength Fe–12Mn–1.3C steel [89] and the lower-strength Fe–25Mn–10Ni–1.5Cr–0.65C alloy similarly show reduced elongation under hydrogen, despite their different strength levels [90]. These comparisons emphasize that hydrogen degradation in FCC steels is not restricted to a single strength class and cannot be interpreted from tensile strength alone. Rather, it is closely linked to the combined effect of SFE, slip character, twinning tendency, hydrogen distribution, and fracture-path sensitivity.

In contrast, Fig. 7**b** demonstrates that, in selected FCC alloys, hydrogen can either improve ductility or have only a negligible effect, again irrespective of the alloy strength level. These alloys share relatively high SFE values compared with those presented in Fig. 7**a**. Although high SFE does not necessarily guarantee hydrogen compatibility, it can suppress highly damaging planar deformation and martensitic transformation, thereby may shift the alloy response away from embrittlement. The Fe–25Mn–5.5Al–3Si–1C lightweight TWIP steel, which exhibits approximately 10% ductility enhancement (in Fig. 7**b**), provides a great example of this beneficial response. Lai et al. [28] reported hydrogen-induced ductilization in this alloy, with an SFE of approximately 49.5 mJ/m^2, is associated with hydrogen-enhanced twinning in the hydrogen-rich surface layer which can assist deformation without immediately triggering premature cracking. Similarly, Gutierrez-Urrutia et al. [24] reported improved HE resistance in an austenitic Fe–30Mn–6.5Al–0.3C low-density steel with an SFE of 64 mJ/m^2. Hydrogen produced a moderate increase in the YS and an approximately 4% increase in the elongation to fracture. This beneficial response was attributed to the hydrogen-enhanced deformation banding and microbanding, suggesting that hydrogen-induced strain localization is not necessarily detrimental if it contributes to stable strain partitioning rather than crack initiation.

The comparison between Fig. 7**a** and Fig. 7**b** can also be directly linked to the broader trend in Fig. 1, where some FCC steels show severe relative elongation loss up to approximately 90%, whereas others fall into the minimal-loss or ductility-enhancement region. Fig. 1**b** further demonstrates that this trend is not necessarily composition-dependent. Another clear example of the positive and negative effects of hydrogen is presented in Fig. 8, obtained from a systematic work by Yamada et al. [27], who investigated the Fe–30Mn–(6 – X)Si–XAl austenitic alloy family with varying SFEs ranging from 16 to 64 mJ/m^2. In the low-SFE Fe–30Mn–6Si and Fe–30Mn–4Si–2Al alloys, where ε-martensitic transformation was active, hydrogen caused premature fracture and reduced elongation. In the Fe–30Mn–3Si–3Al alloy, with an SFE of approximately 41 mJ/m^2, hydrogen had a minimal effect or slight improvement, suggesting that the alloy was already within an optimized TWIP regime. Instead, the high-SFE Fe–30Mn–6Al alloy, with an SFE of approximately 64 mJ/m^2, showed distinctly improved uniform and total elongations after hydrogen gaseous pre-charging. This study provides further evidence of composition- and SFE-dependent variations in hydrogen uptake and mechanical response within the same alloy family under identical applied conditions.

Additional examples of hydrogen-induced degradation and hydrogen-assisted enhancement in FCC steels are summarized in Table 3. These examples clearly indicate that the boundary between degradation and enhancement cannot be defined by a single parameter. While an SFE threshold range near 40 mJ/m^2 is useful as a first-order screening criterion, several exceptions exist. Some alloys with SFE above this threshold still show ductility loss when grain boundary carbides, κ-carbides, strong localization, or unfavorable charging conditions create crack-sensitive hydrogen distributions. In addition, the compiled data in Table 3 also suggest that

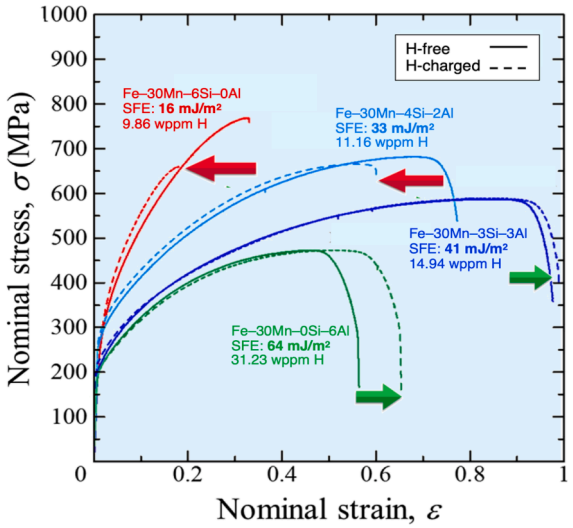


Fig. 8. Positive and negative effects of hydrogen on tensile behavior in polycrystalline Fe–30Mn–(6-X)Si–XAl austenitic alloys, pre-charged with hydrogen gas at 10 MPa.
Reproduced from Yamada et al. [27].

Table 3
Further representative literature examples on the dual role of hydrogen on tensile properties of FCC steels ranging from a strong enhancement to severe degradations. Unless otherwise specified, hydrogen charging was performed electrochemically in all cases. Additional details on hydrogen content and sample dimension are provided in Supplementary Table S3.3.

Alloy System	SFE, mJ/m^2	H Content, w.ppm	Strain Rate, s^{-1}	Elongation Changes under H	Response	Main interpretation	Ref.
Fe–25Mn–5.6Al–3Si–1C	49.5	~4.5	10^{-5}	71 → 82%	Strong enhancement	Lower strain rate strengthens the beneficial H effect.	[28]
Fe–24Cr–1Mn–19Ni–0.02C	40	~140 Gaseous H	10^{-5}	55 → 65%	Enhancement	Greater improvement at a lower strain rate, suggesting kinetic coupling between H and deformation.	[19]
Fe–24Cr–19Ni–0.02C	48	8–133 Gaseous H	5×10^{-3}, 10^{-5} & 10^{-7}	57.7 → 58.7%; up to 64% at higher H	Enhancement	H acts as an interstitial strengthening element; improvement increases with H content.	[25]
Fe–24Cr–19Ni–0.02C	40	139 Gaseous H	3×10^{-5}	42 → 47%	Enhancement	In-situ neutron diffraction shows solid-solution strengthening dominates over direct SFE reduction.	[21]
Fe–30Mn–6.5Al–0.3C	64	~101 Gaseous H	5×10^{-5}	51 → 55%	Enhancement	Hydrogen-enhanced microbanding can improve ductility when localization remains stable.	[24]
Fe–25Mn–5.6Al–3Si–1C	49.5	~4.5	10^{-3}	72 → 79%	Enhancement	Hydrogen-induced ductilization through enhanced twinning/plasticity.	[28]
Fe–24Cr–1Mn–19Ni–0.02C	40	~140 Gaseous H	10^{-4}	62 → 70%	Enhancement	Solute H improved strength–ductility.	[19]
Fe–30Mn–2.7Cr–1.7Al–3Ni–0.25C	49	Gaseous H	5×10^{-4}	22 → 32%	Enhancement	Higher SFE delays stacking-fault accumulation and improves resistance relative to low-SFE counterpart.	[22]
Fe–30Mn–6Al	64	~31.2	6×10^{-5}	45 → 51%	Enhancement	High SFE suppresses damaging transformation and supports stable plasticity.	[27]
Fe–19Mn–2Al–0.6C	30	~0.65	4.8×10^{-5}	70 → 75%	Slight enhancement	Al raises SFE and reduces damaging H-assisted planar localization.	[92]
Fe–30Mn–3Al–3Si	41	~14.9	6×10^{-5}	83 → 84%	Neutral / slight enhancement	Near or above the critical SFE range, H has little ductility penalty.	[27]
Fe–31Mn–3Al–3Si–0.008C	40	7.1	8×10^{-6}	55 ↔ 55%	Neutral	Stable austenite and fine grains can reduce H ductility loss under selected conditions.	[8]
Fe–19Mn–1Al–0.6C	24	~2.2	4.8×10^{-5}	68 ↔ 68%	Neutral	Small Al addition reduces H sensitivity compared with lower-SFE Al-free alloy.	[92]
Fe–25Mn–10Ni–1.5Cr–0.65C	38.8	13.4	5×10^{-5}	74 → 62%	Moderate degradation	Near-threshold SFE still allows H-assisted planar deformation and ductility loss.	[90]
Fe–16Mn–10Ni–1.5Cr–0.65C	29.5	~17.2	5×10^{-5}	58 → 44%	Degradation	Lower SFE increases sensitivity to H-assisted planar slip/twinning.	[90]
Fe–30Mn–2.7Cr–0.24C	29	–	5×10^{-4}	32 → 12%	Severe degradation	H accelerates stacking-fault accumulation and premature fracture.	[22]
Fe–24Mn–3Cr–0.35C	35	21–25	6×10^{-5}	62 → 47%; 59 → 42%	Degradation	H promotes TRIP/TWIP-assisted localization and early fracture.	[93]
Fe–24Mn–3Cr–0.35C	35	25–36	6×10^{-5}	65 → 45%; 45 → 15%	Severe degradation	Higher H content intensifies ductility loss in metastable austenite.	[94]
Fe–18Mn–0.6C	16	~0.36	5×10^{-5}	62 → 32%	Severe degradation	Very low SFE promotes H-assisted cracking even at low absorbed H.	[95]
Fe–18Mn–1.15C	35	~5.2 In-situ charging	1.7×10^{-6}	80 → 19%	Severe degradation	Slow strain rate allows stronger H-defect interaction and severe embrittlement.	[96]

(*continued on next page*)

Table 3 (*continued*)

Alloy System	SFE, mJ/m^2	H Content, w.ppm	Strain Rate, s^{-1}	Elongation Changes under H	Response	Main interpretation	Ref.
Fe–17Mn–0.8C	21	–	10^{-5}	110 → 50%	Severe degradation	Low SFE and slow strain rate strongly enhance H-assisted ductility loss.	[9]
Fe–22Mn–0.6C	28	9–22	4×10^{-5}	77 → 63%; down to 30% at higher H	H-content-dependent degradation	Increasing H content progressively reduces elongation.	[97]
Fe–27Mn–0.3C	27	–	10^{-3}	75 → 10%	Severe degradation	H-assisted cracking along planar defects/twin-related interfaces.	[98]
Fe–28.8Mn–6Si–7Cr	10	~27	10^{-2} –10^{-4}	48 → 25%; 45 → 20%	Degradation	Very low SFE and transformation-prone deformation led to H sensitivity.	[99]
Fe–18Mn–0.56C	20	0.63–1.17	10^{-5} –10^{-6}	80 → 30%; 80 → 10%	Severe degradation	Slower strain rates and H promote strong ductility loss.	[100]
Fe–17.5Cr–11.5Ni–2.2Mo–0.008C	36	2.7–4	5×10^{-5}	70 → 60%; down to 3% in severe condition	Variable degradation	Hydrogen effect depends strongly on local stability and test conditions.	[101]
Fe–17Cr–13Ni–2.5Mo–0.02C–0.04 N	29.8	~2.48	5×10^{-5}	62 → 44%	Degradation	Lower SFE stainless steel remains sensitive to H-assisted ductility loss.	[102]
Fe–15Cr–11Mn–6Ni–0.02C –0.3 N	40.1	~0.73	5×10^{-5}	48 → 44%	Mild degradation	SFE near threshold gives moderate H resistance but not complete immunity.	[102]
Fe–28Mn–8Al–1.3C	88.4	~15	7×10^{-5}	73 → 67%; 47 → 10% depending on condition	Variable / severe in some states	High SFE alone is insufficient; grain boundary κ-carbides or brittle interfaces can dominate.	[91]
Fe–30Mn–8Al–1.27C	84	9–17	10^{-6}	77 → 63%; 22 → 4% in susceptible state	Variable / severe degradation	Microstructure controls whether high-SFE resists or suffers H damage.	[103]
Fe–25Mn–10Al–1.16C	110	~0.16	10^{-4}	44 → 5%	Severe degradation despite high SFE	High SFE does not guarantee resistance when brittle interfaces/precipitates dominate.	[104]

Colored arrows indicate the overall elongation change after H-charging: → improved, → worsened, ↔ negligible.

strain rate alone does not determine whether hydrogen causes enhanced plasticity or embrittlement. HEP is observed over a relatively broad strain-rate range, from around 10^{-3} to 10^{-7} s^{-1}, indicating that the beneficial effect is not restricted to a specific deformation rate. The same trend can also be seen in Fig. 1**e**. Strain rate may still influence the kinetics of hydrogen–defect interactions, particularly under very slow testing, but the available evidence does not support considering it as the principal controlling parameter. Thus, HEP should be viewed as a mechanism- and microstructure-dependent response that can occur across different strain rates when the alloy falls within a favorable effective SFE and stability window.

Hydrogen content should also be considered as another key factor, because the hydrogen-assisted property enhancement does not occur unconditionally simply due to the presence of hydrogen; rather, it naturally depends on the hydrogen concentration. Fig. 9, based on the work of Ogawa et al. [25], presents the stress–strain response and product of tensile strength and uniform elongation at different displacement rates and hydrogen contents in an Fe–24Cr–19Ni ASS. It shows that the magnitude of strength-ductility improvement varies with both displacement rate and hydrogen concentration. At the lowest displacement rate, the H-charged sample shows a significant improvement in strength–ductility balance. At the intermediate rate, the improvement is even more pronounced, especially at higher hydrogen content, whereas at the highest displacement rate the benefit is reduced. This trend implies that hydrogen must be sufficiently mobile on a local scale and sufficiently concentrated to interact with the evolving deformation structure during tensile straining. When hydrogen content is too low, its effect on flow stress, twinning, or local defect interactions may remain limited. When the imposed deformation rate is too high, hydrogen redistribution may not occur as fast as the dislocation motion and evolving defects.

An additional experimental factor that should be considered when interpreting SSRT data is the specimen geometry, particularly for electrochemically charged FCC alloys. Due to the low hydrogen diffusivity in FCC lattices, electrochemical charging generates a

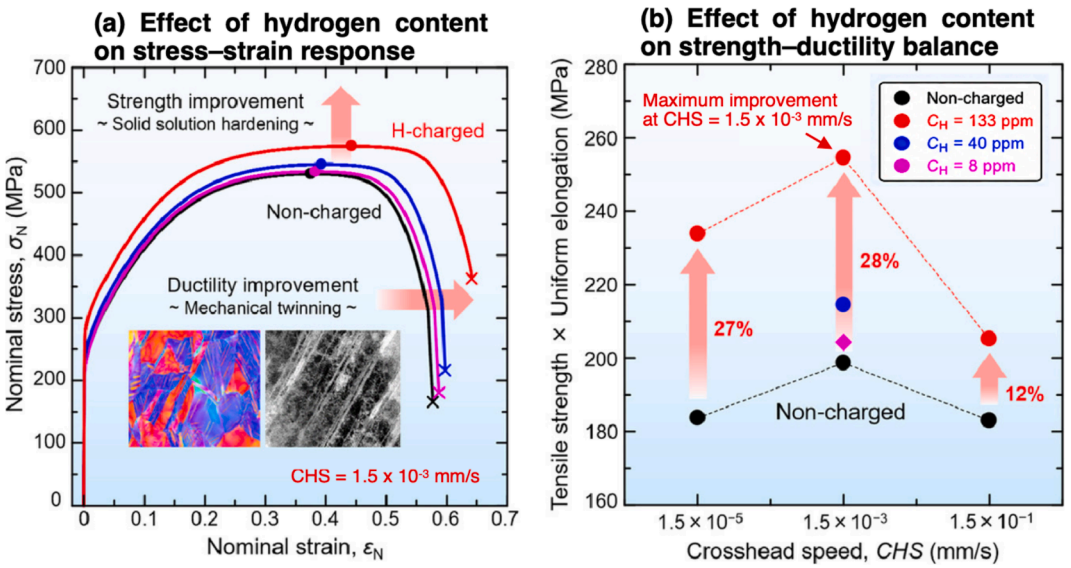


Fig. 9. Effect of hydrogen content and displacement rate on the strength–ductility balance of a stable Fe–Cr–Ni austenitic stainless steel, expressed as the product of tensile strength and uniform elongation. Crosshead speeds (CHSs) of 1.5×10^{-1}, 1.5×10^{-3} and 1.5×10^{-5} mm/s correspond to the initial strain rates of 5.0×10^{-3}, 5.0×10^{-5} and 5.0×10^{-7} s^{-1}, respectively. Modified and reproduced from Ogawa et al. [25].

strongly non-uniform hydrogen distribution, with hydrogen concentrated predominantly near the specimen surface. Consequently, in conventional tensile specimens, the relatively H-free bulk may dominate the global mechanical response, leading to an underestimation or even masking of the intrinsic hydrogen effect. Lee et al. [106] recently demonstrated this issue using additively manufactured Co–Cr–Ni medium-entropy FCC alloy specimens.

As illustrated in Fig. 10, while a conventional geometry showed only a modest change in tensile response after hydrogen charging, a newly designed U-grooved tensile specimen with a thin ligament revealed a more severe hydrogen-induced degradation, including a pronounced reduction in both UTS and elongation. This result emphasizes that, in FCC alloys, the apparent balance between hydrogen-assisted enhancement and degradation can also be affected by hydrogen penetration depth and specimen dimensions. Therefore,

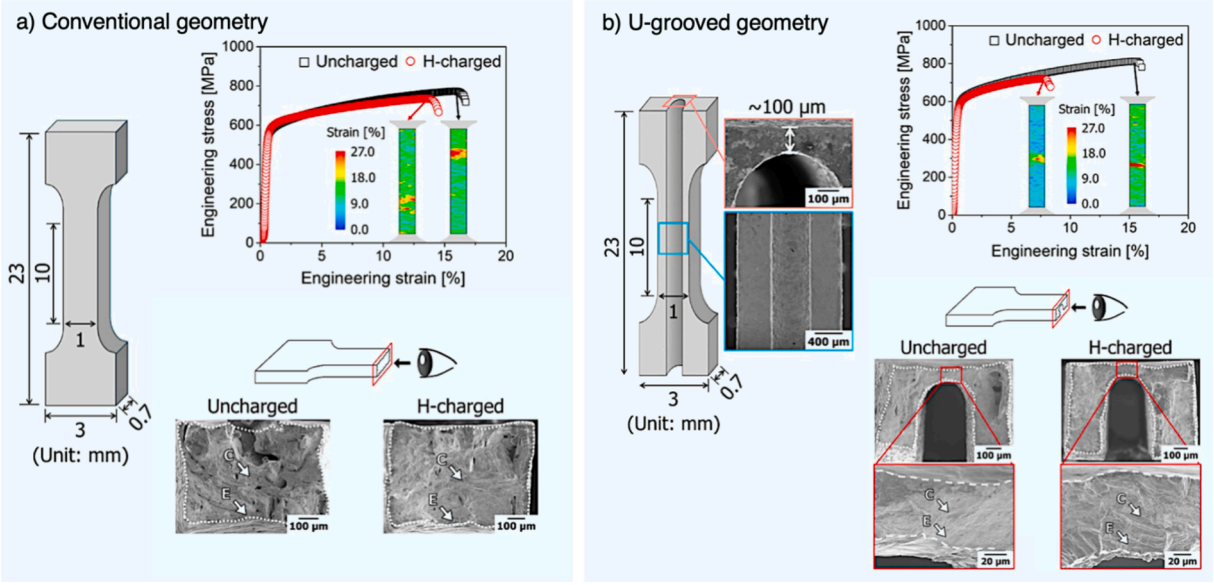


Fig. 10. Influence of tensile-specimen geometry on the apparent hydrogen effect in electrochemically charged FCC alloys. (a) Conventional tensile-specimen geometry and (b) U-grooved tensile-specimen geometry with an approximately 100 μm ligament, designed to increase the fraction of the load-bearing volume influenced by hydrogen while preserving nominally uniaxial loading, along with corresponding engineering stress–strain curves, digital image correlation strain maps, and fracture-surface morphologies of H-free and H-charged specimens. C and E indicate the center and edge regions, respectively. Modified and reproduced from Lee et al. [106].

comparisons across literature data should account not only for hydrogen content, strain rate, and SFE, but also for the spatial distribution of hydrogen within the tested volume, particularly hydrogen distribution through the specimen thickness. Nevertheless, systematic studies that purposefully deconvolute hydrogen content and its distribution in FCC alloys remain limited. Most available works compare only a H-free condition with a single H-charged state, which makes it difficult to define an optimum hydrogen concentration window for mechanical enhancement. Accordingly, hydrogen content should be regarded as a critical design variable (alongside others), as the available evidence [23,25], together with Fig. 2, indicates that the beneficial effect of hydrogen follows an optimum-window behavior; insufficient hydrogen may be unable to activate strengthening or plasticity-enhancing mechanisms, whereas excessive hydrogen can shift the response toward localized damage and embrittlement.

Overall, the underlying mechanisms for hydrogen-enhanced ductility are still under active investigation. Most hypotheses involve hydrogen-induced modification of the deformation mechanisms, which in turn promotes deformation twinning and deformation microbanding. These mechanisms can enhance work-hardening capacity, delay the onset of necking, and thereby sustain or even improve ductility in the presence of hydrogen. Notably, many alloys exhibiting hydrogen-enhanced ductility are austenitic steels alloyed with Al and/or Ni, in which these alloying elements generally increase the SFE and strongly suppress martensitic transformation, thereby reducing the likelihood of severe hydrogen-induced degradation. Thus, the dual role of hydrogen should be described as a competition between hydrogen-assisted work-hardening and H-assisted damage localization. The former dominates when solute hydrogen enhances flow stress, twinning, or microbanding in a stable and damage-tolerant microstructure. The latter dominates when the same localization processes interact with weak interfaces, low-SFE planar defects, martensitic transformation, grain boundary carbides, or high local hydrogen segregations. A detailed overview of the enhancement mechanisms is discussed in **Section 4**, while **Section 5** and **Section 6** subsequently explain how microstructural sensitivity and charging conditions will affect the material response under loading and hydrogen exposure.

4. Mechanisms of hydrogen-enhanced mechanical properties in austenitic steels

The classical HELP mechanism is widely recognized as one of the fundamental embrittlement mechanisms in austenitic steels. This mechanism, which was originally proposed by Birnbaum and Sofronis [13] remains central to explaining hydrogen-assisted deformation and fracture in metallic materials. According to this concept, hydrogen promotes localized dislocation activity, reduces barriers for dislocation motion, and can intensify strain localization. In many alloys, such localization accelerates crack initiation and propagation, thereby contributing to HE and premature fracture. However, as discussed, recent observations in stable FCC austenitic alloys show that hydrogen-assisted plasticity does not always lead to premature failure. Under certain conditions, hydrogen can contribute to enhanced work-hardening, delayed plastic instability, and improved strength–ductility balance.

Building on current understanding of hydrogen–microstructure interactions, in this review, the term HEP (hydrogen-enhanced plasticity), as briefly introduced in Fig. 2, is used as an umbrella concept to describe cases in which hydrogen-assisted defect activity produces a beneficial macroscopic mechanical response. HEP should not be viewed as a mechanism that contradicts HELP. Rather, HELP-type hydrogen–dislocation interactions may still operate locally, but their macroscopic consequence depends on how the surrounding microstructure accommodates the resulting plasticity. When hydrogen-assisted localization is stabilized by work-hardening, deformation twinning, microbanding, or distributed strain partitioning, the overall response may be beneficial. When the same localization intersects with weak interfaces, martensite/austenite boundaries, grain boundaries, coarse precipitates, or other crack-sensitive paths, it promotes damage. Therefore, HEP is best understood as a favorable macroscopic outcome of hydrogen–defect interactions, not as a replacement for classical HE mechanisms.

This section explores the fundamental sub-mechanisms of HEP proposed in various studies, including hydrogen-enhanced twinning (**Section 4.1.1**), hydrogen-enhanced densified twinning (**Section 4.1.2**), hydrogen-enhanced deformation banding (**Section 4.2**), hydrogen-enhanced microbanding (**Section 4.3**), and hydrogen-enhanced hardening or solid-solution strengthening (**Section 4.4**). These mechanisms are not mutually exclusive. Their relative contribution depends on alloy composition, local hydrogen concentration, SFE, phase stability, strain rate, defect density, and the spatial distribution of hydrogen. **Section 4.5** will present a preliminary unified mechanism map of the interplay between these mechanisms where they can operate concurrently or sequentially within the same alloy.

4.1. Hydrogen-enhanced twinning (HET) and densified twinning (HEDT)

Hydrogen-enhanced twinning (HET) refers to the increased tendency for mechanical twinning in the presence of hydrogen. This may appear as an earlier onset of twinning, a higher twin volume fraction at a given strain, or a greater contribution of twinning to work-hardening. HET is most relevant in FCC alloys with intermediate effective SFE (around 40–45 mJ/m^2), where twinning is possible from a crystallographic point of view, but requires sufficient local stress, partial-dislocation activity, and twin embryo stability.

The physical basis of HET is closely linked to the effect of hydrogen on stacking-fault stability and partial dislocation behavior. By reducing the local effective SFE, hydrogen can stabilize intrinsic stacking faults and promote the dissociation of perfect dislocations into Shockley partials. Since stacking faults are precursors to deformation twins, this effect lowers the barrier for twin-embryo formation. As a result, the critical twinning stress, the threshold shear stress required to initiate twin formation, is reduced in the presence of hydrogen. This reduction in critical twinning stress occurs through several mechanisms [30]:

i) SFE-dependent reduction: The decreased SFE lowers the energy barrier for dislocation dissociation, thereby reducing the external stress required to initiate twinning.

ii) Dislocation shielding effect: Hydrogen reduces the interaction energy between dislocations and obstacles such as twin boundaries or forest dislocations. This facilitates the dislocation motion and reduces the stress needed for dislocation pile-up to trigger twinning. This is because a dislocation pile-up amplifies the local stress at its leading dislocation; when this local stress reaches the critical twinning stress, a deformation twin can nucleate. Hydrogen allows this condition to be reached at lower external applied stress.

iii) Dislocation density modulation: Hydrogen promotes dislocation multiplication and increases local dislocation density. While this can raise local back-stresses (due to pile-up and dislocation–dislocation interactions), hydrogen simultaneously reduces the barriers to dislocation motion, leading to a net decrease in critical twinning stress.

Hydrogen-enhanced densified twinning (HEDT), on the other hand, should be considered a specific microstructural expression of HET rather than a separate mechanism. In HET, hydrogen increases the probability or extent of twinning. In HEDT, hydrogen additionally modifies the twin morphology by producing thinner, more closely spaced and densely distributed twins within twin bundles. Thus, HET describes the activation or promotion of twinning, whereas HEDT describes the hydrogen-assisted refinement and densification of the twin network.

This distinction helps to separate two effects. First, hydrogen may increase the possibility that deformation twins nucleate at lower strain or stress. Second, once twins are nucleated, hydrogen may modify their morphology by increasing twin-boundary density and refining the twin substructure. The first process corresponds to HET, while the second corresponds to HEDT. Hence, HET and HEDT describe two levels of the same hydrogen-assisted twinning response. HET describes earlier or more frequent activation of twinning, whereas HEDT describes the refinement and multiplication of twin boundaries after twinning has been activated, and it is more intensified at higher SFE and higher hydrogen content.

4.1.1. Hydrogen-Enhanced twinning (HET)

In coarse-grained FCC metals, deformation twinning is commonly idealized as the result of the highly coordinated glide of Shockley partial dislocations (SPDs) with identical Burgers vector on successive {111} close-packed planes [107]. While this description captures the crystallographic outcome of twinning, a more fundamental understanding requires explicit consideration of how deformation twins nucleate from specific arrangements of partial dislocations and how these nuclei subsequently thicken and propagate. Over the past decades, various atomistic and dislocation-based models have been proposed to describe the nucleation and growth mechanisms of deformation twins in FCC metals. The most representatives of them are summarized in the Supplementary Document. These include the Venables pole mechanism [108], deviation mechanisms involving sessile dislocations or obstacles [109], and the three-layer twin nucleus model proposed by Mahajan and Chin [110]. More recent work on Fe–Mn–C, Fe–Mn–Si–Al TWIP steels [111–114] and FCC high-entropy alloys [115,116] has shown that several twinning nucleation routes can operate simultaneously, depending on local orientation, dislocation configuration, and strain state.

From a crystallographic perspective, hydrogen does not appear to introduce a new twinning mechanism, and deformation twins are still formed through classical partial-dislocation-mediated processes [103]. Existing experimental, atomistic, and modeling studies collectively indicate that the role of hydrogen is better described as modifying the kinetics, stability, and stress threshold of these pre-existing twinning pathways rather than creating a fundamentally new path for twin formation [117,118].

HET refers to the increased propensity of mechanical twinning in the presence of hydrogen. This may be reflected by a higher twin volume fraction at a given strain, an earlier onset of twinning, or an enhanced contribution of twinning to work-hardening, as illustrated in Fig. 11.

HET could emerge as the dominant plasticity-enhancing mechanism in alloys with the upper band of intermediate original SFE (around 40–45 mJ/m^2).[1] However, when hydrogen is present, a higher original SFE is needed, because hydrogen can reduce the effective SFE. If SFE is too low, ε-martensite or extensive stacking faulting may dominate; if SFE is too high, glide of perfect dislocations, deformation banding, or microbanding may become more favorable than twinning. The SFE-reduction presented in Fig. 4 is therefore useful, as it illustrates how hydrogen can shift the effective SFE of several FCC alloys toward a lower range. Direct experimental evidence for this effect is provided by weak-beam dark-field TEM observations in a Cr–Mn–Fe–Co–Ni high-entropy alloy. Kim et al. [18] showed that hydrogen absorption increased the separation width between SPDs. This wider partial separation corresponded to a reduction in SFE from approximately 31.5 ± 3.5 mJ/m^2 in the H-free condition to 22.5 ± 2.5 mJ/m^2 after hydrogen charging at an estimated hydrogen concentration of about 115 w.ppm. This result is important because it directly connects hydrogen to partial-dislocation separation, which is one of the key prerequisites for stacking fault persistence and twin embryo formation.

A similar observation is reported in the light-weight Fe–Mn–Al–Si–C TWIP steel studied by Lai et al. [28]. In that alloy, the original SFE was relatively high, around 49.5 mJ/m^2, which is beyond the upper boundary of the TWIP regime. However, after hydrogen charging, the hydrogen concentration was higher near the surface. This surface layer containing approximately 265 w.ppm of hydrogen exhibited an earlier onset of deformation twinning, at about 10% strain, compared with the center region, where twinning started at about 20% strain. The measured SFE was also reduced from 48.1 mJ/m^2 in the center to 34.7 mJ/m^2 in the H-rich surface layer. This provides a clear example of how hydrogen can locally move an alloy from a high-SFE state toward a more favorable twinning regime.

From a dislocation-mechanism perspective, hydrogen may facilitate twinning by stabilizing dissociated SPDs and suppressing cross-slip. Since cross-slip requires constriction of partials back into a perfect dislocation, hydrogen-induced stabilization of the separated partial configuration makes this process more difficult and less energetically favorable. As a result, dislocation motion

[1] *Original SFE refers to the SFE of a system before the presence of hydrogen in the alloy composition. In the absence of hydrogen, the SFE range of 20–40 mJ/m^2 is favorable for mechanical twinning.*

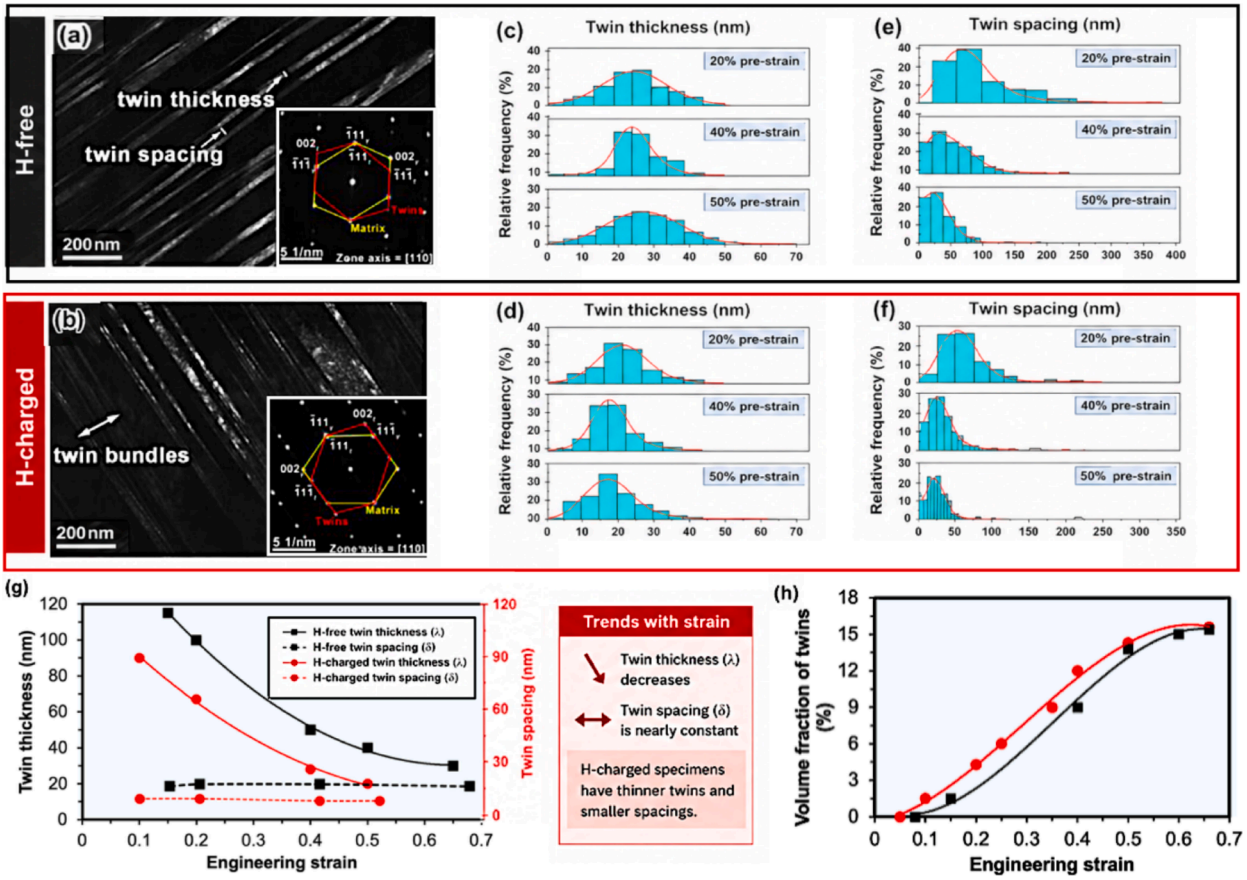


Fig. 11. TEM dark-field images of the (a) H-free and (b) H-charged specimens strained to 50%, showing the formation of mechanical twins. Statistical distributions of individual twin thickness (c, d) and twin spacing (e, f) are presented for the H-free and H-charged specimens, respectively, at different strain levels of 20%, 40%, and 50%. (g) Evolution of the average twin thickness and twin spacing as a function of strain, and (h) corresponding variation in twin volume fraction with strain. Modified and reproduced from Zhang et al. [30].

becomes more planar, allowing stacking faults to persist over longer distances [117,118]. This increases the probability that stacking faults overlap on adjacent {111} planes, facilitating the formation of twin embryos. In parallel, hydrogen-enhanced planar slip promotes the formation of dislocation pile-ups at grain boundaries, twin boundaries, and other obstacles. The local stress concentration at the head of such pile-ups can help reach the critical twinning stress at a lower macroscopic strain.

Atomistic simulations and elasticity-based models demonstrate that hydrogen segregates to dislocation cores and stacking faults, where it screens elastic interactions between partial dislocations [117,119,120]. This screening effect increases the equilibrium separation between Shockley partials, thereby stabilizing dissociated configurations and reducing the possibility of recombination into perfect dislocations. Although this effect does not necessarily translate into a measurable reduction in bulk SFE, it locally favors the persistence of stacking faults and promotes planar slip, which are both prerequisites for twin embryo formation [29]. Therefore, the term "effective SFE" is more appropriate here, because the relevant energy barrier is not only a bulk thermodynamic quantity, but also reflects local hydrogen distribution, partial dislocation separation, stacking fault stability, local stress state, and defect interactions. This distinction is important because some bulk diffraction studies have also reported little or no measurable change in SFE after hydrogen charging, even when local microstructural observations show enhanced twinning or higher twin-boundary density.

As presented in Fig. 11, in high-Mn TWIP steels hydrogen can influence the stability and critical size of twin embryos. H-charged specimens consistently exhibit higher twin densities, reduced twin thicknesses, and decreased twin spacing, features collectively described as HEDT [28,93,117], which will be described in **Section 4.1.2**. These findings imply that hydrogen reduces the critical twin embryo thickness required for stability, either by lowering the local energy barrier for embryo formation or by increasing the local driving stress through enhanced dislocation accumulation. However, this balance is delicate. Twin boundaries can also trap hydrogen and become crack-sensitive interfaces in low-SFE or highly stressed TWIP steels. Therefore, HET and HEDT can be either beneficial or harmful depending on whether twinning contributes to stable strain partitioning or localized fracture.

Despite the above discussed scientific progress, it is also important to emphasize that a fully unified and quantitative description of hydrogen-assisted twin nucleation remains absent. Direct experimental evidence capturing the earliest stages of twin embryo formation in the presence of hydrogen, particularly at the atomic scale, is still lacking. Current understanding instead points toward a

scenario in which hydrogen primarily affects dislocation mobility, local stress states, and defect stability, rather than fundamentally altering the classical twinning mechanisms themselves. Consequently, HET should be viewed as a kinetic and microstructure-mediated phenomenon, emerging from the interplay between hydrogen–dislocation interactions, cross-slip suppression, and localized stress amplification, rather than from a simple reduction in SFE.

4.1.2. *Hydrogen-enhanced densified twinning (HEDT)*

Hydrogen-enhanced densified twinning (HEDT) represents a more specific microstructural appearance of HET. In HEDT, hydrogen does not merely increase the occurrence of twinning; but it refines the twin structure. The characteristic features are reduced individual twin thickness, decreased twin spacing, increased twin-boundary density, and higher twin volume fraction at a given strain. These features create a finer internal barrier network and enhance dynamic Hall–Petch strengthening. It has typically been reported in high SFE ($> 45\ mJ/m^2$) materials in the presence of high hydrogen content [25,30].

Fig. 11 directly illustrates this mechanism where in H-charged sample, twin volume fraction at a given true strain level consistently exceeds that of H-free specimens by approximately 20–40%, while individual twin lamella thickness is concurrently reduced by 30–60%, and twin bundle spacing decreases by up to 50%. Zhang et al. [30] introduced the term HEDT after observing that H-charged TWIP steel developed thinner and more densely packed twins than that in the H-free condition. The TEM dark-field images compare H-free and H-charged specimens strained to 50%, while the statistical plots quantify twin thickness, twin spacing, and twin volume fraction at different strain levels. The results showed that H-charged specimens contain thinner and more closely spaced twins, leading to an increased twin boundary density. This is mechanically important because closely spaced twin boundaries shorten the dislocation mean free path, increase back stress, and enhance work-hardening capacity.

The HEDT mechanism can be understood as a competition between twin nucleation, twin thickening, and twin-boundary multiplication. In H-free conditions, twin embryos may need to exceed a critical thickness before they become stable and grow. In the presence of hydrogen, this threshold may be reduced because hydrogen stabilizes stacking faults and partial dislocations and increases local driving stress through dislocation pile-ups. Consequently, a larger number of twin embryos can become stable at earlier deformation stages. Instead of forming fewer thick twins, the microstructure develops many thin twins distributed within twin bundles. As schematically demonstrated in Fig. 12, hydrogen restricts twin growth after nucleation, leading to the formation of multiple thin twins rather than fewer thick ones. Additionally, twin spacing (the average distance between adjacent twin boundaries) progressively decreases with strain and becomes even smaller in H-charged specimens. For example, hydrogen reduces the twin bundle spacing from 246 nm to 183 nm, while the bundle thickness remains constant (approximately 310 nm) [12]. This morphological refinement is a key feature of the HEDT effect.

HEDT has been proposed as a robust mechanism for improving plasticity [25,30]. Densified twins during HEDT create a gradient microstructure that impedes strain localization and suppresses void coalescence. This refined twin morphology has two major mechanical consequences. First, the increased twin boundary density provides more effective barriers to dislocation glide, increasing work-hardening. Second, the finer twin spacing promotes more homogeneous grain subdivision, which can delay localized

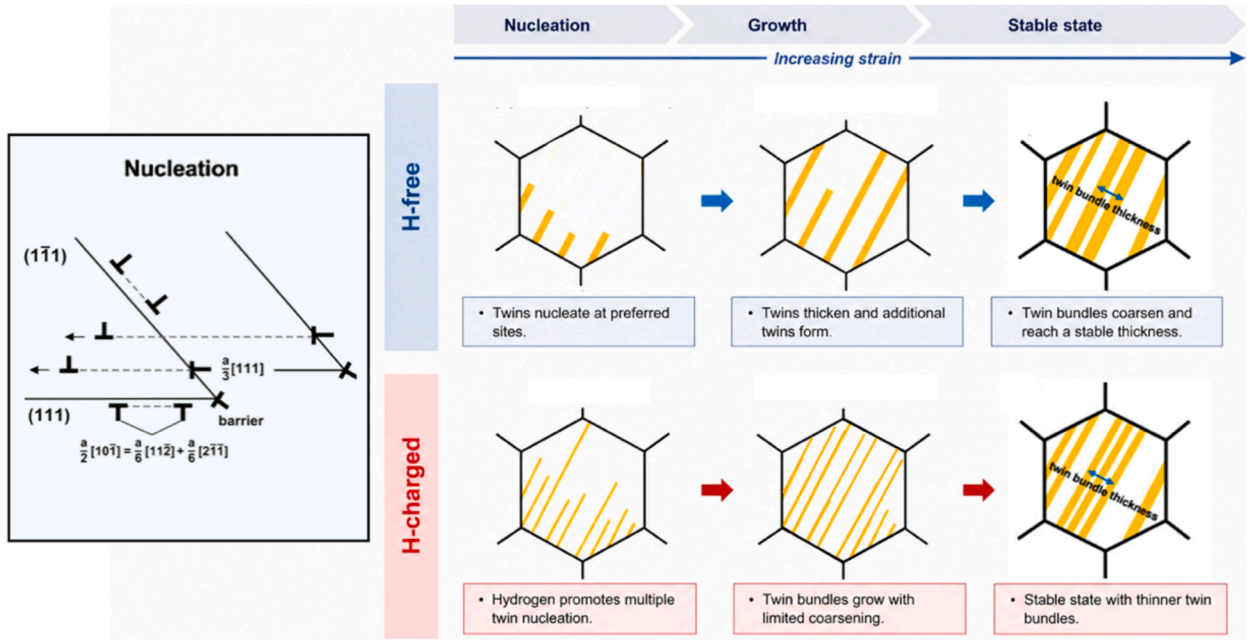


Fig. 12. Schematic representation of the hydrogen effect on the deformation twinning evolution in TWIP steel during straining, comparing the twinning behavior under H-free and H-charged conditions across the nucleation, growth, and stable-state stages. Note that twin bundles are indicated by two-way arrows. Modified and reproduced from Zhang et al. [30].

deformation and necking. These effects explain why HEDT can contribute to hydrogen-enhanced ductility in some TWIP and lightweight austenitic steels.

4.2. Hydrogen-Enhanced deformation banding (HEDB)

Hydrogen-enhanced deformation banding (HEDB) and Hydrogen-enhanced microbanding (HEMB) (cf. **Section 4.3**) are other relevant mechanisms shifting the paradigm of hydrogen–material interactions in austenitic steels with moderately high SFE (approximately 50–60 mJ/m^2 or higher). These mechanisms are particularly relevant in Fe–Mn-(Ni)–Al–C systems, where Al increases the initial SFE considerably, and hydrogen uptake significantly alters the deformation mechanisms by promoting localized planar slip and band formation.

HEDB refers to the hydrogen-assisted development of mesoscale deformation bands that redistribute plastic strain across grains or clusters of grains. Unlike HEDT, in which the central microstructural feature is the refinement and multiplication of twin boundaries. In HEDB, the central feature is the spatial organization of plastic strain into deformation bands. These bands may cut across grains, interact with grain boundaries, and operate as organized paths for plastic flow. Their mechanical importance lies in their ability to redistribute strain and prevent severe localization, if they do not become crack-initiation paths. Hydrogen can promote deformation banding by enhancing planar slip and increasing the persistence of slip on selected {111} planes. When cross-slip is reduced and dislocation glide becomes more planar, plastic strain is more likely to organize into bands rather than into a three-dimensional dislocation cell structure. In high-SFE steels, this provides an alternative route to work-hardening when twinning is less dominant.

Gutierrez-Urrutia et al. [24,121] reported that in an austenitic Fe–30Mn–6.5Al–0.3C low-density steel, hydrogen exposure produced a moderate increase in the YS and an increase in elongation to fracture attributed the improved response to hydrogen-enhanced deformation banding and microbanding. This indicates that hydrogen-induced strain localization is not necessarily harmful. If localization is distributed, repeatedly subdivided, and coupled with sufficient work-hardening, it can improve the macroscopic mechanical response. Deformation bands are helpful only when they remain stable carriers of plasticity. However, if the bands become intense crack-initiation paths or intersect brittle grain boundary precipitates, martensite/austenite interfaces, or hydrogen-enriched weak interfaces, the same process may accelerate fracture. Thus, HEDB should be understood as a mesoscale strain-partitioning mechanism whose outcome depends on the surrounding microstructure.

4.3. Hydrogen-Enhanced microbanding (HEMB)

Hydrogen-enhanced microbanding (HEMB) is closely related to HEDB, but it occurs at a finer structural scale. While HEDB describes the mesoscale organization of strain into deformation bands, HEMB refers to the formation and refinement of narrow dislocation-rich microbands (MBs), often bounded by geometrically necessary boundaries (GNBs), dense dislocation walls, or domain boundaries. In other words, HEDB describes where plastic strain is spatially concentrated, whereas HEMB describes how the internal dislocation structure evolves within or around those regions. MBs are narrow, shear-dominated regions of localized deformation aligned at 30–45° to the loading axis that accommodate plastic strain in a more homogeneous manner. Hydrogen promotes their formation by suppressing cross-slip and stabilizing planar slip, which collectively leads to a multiscale hardening effect. As MBs

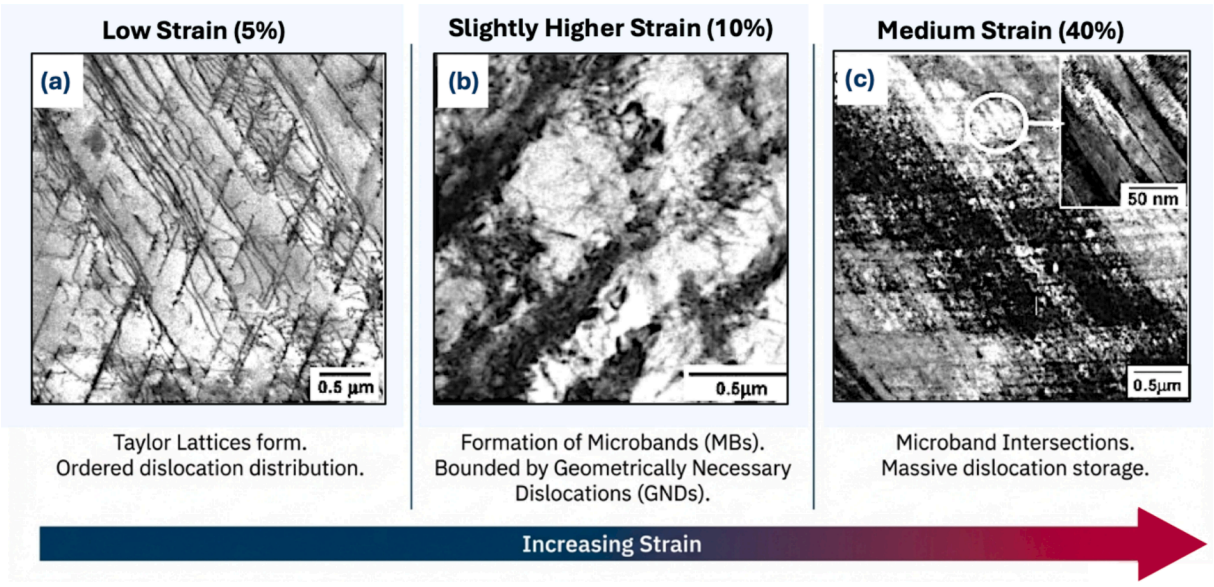


Fig. 13. TEM micrographs illustrating the formation and evolution mechanism of microbands in a Fe–28Mn–9Al–0.8C steel at different strain levels during room-temperature tensile deformation: (a) 5%, (b) 10%, and (c) 40%. Created based on the results reported by Yoo et al. [122].

intersect grains and subgrains, they can act as an effective barrier for dislocation motion, thereby improving both strength and ductility. The simultaneous formation of MBs and mechanical twins produces a complex, hierarchical deformation structure that not only enhances work-hardening but also mitigates the susceptibility of the material to hydrogen embrittlement.

At relatively high SFE regimes, especially when mechanical twinning is suppressed even in the presence of hydrogen, MBs can form and develop along localized crystallographic planes and host a dense network of geometrically necessary dislocations (GND). These MBs are characterized by high dislocation densities and efficient strain partitioning. As an example, Yoo et al. [122] demonstrated that in a high-Mn austenitic steel with high Al and moderate C content (Fe–28Mn–9Al–0.8C) possessing an SFE of around 85 mJ/m^2, dislocation glide and microbanding are the dominant deformation mechanism rather than twinning. MBs form along well-defined crystallographic planes and intersect to assist in the formation of dense dislocation networks that act to impede dislocation motion. This interaction suppresses dislocation cell formation, thereby enhancing strain partitioning and contributing to superior work-hardening.

Fig. 13 shows the progressive evolution of MBs in a Fe–28Mn–9Al–0.8C steel at increasing strain levels. The process typically proceeds through the following stages:

i) Dislocation rearrangement: at an early stage of straining, dislocations lack the mobility to form the cell structures typical of other metals. Instead, they rearrange into a Taylor lattice (a kind of low-energy dislocation structure), which is a homogeneous distribution of dislocations with a planar order and alternating senses to lower stored energy (Fig. 13**a**).

ii) Formation of domain boundaries: as strain increases, crystallographic boundaries called domain boundaries (DBs) or GNBs form between different Taylor lattice domains. These boundaries consist of GNDs that accommodate the misfit orientation between the domains (Fig. 13**a**).

iii) Development of the microband: further deformation promotes a second dislocation wall parallel to the initially formed boundaries, thereby further reducing the associated strain energy. The narrow region enclosed by two parallel walls is defined as an MB (Fig. 13**b**). These MBs are often oriented along the trace of active slip planes and end at grain boundaries or DBs. At high strains, the

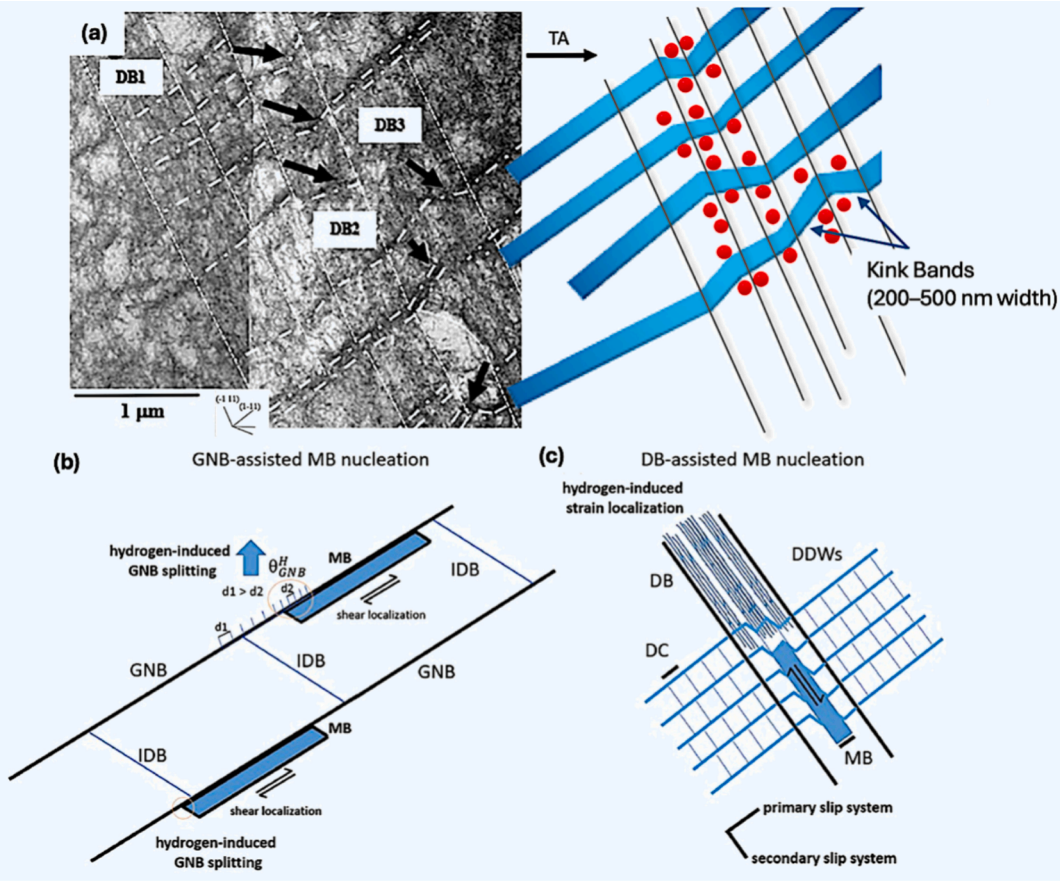


Fig. 14. (a) Schematic and BF-STEM image of the dislocation substructure revealing deformation bands in a grain oriented approximately along the [9 7 12]//TA direction in the H-charged specimen. The image was acquired under two-beam conditions using a (111)-type diffraction vector. (b) Schematic of the hydrogen-induced GNB-assisted MB nucleation and (c) DB-assisted MB nucleation. Denotation: DDW: dense dislocation wall, IDB: incidental dislocation boundaries, DC: dislocation cells, DB: domain boundary and TA: tensile axis. Adapted from the results reported by Gutierrez-Urrutia et al. [24].

intersection of multiple MBs causes grain subdivision, which increases the total dislocation density and leads to continuous work-hardening (Fig. 13**c**) [122].

Hydrogen plays a multifaceted role in this process. Within the framework of HEP, hydrogen interacts with the dislocation substructure, reduces the Peierls barrier for dislocation motion, and facilitates the formation of slip bands and MBs. As reported by Yoo and Park [122], Koyama et al. [105] and more recently by Gutierrez-Urrutia et al. [24], in H-charged Fe–Mn–Al–C specimens, the presence of hydrogen promotes the initiation of MBs at lower strain levels and increases their number. This observation suggests that hydrogen enhances both nucleation and propagation of these localized deformation features. The TEM investigation of hydrogen pre-charged samples revealed more refined and intersecting MB structures compared with H-free counterparts, indicating that hydrogen stimulates additional slip activity and increases the overall dislocation density. As shown in Fig. 14 (domain boundaries DB1–DB3 and kink bands), hydrogen promotes MB nucleation through two coupled mechanisms. First, GNB-assisted nucleation as the dominant pathway which occurs through hydrogen-enhanced storage of GNDs along pre-existing GNBs. According to the boundary-splitting model originally proposed by Hughes [123], GNBs (which are formed due to strain-induced dislocation pile-up and misorientation) undergo localized splitting under applied stress. The introduction of hydrogen enhances this process by increasing local strain incompatibilities, thus raising the misorientation across GNBs during deformation. Hydrogen increases GNB misorientation (from approximately 2–3° up to 2–8°), indicating localized boundary splitting. This process results from enhanced dislocation pile-up stabilization due to elastic shielding, which promotes dense dislocation configurations and localized shear. Microbands nucleate preferentially along these higher-misorientation GNB segments (Fig. 14**b**).

In a complementary mechanism, identified as DB-assisted nucleation and illustrated in Fig. 14**a** and Fig. 14**c**, hydrogen intensifies macroscopic and submicron deformation banding. Inside these bands, a massive glide of secondary dislocations shears the pre-existing dense dislocation walls /dislocation cells structure, forming kink bands and closely spaced dislocation sheets (approximately 150–200 nm thick) that evolve into MBs. Cross-slip is not fully suppressed; rather, internal stresses within DBs enable cross-slip and dislocation reactions that stabilize the MB structure. The evolution of these sheets into stabilized MBs is driven by two parallel phenomena: first, the high local stresses generated within deformation bands may activate limited cross-slip and dislocation reactions, facilitating local dislocation rearrangement and annihilation during MB formation; second, the formation of sessile Lomer–Cottrell locks at the intersections of active slip systems contributes to the mechanical stabilization of the evolving MBs. Crystallographic analysis confirmed that MBs are preferentially formed within DB regions, as further evidenced by ECCI of regions that contain both DBs and newly formed MBs [121].

The key mechanical effect of this microbanding is an increased work-hardening capacity, which translates into simultaneous improvement in YS and ductility, a rare synergy in materials engineering. Experimental stress–strain tensile results of hydrogen-charged specimens showed both higher YS and significantly extended uniform elongation compared with their uncharged counterparts. This is because MBs act as barriers to dislocation motion, thereby enhancing work-hardening, while H-induced planar glide facilitates dislocation motion in the early stages of deformation. This combined effect delays the onset of necking and contributes to the simultaneous improvement in strength and ductility. Moreover, microbanding offers a more uniformly distributed plasticity mechanism than twinning or martensitic transformation. This promotes the dispersion of deformation across a larger number of grains and mitigates the severity of local stress concentrations, which typically serve as crack initiation sites in embrittled materials. In this regard, microband-induced plasticity not only enhances mechanical performance but may also partially alleviate HE, provided that the hydrogen concentration remains below a critical threshold.

The effectiveness of HEMB and HEDB strongly depends on alloy composition, hydrogen concentration, and the method of hydrogen charging. For instance, in-situ gaseous charging during deformation may provide a more homogeneous distribution of hydrogen that promotes planar slip and microbanding without inducing premature decohesion or crack nucleation at grain boundaries. On the other hand, aggressive electrochemical pre-charging may localize hydrogen at microstructural heterogeneities, reversing the beneficial effects and reintroducing embrittlement phenomena.

4.4. Hydrogen-Enhanced hardening (HEH)

Hydrogen-enhanced hardening (HEH) in austenitic steels and other FCC metals/alloys is a conventional observation. Yield and flow stress increases after hydrogen charging have been reported for decades [124,125]. More recent, however, is the recognition that this strengthening can, under selected conditions, contribute to a net improvement in the strength–ductility balance rather than simply preceding embrittlement.

More recently, Ogawa et al. [17] demonstrated that solute hydrogen in Fe–24Cr–19Ni ASS increased YS, flow stress, UTS, uniform elongation, and strain-to-failure. The improvement became more pronounced with increasing hydrogen concentration. In another work [21], they emphasized that the solute hydrogen in this Fe–Cr–Ni ASS can produce a magnitude of solid-solution hardening comparable to that of C and N, despite causing only a fraction of their lattice expansion. They proposed that the strengthening is attributed not only to elastic lattice distortion, but also to dynamic hydrogen–dislocation interactions, including solute drag (i.e., drag associated with a hydrogen Cottrell atmosphere), diffusion-controlled dislocation glide (i.e., cooperative motion of segregated hydrogen with the local dislocation core), and possible hydrogen–substitutional atom complexes (e.g., with Cr). This distinction is important as the conventional explanation for interstitial solid-solution hardening in austenite is based largely on the elastic interaction between dislocations and local lattice strain around interstitial atoms.

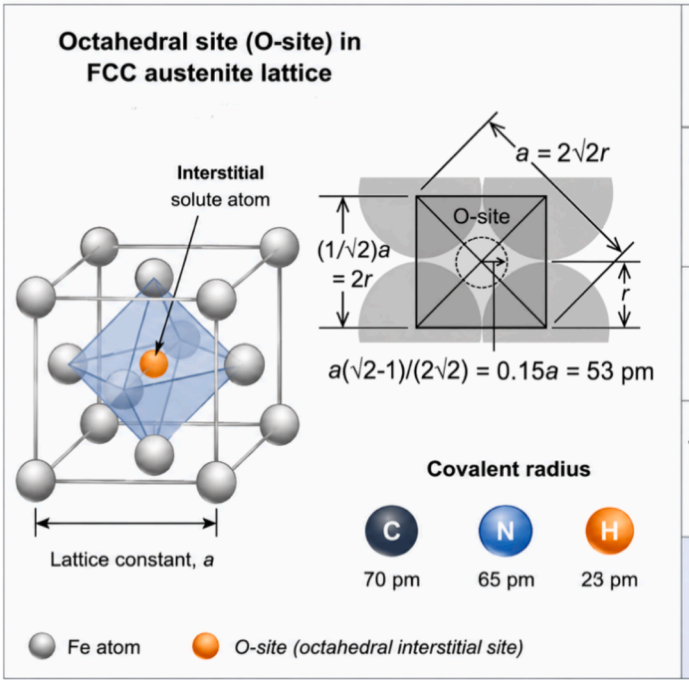
C and N occupy octahedral interstitial sites in FCC austenite and generate relatively large local lattice distortion. In contrast, hydrogen has a much smaller covalent radius and produces a smaller lattice volume expansion per atom [126]. As summarized schematically in Fig. 15, C and N have similar lattice volume expansion values of approximately 8.6×10^{-3} nm^3 per atom, whereas

hydrogen produces only about 2.3×10^{-3} nm^3. This latter value was experimentally derived from the neutron diffraction analysis by Ito et al. [21], who measured a volume expansion of 2.27 Å^3 per hydrogen atom in Fe–24Cr–19Ni austenitic steel. This indicates a further paradox: hydrogen causes a much smaller static lattice distortion than C or N, yet it can generate a comparable increase in YS in Fe–Cr–Ni ASSs. Thus, hydrogen-induced strengthening cannot be rationalized by lattice expansion alone.

The second important factor illustrated in Fig. 15 is the significantly higher mobility of hydrogen at room temperature. C and N are essentially immobile during room-temperature deformation of austenite, with jump frequencies on the order of 10^{-4} s^{-1} at 300 K. Hydrogen, by contrast, exhibits a jump frequency on the order of up to 10^5 s^{-1}. Thus, C and N behave mainly as static or quasi-static interstitial obstacles, whereas hydrogen can redistribute quickly among lattice sites, dislocations, stacking faults, grain boundaries, and other weak traps during deformation. This makes hydrogen a fundamentally different type of solute strengthener: it is not simply a fixed barrier in the slip plane, but a mobile interstitial alloying element capable of interacting continuously with moving dislocations. Similarly, C and N can also undergo dynamic interactions with dislocations and give rise to dynamic strain aging once the temperature is high enough for their diffusion. However, the distinctive feature of hydrogen is that such behavior can occur even at room temperature.

Fig. 16**a** places this hydrogen-induced strengthening effect at ambient temperature in direct comparison with C and N. Again, the plotted data show that hydrogen-induced YS increments in Fe–Cr–Ni austenitic steels fall within the same order of magnitude as those produced by C and N. This is consistent with the recent comparative work by Nishida et al. on Fe–15Cr–15Ni steel [15,16,19], where both hydrogen and C produced solid-solution hardening of comparable magnitude. C in solid solution in Fe–Mn–C TWIP steels contributes approximately 20–30 MPa per 0.1 wt% C via solid-solution hardening. Similarly, the hydrogen-induced flow stress increment is of the order of 20–40 MPa at hydrogen concentrations of ~ 2000–4000 at.ppm for both Fe–Ni–Cr ASSs and Fe–Mn–Al–C steels [24,127–129], which is comparable per unit solute concentration. Particularly at room temperature, the process by which dislocations move while overcoming the resistance imposed by both these elements is primarily thermally activated, and the deformation resistance decreases with decreasing strain rate. However, the magnitudes of their effects on such thermally activated dislocation motion are clearly different: hydrogen produces a much greater increase in strain-rate sensitivity than C, implying that hydrogen acts as a highly localized barrier, whereas C behaves as a relatively longer-range and less rate-sensitive barrier [129].

The mechanistic map given in Fig. 16**b** schematically illustrates the overall behavior of HEH in Fe–Cr–Ni–based alloy systems. At low temperatures or high strain rates, hydrogen diffusion is too slow to follow dislocation motion effectively. In this regime, hydrogen may behave more like randomly dispersed interstitial atoms or hydrogen–substitutional atom complexes. At higher temperatures and/or lower strain rates, hydrogen can dynamically redistribute with moving dislocations, producing solute drag or diffusion-controlled glide. Ogawa et al. [17] proposed that hydrogen-induced solid-solution hardening is maximized when these dynamic interactions between diffusible hydrogen and mobile dislocations dominate the flow stress. The Peak Hardening Region in Fig. 16**b** therefore represents the kinetic window where hydrogen is mobile enough to interact with dislocations but not so mobile that it simply relaxes



Interstitial solute atom	Carbon (C)	Nitrogen (N)	Hydrogen (H)
Lattice Volume Expansion (ΔV, nm^3)	8.6×10^{-3} nm^3	8.6×10^{-3} nm^3	2.27×10^{-3} nm^3
Lattice Volume Expansion ($\Delta V/V$, %)	0.90	0.90	0.24
Jump Frequency at 300K (Γ, s^{-1})	10^{-4} s^{-1}	10^{-4} s^{-1}	10^5 s^{-1}

ΔV: absolute lattice volume expansion caused by solute atom
$\Delta V/V$: relative lattice volume expansion
Γ: atomic jump frequency

Fig. 15. Schematic illustration of the octahedral interstitial site (O-site) in the FCC austenite lattice according to the rigid-sphere model, together with the relative covalent radii of the interstitial solute atoms hydrogen, C, and N, the absolute and relative lattice volume expansion by each solute atoms, and their atomic jump frequency. Adapted from Ogawa et al. [17].

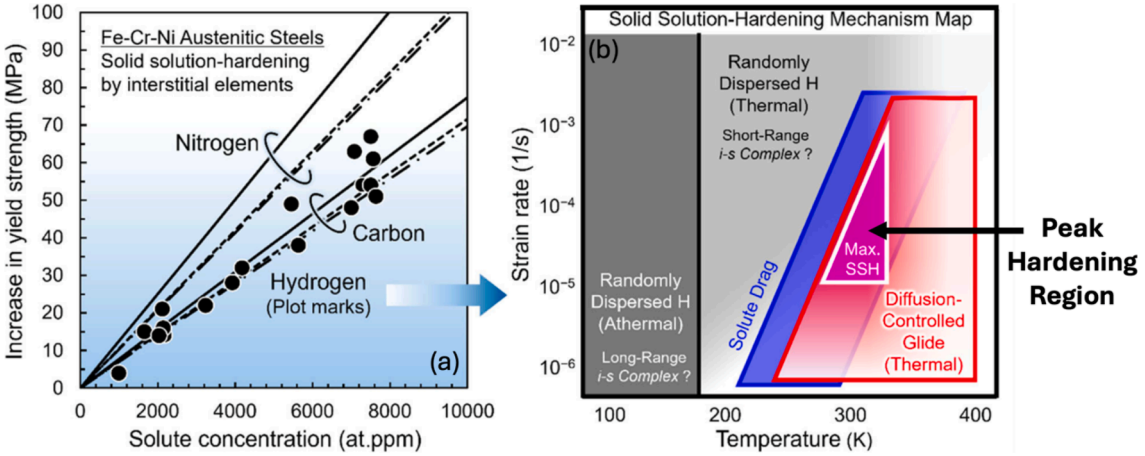


Fig. 16. (a) Effect of C, N, and hydrogen content on the solid-solution hardening response of Fe–Cr–Ni ASSs at ambient temperature. (b) Proposed temperature- and strain-rate-dependent evolution and synergy of the mechanisms governing hydrogen-induced solid-solution hardening at yielding. The fading intensity of the colored areas denotes the progressive reduction in the contribution of each mechanism. Abbreviations: SSH, solid-solution hardening; i–s, interstitial–substitutional interactions. Adapted from Ogawa et al. [17].

the local stress field without contributing resistance.

As already mentioned, while such macroscopic hardening has often been observed, the field of HE has long maintained a strong belief in the HELP mechanism. In HELP, hydrogen is considered to enhance dislocation mobility by shielding the elastic stress field around dislocations. In contrast, Ogawa's stress relaxation, strain-rate sensitivity, and creep studies show that hydrogen can act as a thermally activatable barrier against dislocation glide. These two effects are not necessarily mutually exclusive; rather, they may occur in different kinetic regimes. In mechanical testing, most mobile dislocations must move collectively at a rate high enough to be detected by the testing machine as a finite strain rate. In such a case, the resistance imposed by hydrogen on dislocations moving at relatively high velocities is likely detected as an increase in the flow stress. On the other hand, if a small number of dislocations in a localized region of the material move slowly enough that they do not experience the resistance from the dragging hydrogen atmosphere, an increase in dislocation mobility, as assumed in the HELP mechanism, is not impossible, even though it cannot be detected as a decrease in flow stress. Therefore, hydrogen should not be treated as a purely hardening or purely softening solute. Its effect depends on the competition between hydrogen diffusion and dislocation velocity, as well as on the local mechanical state during deformation.

As already discussed, an important secondary outcome of hydrogen strengthening is the indirect facilitation of mechanical twinning. As schematically illustrated in Fig. 17, hydrogen charging elevates yield and flow stresses, thereby reducing the strain required to reach the critical stress for twin nucleation during plastic deformation. Consequently, deformation twinning is activated earlier and more extensively, contributing to a higher work-hardening rate and delaying the onset of necking or plastic instability. This earlier onset of twinning leads to a refinement of microstructure through the dynamic Hall-Petch effect, in which twins subdivide the grains and impede dislocation glide, thereby contributing positively to both strength and ductility.

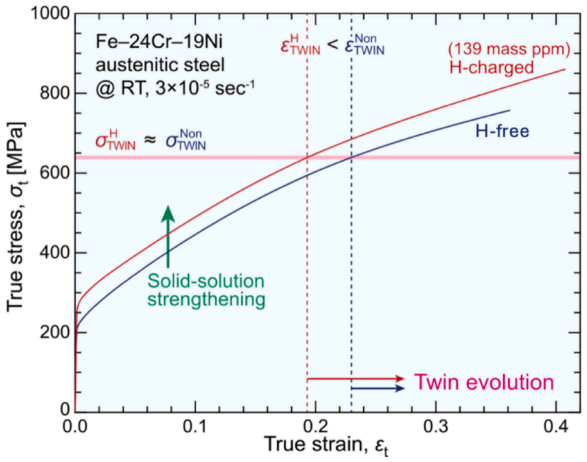


Fig. 17. Schematic representation of hydrogen-assisted twinning in Fe–24Cr–19Ni ASS as a result of hydrogen-induced solid-solution strengthening and elevated flow stress [21].

However, this beneficial strengthening–twinning pathway has clear limits. León-Cázares et al. [120] showed in single-crystal 316 L ASS that hydrogen increases the critical resolved shear stress without causing a clear deviation from Schmid's law, supporting the idea that hydrogen can raise the intrinsic resistance to slip. At the same time, their AFM and EBSD analyses demonstrated that hydrogen strongly enhances slip localization in both single- and multiple-slip orientations; the most active slip bands accumulated substantially higher deformation in hydrogen pre-charged specimens, with consequences for damage initiation. This indicates that HEH may increase strength while simultaneously concentrating plastic strain into fewer active slip bands, providing a link between solute strengthening and HELP-type localized deformation.

A similar observation is provided by the high-Mn TWIP steel study of Khanchandani et al. [99]. In Fe–26.9Mn–0.28C steel, hydrogen charging produced a hardened surface layer and a yield strength increased by about 20%, but this was accompanied by a severe loss of ductility from about 75% to 10%. Their correlative EBSD/ECCI/APT analysis suggested that hydrogen segregation to grain boundaries delayed dislocation emission by blocking dislocation sources, promoting early activation of multiple slip systems and dislocation cell-like structures. With increasing strain, these structures evolved toward stacking faults and strain-induced ε-martensite in the hydrogen-charged region. Therefore, HEH may readily transition from beneficial strengthening to localized deformation and premature fracture, especially when hydrogen segregation, planar defects, or martensitic transformation become dominant.

4.5. Preliminary unified mechanism map

Earlier twinning, increased twin or microband density, and enhanced work-hardening after hydrogen exposure are experimentally observed responses, but they do not, by themselves, identify the controlling mechanism. These responses may arise from several concurrent pathways, including hydrogen-induced solid-solution strengthening that allows the twinning stress to be reached at a lower strain, changes in dislocation mobility and cross-slip, increased planar slip or stacking-fault probability, and local effects associated with hydrogen-concentration and stress gradients. Mechanistic interpretations such as direct stabilization of dissociated partial dislocations or twin embryos are therefore presented with confidence proportional to the available experimental and computational evidence and are not assumed to apply universally across alloy systems or charging conditions. Moreover, the mechanisms discussed above are not isolated. HET, HEDT, HEDB, HEMB, and HEH can operate concurrently or sequentially within the same alloy. Table 4 summarizes their main characteristics, indicative SFE regimes, and key supporting evidence.

Building on the evidence summarized in Table 4, Fig. 18 integrates these mechanisms into a preliminary schematic illustrative, condition-dependent framework describing the competition between hydrogen-enhanced plasticity and hydrogen-assisted damage. Rather than defining fixed mechanism boundaries, the map identifies approximate response regimes governed by the combined effects of initial SFE, hydrogen content and distribution, microstructural state, and loading conditions.

A useful way to interpret the map is to separate the response into three broad regimes: a risk zone, a transition zone, and a target zone. In the low-SFE risk zone, hydrogen-assisted planar slip, SF accumulation, ε- or α'-martensite formation, and twin/grain boundary cracking can dominate. In this regime, hydrogen-enhanced localization is likely to intersect crack-sensitive interfaces, resulting in embrittlement rather than ductility improvement. This is typical of metastable austenitic steels or low-SFE high-Mn steels when hydrogen concentration, strain localization, or interfacial susceptibility is high.

In the transition zone, twinning is accessible but not necessarily damaging. Here, moderate hydrogen concentrations may promote HET or HEDT. If twin formation increases work-hardening and delays necking, hydrogen may improve ductility. However, if hydrogen segregates strongly to twin boundaries or if twin/grain-boundary intersections become crack-initiation sites, the same mechanism becomes harmful. This explains why twinning is not inherently beneficial or detrimental; its effect depends on the stability of the surrounding microstructure and the spatial distribution of hydrogen.

In the high-SFE target zone, ε-martensite formation and excessive twinning are suppressed. In this regime, hydrogen-enhanced deformation banding, microbanding, and solid-solution strengthening can become dominant. This is especially relevant to Al-containing Fe–Mn–Al–C steels and stable Fe–Cr–Ni ASSs. In these materials, hydrogen-assisted plasticity may contribute to higher flow stress, increased back stress, stable strain partitioning, and delayed plastic instability. This is the regime where HEP is most likely

Table 4
Summary of the proposed hydrogen-enhanced deformation and strengthening mechanisms, their experimental signatures, indicative initial SFE regimes, and principal supporting evidence. The SFE ranges are approximate and condition-dependent rather than universal thresholds.

Mechanism	Signature	SFE Regime	Key Evidence	Representative References
HET (4.1.1)	Earlier onset/ increased incidence of twin nucleation at a given strain	Intermediate, ~40–45 mJ/m^2 (original)	WBDF-TEM: increased partial-dislocation separation	[18,28]
HEDT (4.1.2)	Thinner, more closely spaced twins at a given strain compared with HET	High, > 45 mJ/m^2, high H content	Statistical TEM twin-thickness /spacing distributions	[12,30]
HEDB (4.2)	Mesoscale deformation bands redistributing strain	Moderately high, ~50–60 mJ/m^2	EBSD/ECCI banded-slip evidence. Reported for a limited set of high-hydrogen FCC conditions.	[24,121]
HEMB (4.3)	Narrow GND-rich microbands bounded by GNBs/DDWs	High, twinning-suppressed FCC microstructures	TEM/ECCI: GNB splitting, microband density	[24,122]
HEH (4.4)	Increased yield/flow stress, minimal SFE/SFP change	Stable Fe–Cr–Ni austenite	Tensile test, neutron diffraction, Haasen-plot activation volume	[17,21]

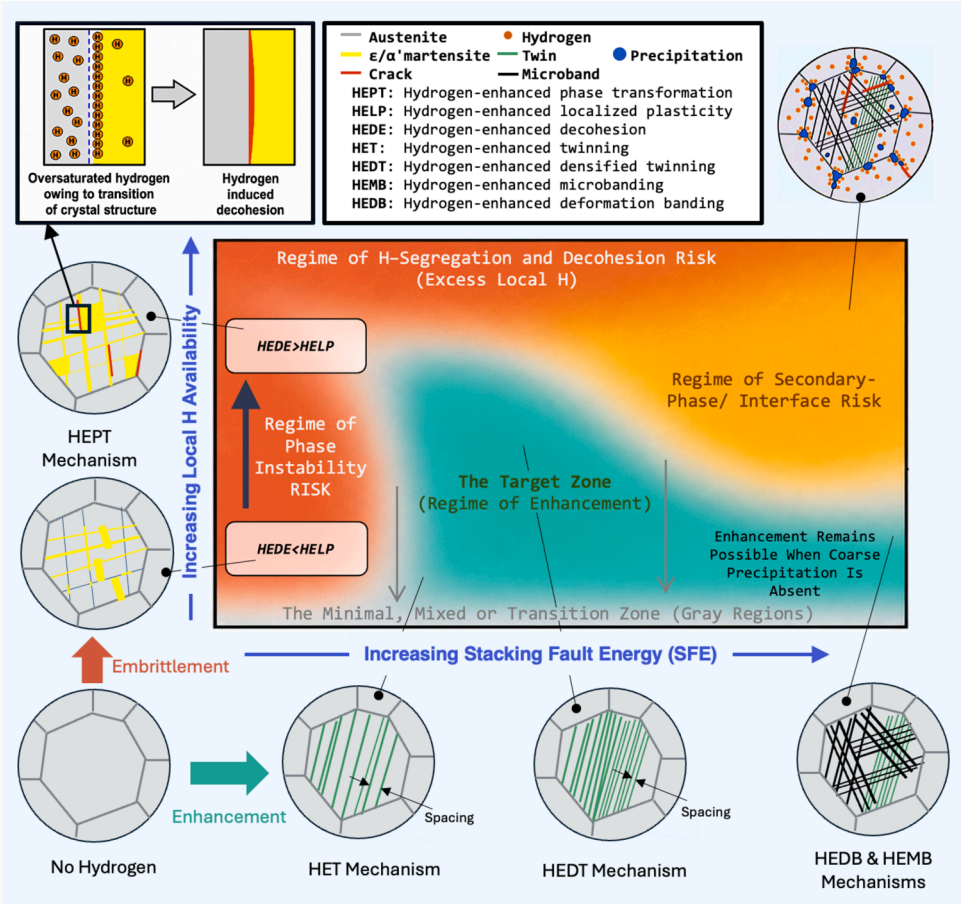


Fig. 18. Conceptual mechanism map showing the condition-dependent transition between hydrogen-assisted damage and hydrogen-enhanced plasticity as functions of chemical composition, original SFE, hydrogen content, and microstructural sensitivity. Gradient boundaries denote approximate transitions rather than universal thresholds. The "No Hydrogen" state represents the unloaded, hydrogen-free reference state; all other schematics represent hydrogen-containing microstructures subjected to sufficient loading to activate the indicated mechanisms. The required loading level depends on alloy composition, microstructure, hydrogen distribution, strain rate, and stress state.

to produce a net improvement in mechanical properties. However, high SFE alone does not guarantee a beneficial response. A separate risk zone exists at high SFE when brittle interfaces, grain boundary κ-carbides, coarse precipitates, inclusion networks, or severe hydrogen gradients dominate the fracture process. In such cases, hydrogen may bypass beneficial plasticity mechanisms and instead promote interface decohesion or crack initiation. Therefore, the mechanism map should include not only SFE and hydrogen content but also microstructural sensitivity, as will be further discussed in **Section 5** for grain size effects and κ-carbide/B2 precipitation.

To make the interplay among these parameters more tangible, we consider a deliberately illustrative "what-if" scenario. Suppose that an austenitic steel initially exhibits a relatively high SFE, favoring dislocation slip over deformation twinning under hydrogen-free conditions, and subsequently absorbs a sufficiently high concentration of hydrogen during electrochemical charging. If hydrogen were to reduce its effective SFE by an amount comparable to the larger reductions reported in the literature and summarized in Fig. 4, the deformation landscape could shift toward a regime in which deformation twinning becomes more favorable and competitive with dislocation slip. In parallel, if hydrogen–dislocation interactions facilitate partial-dislocation activity and reduce the effective stress required for their motion, earlier or denser twin activation could become possible, providing a potential HEDT-type pathway (**Section 4.1.2**). Under such circumstances, enhanced twinning may promote more distributed plasticity and could delay strain localization or crack initiation at stress concentrators. Importantly, none of these steps is inevitable, and the same underlying hydrogen–dislocation interactions need not be intrinsically beneficial or detrimental. In this sense, HEP does not fundamentally contradict HELP: hydrogen-enhanced dislocation mobility or localized plasticity may contribute to greater plastic accommodation when it remains sufficiently distributed, whereas excessive localization near stress concentrators, interfaces, or microstructural heterogeneities may instead facilitate damage initiation. For example, if the same alloy contains a high density of incoherent κ-carbides or other strong trapping interfaces, preferential hydrogen accumulation at these sites could promote local interfacial weakening and favor HEDE-type damage rather than a beneficial twinning-assisted response. This hypothetical scenario is therefore intended to illustrate the competition between possible beneficial and detrimental pathways, rather than to define a deterministic sequence of events. It further emphasizes

Table 5
Representative studies on grain size effects in hydrogen embrittlement of FCC steels. Additional details on hydrogen content and sample dimension are provided in Supplementary Table S3.5.

Alloy System	Grain Size/s, μm	Strain Rate, s^{-1}	Charging Condition*	HAA, μm	HAA, %	HE Resistance	Fracture Mode by H	Ref.
Fe–31Mn–3Al–3Si–C	0.6, 1.5, 19	8×10^{-6}	48 h EC.	Not reported	Not reported	↑, HEP in GS 0.6	Ductile fracture for all; secondary cracks (>100 μm) in CG only, fewer in FG, almost none in UFG.	[8]
Fe–16Cr–10Ni–C	1, 6, 10, 12, 21	10^{-5}	72 h Gas. at 270 °C & 10 MPa pressure	Not reported	Not reported	↑	IG fracture in GS 21 μm → fully ductile fracture in GS 1 μm	[130]
ASS 304	4, 8, 12	2×10^{-5}	In-situ EC. charging	GS 4: 50 GS 8: 192 GS 12: 285	GS 4: 14 GS 8: 50 GS 12: 69	↑	QC fracture on the surface layer of all H-charged samples	[131]
Fe–22Mn–0.6C	4, 7, 20, 45	2×10^{-5}	72 & 166 h EC.	GS 4: 30–40, GS 45: 50–90, Others N/A	GS 4: 6 GS 45: 12 Others N/A	↑	IG fracture for H-charged samples regardless of grain size	[132]
Fe–17.6Mn–0.6C	6, 16, 30, 53, 80	6×10^{-5}	48 h EC.	Not reported	Not reported	↑	Ductile + IG in CG (GS > 20 μm) → fully ductile in FG	[133]
Fe–20Cr–11Ni–5Mn–0.02C–0.2 N	23, 63	6×10^{-5}	48 h EC. at 90 °C	Not reported	GS 23: 2.4 GS 63: 0.9	↓ in GS 23, ↑ in GS 63	IG + QC + microvoids regardless of grain size	[134]
18Mn–1.5Al–0.6C	23, 45	6×10^{-5}	48 h EC. at 90 °C	Not reported	GS 23: 9.2 GS 45: 14.5	↑	grain refinement improved HE resistance even though mixed IG/QC/microvoids fracture features remained.	[134]
Fe–24Mn–3Cr–0.35C	1, 6, 21	6×10^{-5}	48 h EC. at 90 °C	GS 1: 90 GS 6: 109 GS 21: 129	GS 1: 25 GS 6: 30 GS 21: 35	↓	Primarily IG + QC regardless of grain size	[94]
ASS 316 L	15, 25, 35	1×10^{-3}	168 h EC.	~40 Regardless of grain size	Not reported	↑	Brittle fracture at edges (brittle layer) and ductile bulk for all samples	[135]
ASS 304	0.5, 0.8, 1.7, 10, 35	3×10^{-4}	96 h EC. Pre-charging	GS < 1: 10 GS 35: 114	GS < 1: 2 GS 35: 23	GS < 1 ↓ Others ↑	Mixed QC + IG in ultrafine (<1 μm); QC-dominant in CG	[136]
ASS 304	0.5, 0.8, 1.7, 10, 35	3×10^{-4}	In-situ EC. charging	H-affected depth decreased with grain refinement	Not reported	↑	Finer grain suppressed IG fracture by lowering H amount per GB.	[136]
Fe–21Mn–0.55C	10–34**	5×10^{-5}	In-situ EC. charging	Not reported	Not reported	↑	Finer grains in the edge region showed delayed plastic deformation.	[137]

* EC: electrochemical charging, room temperature if temperature is not specified. Gas: Gaseous charging. **Gradient grain size distribution from the edge to the center from approx. 10 to 34 μm. Abbreviations: CG: Coarse grain, FG: Fine grain. UFG: Ultra-fine grain, ASS: Austenitic stainless steel, GS: Grain size, HE: Hydrogen embrittlement, QC: Quasi-cleavage, HAA: Hydrogen-affected area, HAA%: The ratio of HAA to the whole cross-sectional area, IG: Intergranular. Arrows indicate the effect of grain refinement on HE resistance: ↑ improved, ↓ worsened.

why neither single SFE value nor hydrogen content alone is sufficient to predict the mechanical response: the outcome emerges from their interaction with defect structure, hydrogen partitioning, phase stability, and the nature of available trapping and damage sites. Fig. 18 should therefore be presented as a synthesis framework rather than a strict predictive diagram. No single study has yet compared all the mechanisms under identical alloy, hydrogen-exposure, strain-rate, and microstructural conditions. The map is most useful to guide future systematic experiments. A complete validation would require coordinated measurements of hydrogen distribution, local SFE or SFP, twin density, MB density, dislocation structure, and crack-initiation sites during deformation.

5. Microstructure sensitivity

The response of austenitic steels to hydrogen is highly sensitive to microstructure, because hydrogen diffusion, segregation, and local enrichment are governed not only by alloy composition but also by the density, distribution, and character of internal defects, interfaces, and microstructural features. Grain size controls the balance between hydrogen diffusion pathways, grain boundary segregation, strain localization, and the activation of deformation mechanisms such as slip, twinning, and microbanding. Similarly, second phases and precipitates can either act as beneficial hydrogen traps that reduce diffusible hydrogen or become preferential sites for hydrogen accumulation, interfacial decohesion, and crack initiation. This section therefore discusses how grain size and second-phase precipitation, particularly κ-carbide and B2 phases, which are common in several of the alloys discussed in this work, modify the competition between HEP and HE in austenitic steels.

5.1. *Effect of grain size*

Grain refinement is one of the most widely used strategies for strengthening metallic materials without changing their chemical composition. In FCC austenitic steels, however, its role in the presence of hydrogen is not straightforward. Depending on alloy chemistry, SFE, hydrogen charging condition, grain boundary character, and active deformation mechanisms, grain refinement can either improve HE resistance or, in some cases, accelerate hydrogen-assisted failure. Therefore, grain size should not be considered solely as a strengthening parameter; rather, it should be considered as a microstructural variable that simultaneously controls hydrogen distribution, local stress state, deformation mechanism, and crack-path sensitivity.

Table 5 summarizes representative studies on the effect of grain size on HE in FCC/austenitic steels. The results clearly show that no universal trend exists. In several high-Mn TWIP steels and metastable ASSs, grain refinement improves resistance to hydrogen-assisted cracking by reducing strain localization, suppressing detrimental deformation products, and lowering the hydrogen concentration per unit grain boundary area. Among these studies, Bai et al. [8] provided one of the clearest demonstrations that grain refinement can strongly improve, and in the ultrafine-grained condition nearly suppress, HE in a high-Mn TWIP steel. As shown in Fig. 19, hydrogen charging reduced the elongation of the coarse-grained specimen, while the ultrafine-grained specimen retained almost the same tensile elongation after hydrogen charging. This is particularly important because the diffusible hydrogen content increased with grain refinement. Therefore, the improved HE resistance cannot be explained by lower total hydrogen uptake. Bai et al. [8] attributed this behavior to a reduction in local hydrogen segregation at individual grain boundaries. In coarse-grained specimens, a lower density of grain boundaries leads to stronger hydrogen enrichment at each boundary, which promotes secondary crack formation and premature plastic instability. By contrast, in ultrafine-grained specimens, hydrogen is distributed over a substantially larger grain boundary area, so that the local hydrogen concentration at each boundary remains below the critical level required for crack initiation.

However, some other studies have reported the opposite trend. For example, Moallemi et al. [95] observed increased HE

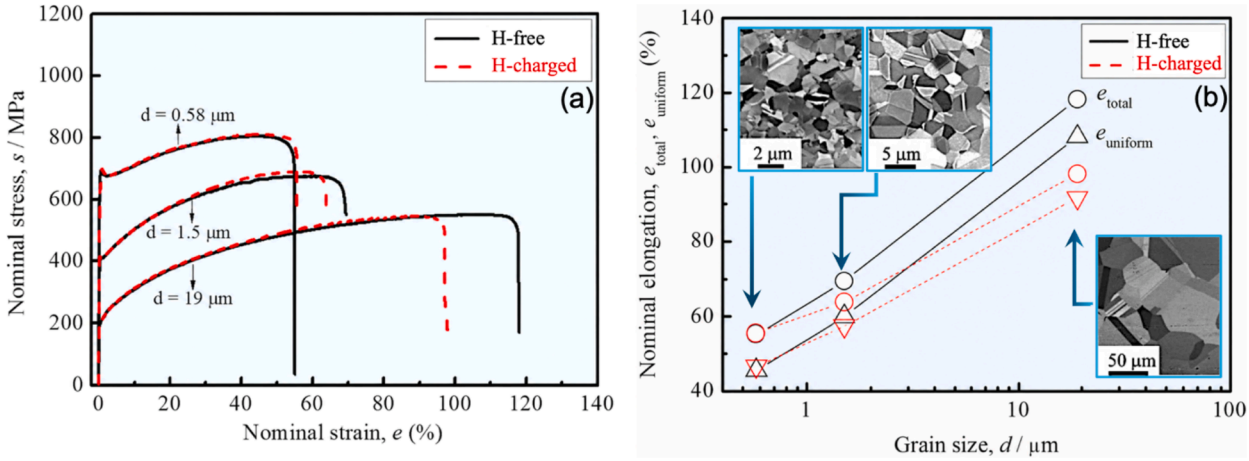


Fig. 19. Effect of grain refinement on hydrogen-affected mechanical properties of a Fe–31Mn–3Al–3Si–0.005C steel, (a) stress–strain curve for H-free and H-charged samples with different grain size distributions and (b) total and uniform elongation of the same samples as a function of grain size. Modified and reproduced from Bai et al. [8].

susceptibility with grain refinement in a Fe–24Mn–3.1Cr–0.35C high-Mn austenitic steel. This behavior was attributed to the more rapid degradation of the hydrogen-affected layer in fine-grained specimens and the larger ratio of the hydrogen-affected layer to the specimen cross-section compared with those reported in previous studies, which collectively intensified hydrogen-induced damage. Similarly, Wang et al. [136] showed that ultrafine-grained 304 ASS exhibited greater HE susceptibility after pre-charging, as grain boundaries served as hydrogen reservoirs. In contrast, grain refinement was found to improve the resistance under in-situ hydrogen charging conditions, highlighting the strong dependence of the grain-size effect on the hydrogen distribution within the microstructure.

These apparently conflicting results can be rationalized by considering four interconnected effects of grain refinement on hydrogen-affected mechanical and microstructural response:

First, grain refinement increases the total grain boundary area and changes the distribution of hydrogen among boundaries. Grain boundaries can serve as weak or moderate hydrogen trapping sites. If the total amount of absorbed hydrogen is distributed over a much larger boundary area, the local hydrogen concentration per unit boundary area decreases. This "hydrogen dilution" effect lowers the probability of grain boundary decohesion and can suppress intergranular cracking. Bai et al. [8] showed that grain refinement can reduce the hydrogen amount per grain boundary area even when the total diffusible hydrogen content increases. However, this beneficial effect only applies when the hydrogen occupancy of each boundary remains sufficiently low. If the refined microstructure absorbs too much hydrogen, the larger number of grain boundaries may instead act as a high-capacity hydrogen reservoir, supplying hydrogen to stress-concentrated regions during deformation.

Second, grain refinement affects the effective SFE and austenite stability. Although chemical composition is the primary factor controlling SFE, grain size can modify the apparent or effective SFE. Fig. 20 shows the calculated SFE for the material studied by Bai et al. [8] as a function of grain size, using Saeed-Akbari et al.'s thermodynamic model [138] which considers the effect of grain size on SFE. Although Bai et al. [8] reported that the SFE of their material was estimated to be below 40 mJ/m^2, the calculation indicates that grain refinement can still increase the effective SFE and thereby influence the dominant deformation mechanism. Fig. 20 clearly shows that decreasing grain size increases the SFE, and for the ultrafine-grained condition, the SFE approaches or exceeds the critical value of approximately 40 mJ/m^2 discussed in **Sections 1 and 4**. As described in the HEP-based interpretation presented earlier, FCC alloys with original SFE values above this threshold generally exhibit lower HE susceptibility. Therefore, the excellent HE resistance reported by Bai et al. [8] for the ultrafine-grained TWIP steel can be correlated not only with the reduction in hydrogen concentration per grain boundary area, but potentially also with the grain-refinement-induced increase in effective SFE into a regime associated with minimal HE according to the HEP framework. In hydrogen-containing conditions, this effect competes with the tendency of hydrogen to reduce the local effective SFE. Therefore, the final deformation mechanism is determined by the balance between two opposing effects: grain refinement tends to raise SFE and stabilize austenite, whereas hydrogen charging can locally reduce SFE and promote stacking faults or twinning. The resulting bulk response may therefore differ from the local response in hydrogen-enriched regions, especially near specimen surfaces or grain boundaries.

Third, grain refinement changes the grain boundary character distribution. A refined microstructure does not automatically improve HE resistance; the type of boundary also matters [139]. Special boundaries, particularly coherent Σ3 twin boundaries, are generally more resistant to intergranular decohesion than random high-angle grain boundaries [140,141]. In contrast, random high-angle grain boundaries can provide easy paths for intergranular cracking if they become hydrogen enriched. Thus, the beneficial effect of refinement depends not only on the amount of boundary area but also on whether the processing route increases special boundaries or creates a large population of random, highly stressed, hydrogen-sensitive interfaces.

Fourth, and importantly, grain refinement changes the critical stress for deformation twinning and therefore modifies the active deformation mechanism. Zan et al. [132] showed that the critical stress for twinning follows a Hall–Petch-type dependence on grain size. As grain size decreases, the critical twinning stress increases, making deformation twinning more difficult. Their TEM observations in Fe–22Mn–0.6C TWIP steel showed that the fraction of twinned area increased with increasing grain size, while fine-grained

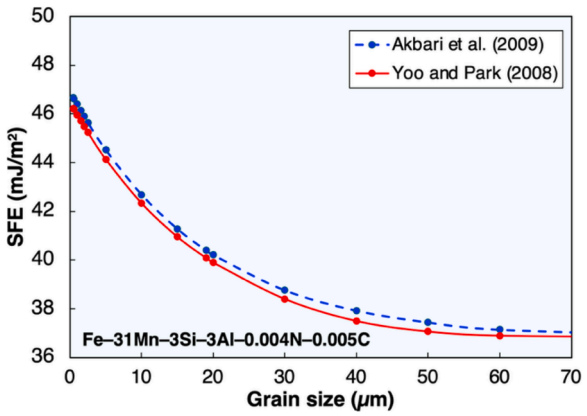


Fig. 20. Calculated SFE as a function of grain size for Fe–31Mn–3Si–3Al–0.004 N–0.005C (alloy studied by Bai et al. [8]) using Saeed-Akbari et al. [138] and Yoo and Park [122] thermodynamic models.

specimens exhibited fewer deformation twins. This effect is crucial for HE because grain refinement can also modify the formation and distribution of deformation twins, including twin–twin and twin–grain boundary intersections, which may act as local stress concentrators and hydrogen-assisted crack-initiation sites.

Zan et al. [132] showed that in Fe–22Mn–0.6C TWIP steel, HE susceptibility increases with increasing the grain size. The elongation loss caused by hydrogen increased strongly as the grain size increased from fine to coarse conditions. This was attributed to two linked factors: coarser grains contained more hydrogen per unit grain-boundary area and also promoted earlier and more extensive deformation twinning. The larger density of deformation twins and twin-related intersections in coarse grains generated more stress-concentration sites, providing favorable paths for hydrogen-assisted cracking. Therefore, this work shows [132] that grain refinement improves HE resistance not simply by trapping hydrogen, but also by delaying deformation twinning and reducing the number of twin-related crack-initiation sites. Park et al. [133] reached a similar conclusion in a Fe–18Mn–0.6C TWIP steel. However, the beneficial effect of grain refinement is not universal. Moallemi et al. [95] reported the opposite behavior in a metastable high-Mn austenitic steel, where reducing the grain size from the coarse-grained to fine-grained condition increased HE susceptibility. In that case, relative elongation loss increased markedly after grain refinement, and the dominant damage mode remained intergranular. This adverse effect was attributed to the combined influence of higher flow stress, larger normal stress on grain-boundary planes, and sufficient hydrogen accumulation at grain boundaries to activate decohesion. Although refinement increased austenite stability and suppressed ε-martensite formation, the local hydrogen concentration per grain-boundary area remained high enough to weaken boundaries. Consequently, the protective effect of refinement was overwhelmed by hydrogen-assisted intergranular cracking.

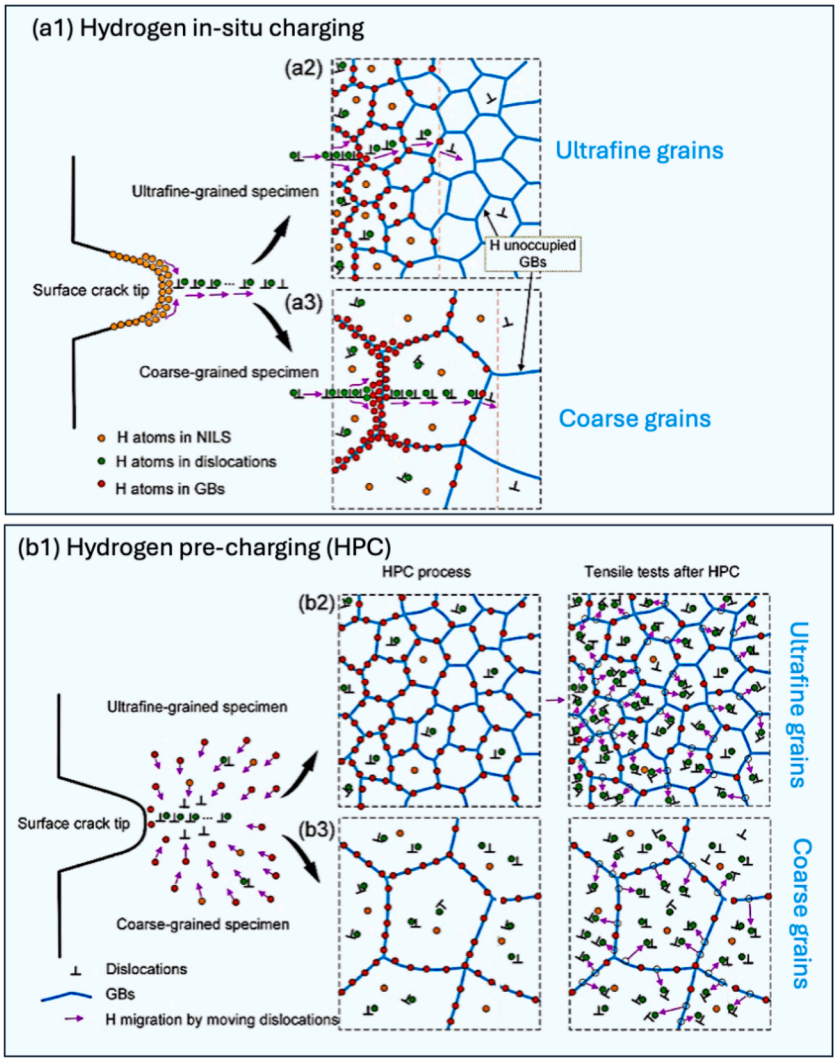


Fig. 21. Schematic presentation of the effect of grain refinement on hydrogen uptake, diffusion and distribution in two different charging conditions: (a) in-situ electrochemical charging and (b) ex-situ electrochemical pre-charging for 96 h. Both conditions use an electrolyte of 0.5 mol/L H_2SO_4 and a charging current density of 50 mA/cm^2. Orange dashed lines in (a2) and (a3) highlight the hydrogen-affected region. Abbreviations: NILS: normal interstitial lattice sites, GB: grain boundary, HPC: hydrogen pre-charging. Modified and reproduced from Wang et al. [136].

The comparison between the results of Bai et al. [8] and Moallemi et al. [95] indicates that the key factor is not grain size alone, but the combined ratio of absorbed hydrogen, total boundary area, boundary character, local stress, and effective SFE are similarly important. Wang et al. [136] further clarified this by studying grain refinement in 304 ASS under two different hydrogen-charging routes: hydrogen pre-charging and hydrogen in-situ charging. Their results show that the effect of grain refinement depends strongly on how hydrogen is introduced. Under in-situ charging, grain refinement reduced HE susceptibility because the increased number of grain boundaries lowered the apparent hydrogen diffusivity and reduced the amount of hydrogen at each grain boundary. Under pre-charging, however, ultrafine-grained specimens became more susceptible because the long charging time allowed a large amount of hydrogen to fill the numerous grain boundary traps. In that condition, grain boundaries acted not only as traps but also as hydrogen reservoirs, supplying hydrogen to stress-concentrated lattice sites and newly formed dislocations during deformation.

This finding is schematically summarized in Fig. 21. The schematic illustrates why the same increase in grain boundary area can be either beneficial or harmful. In coarse grains, fewer boundaries mean that the hydrogen concentration at each boundary can become high, favoring decohesion. In fine grains under appropriate conditions, hydrogen is distributed over a larger boundary area, reducing hydrogen occupancy per boundary and suppressing intergranular fracture. However, if the charging condition allows excessive hydrogen uptake, as in long-term pre-charging, fine grains can store a larger total amount of hydrogen and maintain high boundary occupancy. In that case, grain refinement may increase HE rather than suppress it. Thus, Fig. 21 supports the view that hydrogen occupancy per trap, rather than the absolute number of traps, is the controlling factor.

Therefore, based on the studies summarized in Table 5, the effect of grain refinement on HE in FCC steels should be interpreted through four coupled mechanisms: hydrogen redistribution and trap occupancy, effective SFE and phase stability, grain boundary character, and grain size-dependent deformation mechanisms. These factors are strongly interconnected and cannot be considered independently. For example, a refined grain structure may raise SFE and suppress martensitic transformation, but it may also increase grain-boundary area available for hydrogen trapping. Similarly, grain refinement may delay deformation twinning by increasing the critical twinning stress, while simultaneously increasing the flow stress, and, consequently, the normal stresses acting on grain boundary planes. Whether grain refinement ultimately improves HE resistance or enhances embrittlement is therefore controlled by the dominant mechanism operating under a given combination of alloy chemistry, hydrogen distribution, and deformation mechanism.

From an HEP perspective, grain size should therefore be considered as a microstructural tuning parameter rather than a universally beneficial strategy. Grain refinement is most likely to support HEP when it increases austenite stability, optimizes the critical stress for twinning, distributes hydrogen over a large population of special boundaries, and maintains low local hydrogen occupancy. Conversely, grain refinement may become detrimental when hydrogen occupancy at boundaries remains high, when random high-angle boundaries dominate, or when increased flow stress raises the driving force for intergranular decohesion. In this sense, grain refinement must be optimized together with SFE, hydrogen charging condition, boundary character, and deformation mechanism.

5.2. *Effect of second phase:* k-*carbide and B2 precipitation*

5.2.1. *k-carbide*

Precipitation represents one of the most important, but also one of the most microstructure-sensitive, factors controlling hydrogen-steel interactions. In general, carbides, nitrides, and intermetallic phases may reduce the amount of mobile hydrogen by acting as segregation sites. However, the same precipitates can also create preferred sites for hydrogen accumulation, interfacial decohesion, or strain localization when they are coarse, incoherent, or located at grain boundaries. Therefore, the role of precipitation should, similarly to other microstructural features, not be described simply as beneficial or detrimental. Instead, it depends on the chemistry, interface coherency, local stress state, and spatial distribution of the precipitates.

In the HEP framework, this is particularly important because precipitation may influence solid-solution hardening, work-hardening, deformation stability, dislocation activity, microband formation, and, potentially, the conditions under which hydrogen contributes to enhanced plasticity or enhanced damage. There is no direct evidence for precipitation-assisted HEP yet; but in Fe–Mn–Al–C alloy systems, κ-carbide could provide a useful case study because it can act either as a non-threatening hydrogen sink or as a critical damage-initiation site, depending on its morphology, size and location.

κ-Carbide is generally described as an ordered, FCC-derived $E2_1/L1_2$-type carbide with the nominal composition $(Fe,Mn)_3AlC_x$, where x is often below unity because of C off-stoichiometry [142]. The ideal structure contains Al at the corner sites, Fe/Mn at the face-centered sites, and C at the octahedral body-centered interstitial site. Experimental and APT studies show that κ-carbides usually precipitate coherently within the austenitic matrix during optimized aging, often after spinodal decomposition and ordering reactions that produce C- and Al-enriched regions before the formation or coarsening of the carbide phase [142–144]. This precipitation pathway is important for hydrogen trapping because the C-deficient nature of the κ-carbide introduces vacant C sites, and such sites are energetically favorable positions for hydrogen.

A DFT study [145] has shown that hydrogen tends to occupy positions associated with vacant C sites in κ-carbides and that the κ-carbide/austenite interface is a particularly attractive trapping region. The calculated trapping tendency is enhanced by local chemical environments, including Mn-related short-range interactions, and by the lattice expansion associated with interstitial occupation. These results explain why finely dispersed κ-carbides can reduce the fraction of diffusible hydrogen in the austenitic matrix and delay hydrogen transport toward more dangerous sites such as grain boundaries, triple junctions, and crack tips. In this sense, coherent intragranular κ-carbides can function as beneficial traps when they immobilize hydrogen without introducing a severe local stress concentration or a weak decohesive interface. Xiong et al. [104] demonstrated that in a Fe–30Mn–8Al–1.2C steel aged at 600 °C, a short aging treatment produced globular κ-carbides with a size of approximately 2–4 nm, which increased the YS while maintaining a

ductile-dominated fracture mode and reducing HE sensitivity. Thermal desorption analysis suggested a higher amount of reversibly trapped hydrogen in this condition, suggesting that the large interfacial area of fine κ-carbides captured hydrogen and limited its detrimental redistribution. This observation agrees well with the DFT prediction that κ-carbide interfaces and C vacancies are effective hydrogen traps [145,146]. Thus, when κ-carbides remain fine and coherent, their high number density and large total interface area can distribute hydrogen over many moderate traps, reducing hydrogen availability at grain boundaries and triple junctions.

In contrast, κ-carbides become detrimental when aging promotes their coarsening, grain boundary precipitation, or loss of effective shearability. Several studies show that grain boundary κ-carbides are more detrimental than intragranular κ-carbides because they combine three harmful features: preferential hydrogen trapping, mechanical incompatibility with the surrounding austenite, and direct connection to intergranular crack paths. Koyama et al. [105] reported that hydrogen charging reduced the tensile elongation of a precipitation-hardened Fe–26Mn–11Al–1.2C austenitic steel from 44% to 5%, with damage dominated by grain boundary triple

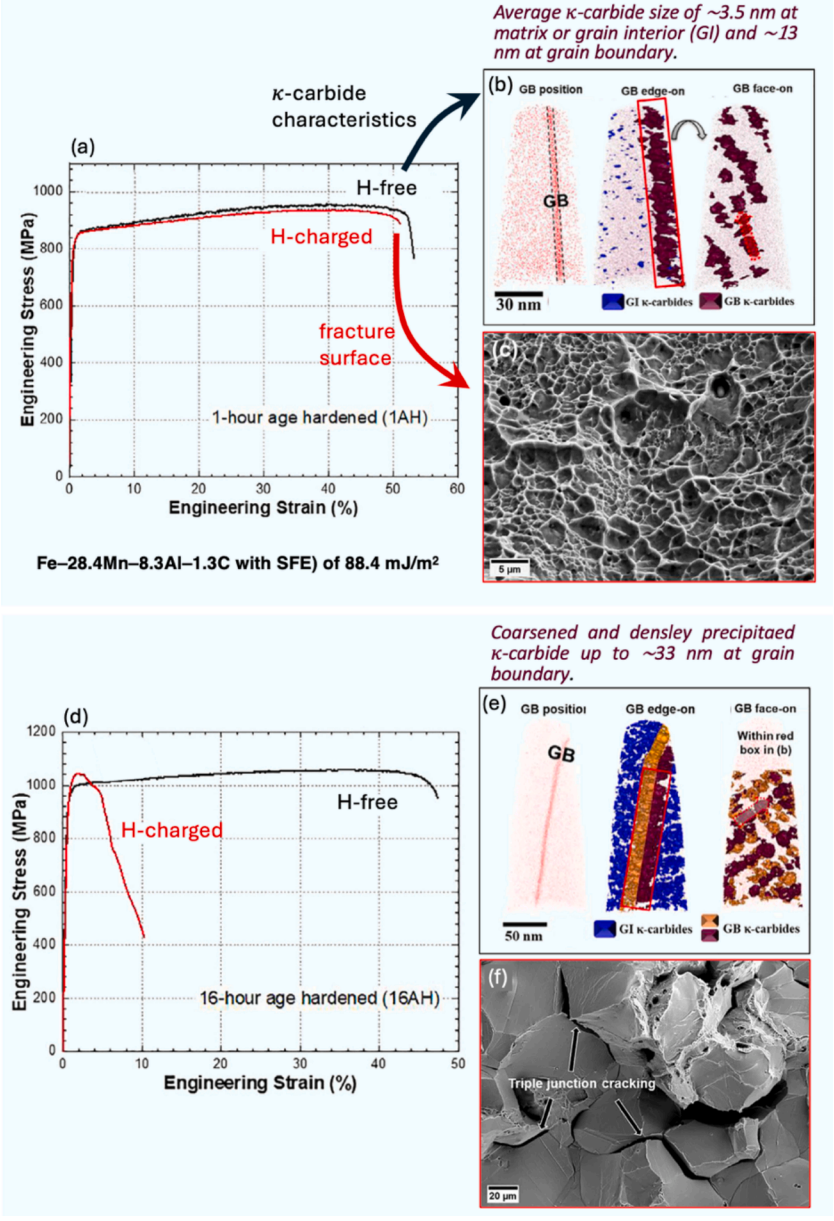


Fig. 22. (a,d) Engineering stress–strain curves of H-free and H-charged 1 h aged (1AH) and 16 h aged (16AH) samples, respectively. (b,e) APT reconstructions of H-free 1AH and 16AH samples showing κ-carbides identified using a 9 at.% C iso concentration criterion from GB edge-on and face-on views. GI κ-carbides are shown in blue; GB κ-carbides are shown in dark red for 1AH and in orange/dark red for the left- and right-hand grains in 16AH, and (c,f) Fracture surfaces of H-charged 1AH and 16AH samples, showing predominantly ductile fracture in 1AH and brittle fracture near the charging surface in 16AH. Abbreviations: GI: grain interior (bulk) and GB: grain boundary. Adapted from Elkot et al. [91].

junction cracking and slip-localization-assisted intergranular fracture. Although this work emphasized strain localization and microband activity, later studies clarified that the precipitation state of κ −carbides at grain boundaries is a key factor in activating interfacial decohesion.

As presented in Fig. 22, Elkot et al. [91] provided direct experimental evidence for hydrogen-assisted decohesion associated with coarse grain boundary κ-carbides in a Fe–28.4Mn–8.3Al–1.3C steel. APT and STEM examinations revealed that κ-carbides can precipitate at grain boundaries even at relatively early aging stages, not only after classical overaging (Fig. 22**b**). With increasing aging time, the average grain boundary κ-carbide size increased from about 13 nm to about 32 nm (Fig. 22**b** vs Fig. 22**e**), while the C content and elastic misfit also increased. Under comparable hydrogen charging conditions, the solution-treated and briefly aged specimens (1 h showed intergranular fracture zones with depths of about 20 μm, whereas the more strongly aged condition (16 h) exhibited intergranular fracture extending beyond 550 μm and a 77% reduction in total elongation (Fig. 22**d**). Importantly, cracks in the aged condition did not simply follow ordinary grain boundaries; they preferentially propagated along the κ-carbide/austenite interfaces. This indicates that hydrogen trapped at these interfaces lowers the local cohesive strength and promotes HEDE at a lower critical hydrogen concentration than that required for decohesion of a clean γ/γ grain boundary and triple junctions (Fig. 22**f**).

Coarse or non-shearable grain boundary κ-carbides obstruct dislocation motion and promote dislocation pile-ups. These pile-ups increase hydrostatic and interfacial stresses, which in turn drive additional hydrogen toward the κ-carbide/matrix interface. Hydrogen then reduces the work of separation and lowers the resistance to interfacial cleavage. Xiong et al. [104] further confirmed this size sensitivity of κ-carbide. Prolonged aging generated coarser grain boundary κ-carbides, in some cases above 100 nm, together with dense microbands and stress concentration at grain boundaries, leading to a much larger brittle region and a high HEI.

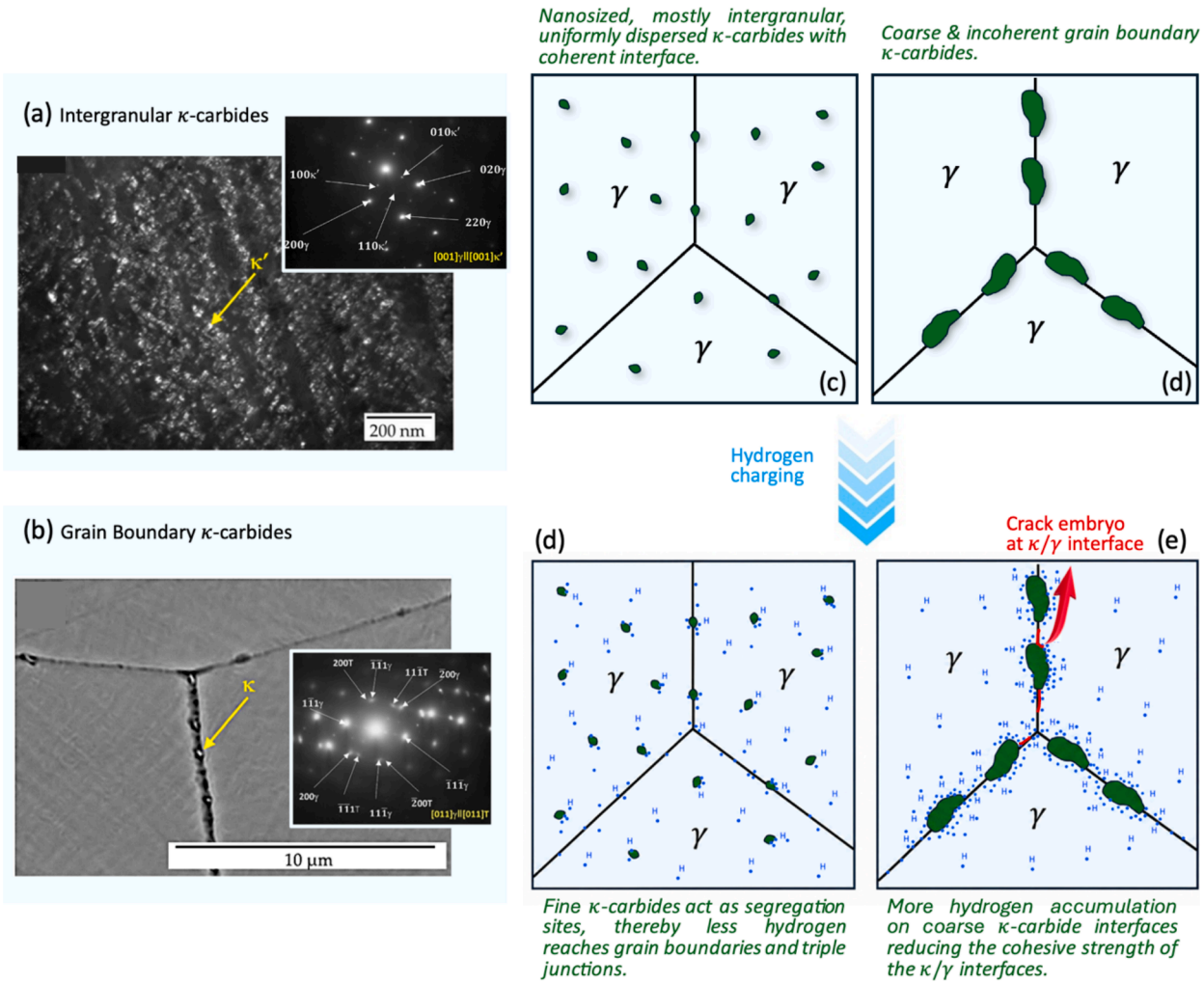


Fig. 23. Schematic illustration of the dual role of κ-carbides in hydrogen partitioning, together with STEM micrographs of (a) intergranular and (b) grain boundary κ-carbides in a Fe–29Mn–9Al–0.85C aged at 550 °C. (c) Fine, coherent intragranular κ-carbides distribute hydrogen among numerous benign traps and reduce its accumulation at grain boundaries and triple junctions, whereas (d) coarse grain-boundary κ-carbides concentrate hydrogen at κ-carbide/austenite interfaces and promote interfacial decohesion. STEM micrographs from Witkowska et al. [148].

As schematically shown in Fig. 23, the role of κ-carbides should therefore be interpreted as location- and size-dependent. Intragranular, coherent κ-carbides with sizes of only a few nanometers trap hydrogen in a distributed manner and may reduce the hydrogen flux toward high-risk defects. In contrast, coarse, incoherent, or grain-boundary κ-carbides concentrate hydrogen at mechanically weak interfaces and provide preferred crack-initiation and crack-propagation paths. This distinction also reconciles apparently contradictory reports on C-containing Fe-Al or Fe-Mn-Al-C systems. Early observations on Fe_3Al-Fe_3AlC intermetallic alloys showed that moderate C additions could improve HE resistance, whereas very low or excessive C contents promoted cracking either in the Fe_3Al phase or in interdendritic/carbide regions [147].

From an alloy-design and processing perspective, κ-carbide should be controlled to maximize fine intragranular morphology over coarse grain boundary precipitation. This requires careful optimization of Al, C, Mn, and additional alloying elements, together with heat-treatment schedules that promote a uniform nanoscale dispersion without allowing continuous grain boundary decoration. Recent reviews emphasize that Al and C promote κ-carbide precipitation, whereas Mn tends to suppress it, and that aging in the approximate range of 500–700 °C can promote intragranular precipitation when the composition and prior processing are properly selected [144]. Si can also accelerate κ-carbide precipitation by increasing the C activity in austenite, while also influencing C partitioning and vacancy ordering in κ-carbide [143]. These effects may be useful for strengthening but must be balanced against the risk of accelerated coarsening or grain boundary precipitation. Grain-boundary engineering may also be beneficial, for example by increasing the fraction of special low-energy boundaries such as coherent Σ3 twin boundaries, which are less favorable sites for continuous carbide precipitation and intergranular decohesion.

5.2.2. B2 precipitates

In addition to κ-carbides, high Al contents in Fe–Mn–Al–C steels, generally above approximately 7–8 wt%, can promote the formation of ordered B2 intermetallic phases. These phases are BCC-derived FeAl- or NiAl-type compounds with CsCl-type ordering, which distinguishes them from disordered ferrite/BCC (A2). In Ni-bearing alloys, Ni addition stabilizes NiAl-type B2 relative to Ni-free FeAl-type B2, because replacing Fe with Ni at a fixed Al content makes the enthalpy of formation of B2-(Fe,Ni)Al increasingly negative [149,150]. Therefore, B2 precipitation in lightweight Fe–Mn–Al–C steels is strongly controlled by Al content, Ni addition, and the balance between ordered intermetallic formation and austenite stabilization.

The mechanical role of B2 precipitates differs from that of κ-carbides. While fine κ-carbides can often be sheared by dislocations, B2 precipitates, particularly when they become coarse or highly ordered, generally behave as hard and less-shearable obstacles [151]. Dislocation pile-up at B2/austenite interfaces produces strain incompatibility between the relatively soft austenitic matrix and the hard intermetallic phase [152]. This can generate back stresses and enhance work-hardening, so a moderate fraction of finely dispersed intragranular B2 precipitates may improve the strength–ductility balance [151,152]. However, excessive B2 precipitation, coarse particles, or continuous B2 networks along grain boundaries can promote strain localization and brittle fracture. Large or boundary-connected B2 phases therefore act as potential crack-initiation sites under tensile stress [153]. From an alloy-design perspective, the key requirement is not simply to avoid B2 precipitation, but to control its fraction, size, coherency, and spatial distribution.

The influence of B2 precipitates on hydrogen-assisted damage is more complex and less systematically documented than that of κ-carbides. In Fe–Mn–Al–C alloys, hydrogen can interact with several microstructural features, including κ-carbides, B2/DO_3 ordered phases, dislocations, and interfaces, and these interactions may either trap hydrogen or promote embrittlement depending on trap strength and local stress state [105,145,147]. FeAl-type B2 and Fe_3Al-type DO_3 phases are not generally considered hydride-forming phases; however, first-principles studies indicate that hydrogen can occupy interstitial or defect-associated sites in FeAl and weaken the metallic bonding [154,155]. Hydrogen was predicted to cause local lattice dilation and reduce Fe–Al cohesive strength by depleting Fe d-electron bonding [154]. Such effects are expected to be most severe in Fe-rich local environments [154,155]. In steels, however, the more relevant consequence is likely not bulk degradation of the ordered phase itself, but hydrogen-assisted decohesion at ordered-phase/matrix interfaces or at grain boundaries decorated by brittle Fe–Al intermetallics.

The location of B2/DO_3 precipitates is therefore critical. In Ni-free or low-C Fe–Mn–Al–C alloys, where κ-carbide precipitation is limited, hydrogen-related cracking may become concentrated at Fe–Al ordered phases or their interfaces. Rao et al. reported that HE in Fe_3Al/Fe_3AlC-type intermetallic systems was associated with the ordered DO_3 phase, whereas in the high-C counterpart the damage was linked to interdendritic κ-carbide networks [147]. This suggests that when strong or abundant carbide traps are absent, brittle Fe–Al ordered phases, especially if located along grain boundaries, can become preferential sites for hydrogen-assisted intergranular fracture. Thus, grain-boundary B2/DO_3 precipitation is generally undesirable for hydrogen-resistant alloy design because it combines chemical susceptibility, elastic/plastic incompatibility, and interfacial crack sensitivity.

In Ni-bearing alloys, the situation may be different. NiAl-type B2 is generally more stable than FeAl-type B2, and Ni–Al bonding may make it intrinsically less susceptible to hydrogen-induced cohesive weakening than Fe-rich FeAl-type ordered phases. Nevertheless, this does not automatically mean that coherent NiAl precipitates are beneficial hydrogen traps. As coherent NiAl precipitates often have relatively low defect density, they may provide only weak trapping sites, allowing hydrogen to remain mobile and redistribute toward more damaging locations such as precipitate/matrix interfaces, inclusions, grain boundaries, or slip-localized regions. Studies on NiAl-strengthened PH13-8Mo stainless steel indicate that coherent NiAl precipitates do not necessarily behave as strong irreversible traps. Instead, they may increase HE susceptibility by promoting planar slip and hydrogen localization rather than by safely immobilizing hydrogen [156,157].

A further concern is the deformation heterogeneity introduced by hard B2 particles. Under applied stress, non-shearable or weakly shearable precipitates can promote localized slip channels between particles. These regions contain high dislocation densities and can attract hydrogen, forming hydrogen-enriched dislocation structures and Cottrell atmospheres. Koyama et al. [105] showed that in precipitation-hardened Fe–26Mn–11Al–1.2C steel containing κ-carbides, hydrogen-assisted failure was governed by grain-boundary

triple-junction cracking and slip-localization-induced intergranular cracking, where microvoids and cracks formed along boundaries adjacent to intensely localized slip bands [105]. Although direct evidence for the same mechanism in B2-containing Fe–Mn–Al–C steels remain limited, hard B2 precipitates are expected to produce similar or even stronger deformation partitioning because of their lower shearability. Consequently, hydrogen may accumulate near B2/austenite interfaces and at nearby grain boundaries where dislocations pile up, increasing the probability of crack nucleation.

Vacancy-related trapping provides another possible hydrogen interaction pathway in FeAl-type B2 phases. FeAl, which has a lower ordering tendency than NiAl, is predicted to form vacancies and divacancies. Fe vacancies provide a favorable segregation site, calculated by Jasen et al. [158] to be 0.46 eV more stable than interstitial sites in the ideal B2 structure. Binding energies for mono- and divacancies from DFT calculations are as high as 2.32 and 3.05 eV [159]. Zhang et al. [160] extended the study of H in divacancies along $< 100 >$ directions in FeAl to adsorption at stacking faults on {100} planes. They predicted an accumulation of hydrogen, leading to the formation of molecules and even blisters. With this investigation, they bridged the electronic structure analysis of Fu and Wang [159] to a possible mechanism of crack initiation, and the results suggest that FeAl precipitates play at best an ambiguous role in the steel microstructure when it comes to hydrogen trapping.

Yoo et al. [161] investigated the effect of B2 precipitates on HE resistance in high-strength Fe–Mn–Al–C steels. Cu-rich B2 precipitates have been shown to markedly improve HE resistance in duplex lightweight steels. Their semi-coherent interfaces with austenite introduce misfit dislocations which serve as strong irreversible hydrogen traps. Because of their high detrapping activation energy ($E_t \approx 132$ kJ/mol), substantially greater than that reported for many carbide-based traps such as NbC, TiC, Cr-carbides, these B2 particles effectively immobilize hydrogen and reduce the concentration of diffusible hydrogen available for transport through the matrix.

6. Experimental protocol variation

This section examines the potentially critical influence of the possible critical influence of the test protocol on hydrogen interaction with FCC steels. This is particularly important for austenitic steels and FCC alloys because their relatively low hydrogen diffusivity and high hydrogen solubility make the measured response highly sensitive to how hydrogen is introduced, retained, and redistributed during deformation. Therefore, mechanical behavior measured after hydrogen pre-charging may not always be directly compared with that obtained during in-situ hydrogen exposure. Similarly, electrochemical and gaseous charging may affect hydrogen concentration, through-thickness hydrogen distribution, surface condition, and failure after charging.

At present, no systematic study has yet isolated the effect of different charging protocols on HEP mechanisms. However, there are a few available protocol-comparison studies on HE responses [162–166]. Nevertheless, these works are highly relevant to the present review because they demonstrate that the apparent balance between hydrogen-assisted enhancement and hydrogen-assisted degradation can be shifted by the charging method itself. In other words, the same nominal alloy may appear resistant, embrittled, or even mechanically enhanced depending on whether hydrogen is introduced by gaseous pre-charging, electrochemical pre-charging, or continuous in-situ charging during deformation.

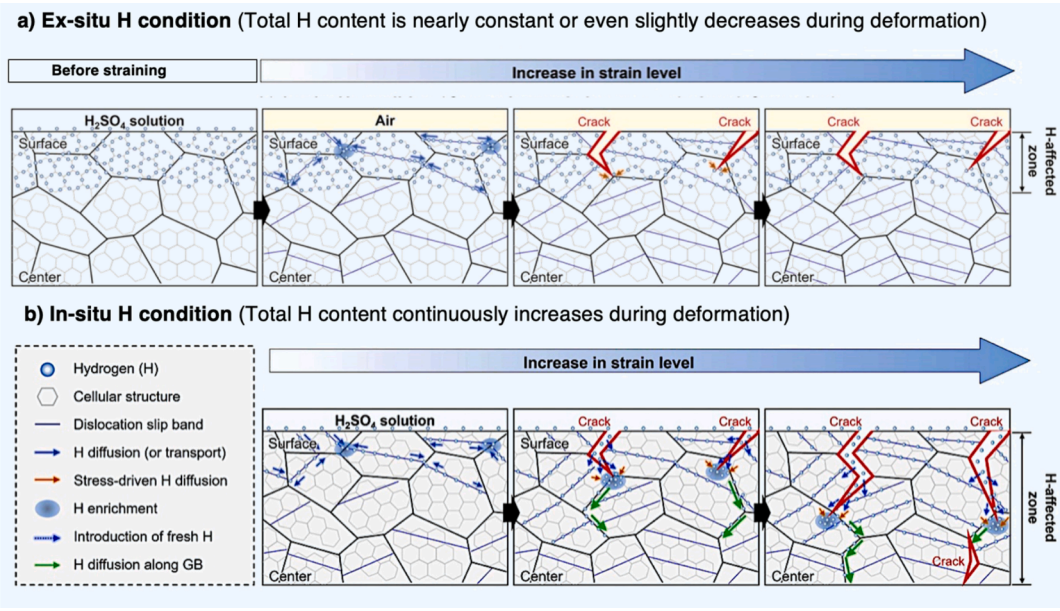


Fig. 24. Schematic comparison of hydrogen permeation and diffusion during straining under (a) ex-situ and (b) in-situ hydrogen charging conditions. Modified from Lee et al. [162].

6.1. In-situ and ex-situ charging

In the context of investigating the impact of hydrogen on the mechanical performance, the first important distinction is between ex-situ and in-situ charging. In ex-situ testing, hydrogen is introduced before mechanical loading, and the specimen is subsequently tested in air or an inert environment. In in-situ testing, hydrogen is supplied continuously during deformation, either by gaseous hydrogen exposure or electrochemical charging. These two conditions are not equivalent. Ex-situ charging mostly probes the effect of pre-existing internal hydrogen, whereas in-situ testing captures the coupled dynamic action of hydrogen under stress, plastic deformation, and evolving microstructural traps. During in-situ charging (with no prior charging), hydrogen is continuously supplied while the microstructure is evolving. Dislocation multiplication, strain localization, grain-boundary sliding, twin formation, and crack-tip stress fields can all create new trapping sites during deformation. Hydrogen can therefore accumulate preferentially at stress concentrators, grain boundaries, dislocation pile-ups, crack tips, and twin or phase interfaces, as schematically presented in Fig. 24. This dynamic coupling often produces a more severe response than ex-situ testing, even when the total measured hydrogen content is not obviously higher. The following examples illustrate this difference.

The influence of in-situ versus ex-situ charging on the HE response of an FCC high-entropy alloy was investigated by Lee et al. [162]. A clear contrast was observed between ex-situ pre-charging and in-situ charging during deformation. As shown in Fig. 25, ex-situ charged samples exhibited only a marginal reduction in ductility and retained their high resistance to HE, whereas in-situ charging caused a severe loss in ductility, reduced work-hardening capacity, and extensive hydrogen-assisted cracking. Hydrostatic tension during straining expands the lattice volume, thereby accommodating more hydrogen, particularly near hydrogen-assisted crack tips. In the absence of applied stress during ex-situ charging, solubility was lower, and hydrogen concentration either remained constant or decreased slightly because of outgassing during subsequent testing.

A similar conclusion was reached in notch tensile testing of ASSs under in-situ and ex-situ electrochemical charging. Shin et al. [167] investigated notch tensile properties of 304 L and 316 L ASSs under in-situ and ex-situ electrochemical hydrogen charging environments. Their results also demonstrated that in-situ charging, which provides a continuous hydrogen supply during deformation, caused significant ductility loss and accelerated brittle fracture at notch tips, whereas ex-situ pre-charging produced only minimal embrittlement. This highlights the critical importance of localized hydrogen accumulation during loading, rather than the total absorbed hydrogen content, in governing HE susceptibility.

The distribution of hydrogen during deformation also differs significantly between the two methods, both in spatial profile and interaction with microstructural features, Fig. 25. In pre-charged specimens, hydrogen may partly desorb before or during testing, unless special procedures such as low-temperature storage or surface coating are used [136]. Zinc electroplating has been used in some studies to reduce hydrogen outgassing during SSRT testing and to better preserve the initially introduced hydrogen content [168]. In in-situ tests, however, hydrogen is continuously generated or supplied and can be transported toward newly formed traps. Therefore, in-situ conditions are often more representative of service environments where mechanical stress and hydrogen exposure occur simultaneously. For the present work, this distinction has an important implication: a condition that appears to promote HEP in an ex-situ test may not necessarily remain beneficial under in-situ exposure. If the hydrogen supply during loading becomes excessive or highly localized, the same mechanisms that can enhance work-hardening, such as planar slip, twinning, or microbanding, may instead promote crack initiation [136].

6.2. Electrochemical and gaseous charging

Hydrogen charging methods usually include electrochemical and gaseous charging. Both are widely employed to evaluate hydrogen interactions with austenitic steels. Although both approaches successfully introduce hydrogen into the material, they differ significantly in terms of hydrogen uptake and distribution. Electrochemical charging is usually performed at or near room temperature

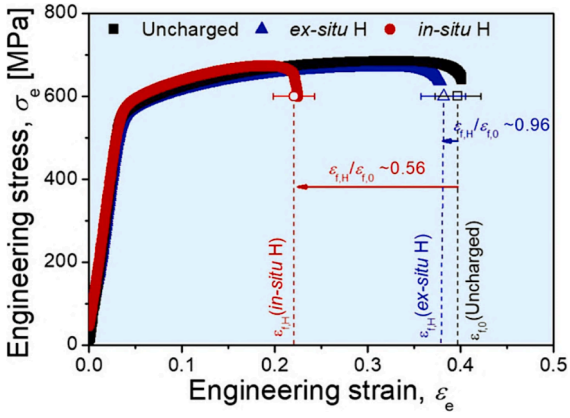


Fig. 25. Engineering stress–strain tensile curves of a Co–Cr–Fe–Ni FCC alloy obtained from uncharged, ex-situ H-charged, and in-situ H-charged samples [162].

in an electrolyte, often with recombination poisons such as thiourea or NH_4SCN. This method can introduce high near-surface hydrogen concentrations, especially when high current densities (e.g., 100 A/m^2) are used. However, because hydrogen diffusivity in FCC alloys is low at room temperature, electrochemical charging often produces a steep hydrogen concentration gradient, with hydrogen concentrated mainly near the surface. As a result, the surface layer may be strongly affected by hydrogen, while the specimen bulk may remain relatively H-free. This can either exaggerate surface cracking or, in conventional tensile geometries, mask the true hydrogen effect because the H-free bulk dominates the macroscopic load-bearing response.

Gaseous charging is typically performed at elevated temperatures (approximately 300 °C) and high hydrogen pressure (approximately 100 MPa). Although the maximum hydrogen content may be limited by thermodynamic solubility under the selected pressure and temperature, gaseous charging can produce a much more uniform hydrogen distribution through the specimen thickness. This is particularly important for FCC alloys, where long diffusion times are required at room temperature. Therefore, gaseous charging is often better suited for studying the effect of dissolved, relatively homogeneous solute hydrogen on bulk tensile behavior, whereas electrochemical charging is particularly sensitive to surface hydrogen gradients and near-surface damage. Several representative studies are discussed below.

Yun et al. [164] studied the effect of hydrogen pre-charging methods, electrochemical versus gaseous, on the HE behavior of a 304 L ASS. Both methods led to ductility loss and changes in fracture mode, but the hydrogen distribution differed markedly. Electrochemical charging produced non-uniform penetration through the sample thickness, with hydrogen mainly segregated at grain boundaries (near-surface regions), while gaseous charging generated a more uniform distribution. These differences influenced the work-hardening response and fracture morphology. Electrochemical charging resulted in mixed brittle–ductile fracture surfaces with localized surface cracking, whereas gaseous charging consistently produced brittle features such as quasi-cleavage and secondary cracks.

Lee et al. [163] investigated the HE susceptibility of austenitic high-manganese steels using different hydrogen charging methods, including ex-situ electrochemical charging, ex-situ high pressure thermal gaseous charging, and in-situ high pressure gaseous charging. As demonstrated in Fig. 26, each method resulted in a different degree of embrittlement. The in-situ gaseous method consistently produced the most severe embrittlement, exhibiting intergranular brittle fracture surfaces. This increased susceptibility was attributed to the simultaneous action of plastic deformation and hydrogen charging under high triaxial stress, which promoted hydrogen uptake and crack propagation along austenite grain boundaries. Ex-situ electrochemical and gaseous charging resulted in shallower hydrogen penetration and less severe ductility loss. Electrochemical charging introduced hydrogen non-uniformly, with hydrogen trapped mainly at grain boundaries, whereas high-pressure thermal charging produced a deeper hydrogen-affected zone with hydrogen more evenly distributed in the lattice, reflecting the role of elevated temperature and pressure in increasing hydrogen diffusivity. Nevertheless, both ex-situ methods showed ductile fracture morphologies with localized hydrogen effects, in contrast to the widespread intergranular fracture observed under high-pressure gaseous conditions.

Tables 6 and Table 7 summarize the reported cases of hydrogen-assisted embrittlement, minimal degradation, and hydrogen-assisted enhancement under electrochemical charging and gaseous charging, respectively. Here, HE is defined as more than 20% elongation loss, while minimal degradation corresponds to less than 20% elongation loss. The available evidence suggests that the most convincing examples of hydrogen-assisted enhancement are mainly associated with gaseous pre-charging or other conditions that introduce relatively homogeneous dissolved hydrogen. Regarding Table 6, attention should also be paid to the applied current density as one of the important parameters controlling hydrogen entry. Higher current density generally increases the hydrogen generation rate at the specimen surface and raises the measured hydrogen content. However, in FCC alloys this does not necessarily produce a uniform hydrogen distribution through the specimen thickness. Because room-temperature hydrogen diffusivity is low, higher current density often increases the surface hydrogen concentration more strongly than it affects the penetration depth. The same applies to the charging duration. For example, in the U-grooved specimen study discussed in **Section 3**, doubling the charging time from 72 to 144 h

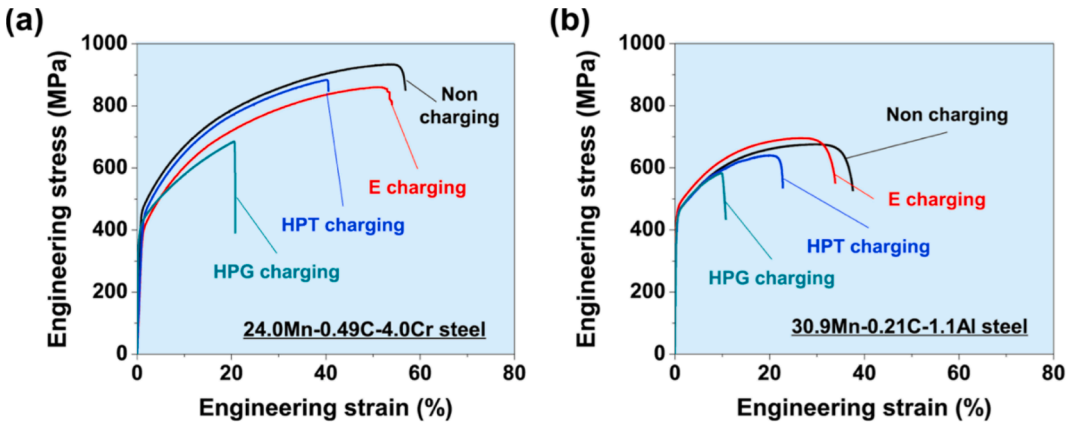


Fig. 26. Engineering stress–strain curves of two austenitic high-Mn steels tested under different hydrogen charging conditions: (a) 24.0Mn–0.49C–4.0Cr steel and (b) 30.9Mn–0.21C–1.1Al steel. Abbreviations: E: ex-situ electrochemical charging, HPT: ex-situ high-pressure thermal charging, and HPG: in-situ high-pressure gaseous charging [163].

Table 6
Representative studies showing hydrogen-affected mechanical properties of different FCC steels under electrochemical hydrogen charging. Additional details on hydrogen content, strain rate, and sample dimension are provided in Supplementary Table S3.6.

Alloy System	Material Composition	SFE, mJ/m^b	Electrochemical Solution	Charging Parameters****	H Content, w.ppm	Response ***	References
Alloyed High Mn Steels (No Al)	Fe–24Mn–4Cr–0.49C	24	0.4% NaOH	50 A/m^b, 48 h	–	↔	[163]
	Fe–(6,12, 18) Mn–6Ni–14.5Cr–0.06C	21–37	0.2 M NaOH + 3% NaCl + 0.3% NH4SCN	*20 A/m^b, 24 h, 90 °C	4–7	↔	[168]
	Fe–24Mn–3.1Cr–0.35C	–	3% NaCl + 0.3% NH4SCN	50 A/m^b, 48 h, 94 °C	21–25	↓	[93]
	Fe–15Cr–11Mn–6Ni–0.02C –0.3 N	40.1	3% NaCl + 0.3% NH4SCN	50 A/m^b, 48 h, 90 °C	0.73	↓	[102]
Fe-Mn-Al-C Steels	Fe–25Mn–5.5Al–3Si–1C	49.5	0.1 M H2SO4 + 2 g/L NH4SCN	200 A/m^b, 24 h	4.51	↑	[28]
	Fe–30.9Mn–1.1Al–0.21C	32	0.4% NaOH	50 A/m^b, 48 h	–	↔	[163]
	Fe–18Mn–(0,1,2)Al–0.6C	–	3% NaCl + 0.3% NH4SCN	50 A/m^b, 48 h	0.65–2.2	↓	[92]
	Fe–28.4Mn–8.3Al–1.3C **	88.4	3% NaCl + 0.3 wt% NH4SCN	25 A/m^b, 72 h	15	↔	[91]
	Fe–30Mn–8Al–1.2C **	–	0.05 M H2SO4 + 1 g/L CH4N2S	50 A/m^b, 24 h	9.1	↔	[103]
	Fe–31Mn–3Al–3Si–0.005C	< 40	3% NaCl + 3 g/L NH4SCN	100 A/m^b, 48 h	7.1	↔	[8]
	Fe–18Mn–1.5Al–0.6C	25	3% NaCl + 3 g/L NH4SCN	13 A/m^b, 45 h, 40 °C	4.2	↓	[169]
Cr-Ni Stainless Steels	ASS 316 L	–	0.1 M NaOH + 0.5 mol/L H2SO4 + 0.5 g/L thiourea	300 A/m^b, 168 h, 25 °C	–	↔	[135]
	ASS 316 L	–	3% NaCl + 0.3% NH4SCN	50 A/m^b, 48 h	2.72	↔	[101]
TWIP/ TRIP Steels	Fe–22Mn–0.6C	20–40	Glycerol + 600 g Borax + 0.002 M Na2S2O3	100 A/m^b, 80 °C	9.39	↔	[97]
	Fe–18Mn–0.6C-0Si	–	3% NaCl + 0.3% NH4SCN	50 A/m^b, 48 h	4.54	↔	[170]
	Fe–18Mn–0.6C–1.5Si	–	3% NaCl + 0.3% NH4SCN	50 A/m^b, 48 h	4.12	↔	[170]
	Fe–18Mn–0.6C–3Si	> 8	3% NaCl + 0.3% NH4SCN	50 A/m^b, 48 h	3.91	↔	[170]
	Fe – 17Mn–0.8C	21	3% NaCl + 0.3% NH4SCN	10 A/m^b, 24 h, 90 °C	–	↔	[9]
	Fe–12.45Mn–1.15C	35	3% NaOH + 3 g/L NH4SCN	168 A/m^b, 24 h,80 °C	6.7	↔	[171]
	Fe–22Mn–0.6C	19	3% NaCl + 0.3 g/L NH4SCN	50 A/m^b, 48 h	–	↓	[30]
	Fe–22Mn–0.6C	23	3% NaCl + 13 g/L NH4SCN	100 A/m^b, 48 h	0.98	↓	[172]

* Other current densities of 50 A/m^2 and 100 A/m^2 were also used in this work, which resulted in more severe embrittlement but still with minimal embrittlement range. ** Age-hardened. *** N: Neutral or minimal effect: 0 < HEI < 20%, HEP/ enhancement: 0 > HEI, HE/ embrittlement: % 20 < HEI. **** It should be noted that, unless otherwise specified, hydrogen charging was performed at room temperature. Arrows indicate the overall elongation change after H-charging: ↑ improved, ↓ worsened, ↔negligible.

increased the penetration depth only from about 73 to 101 μm. This means that changing electrochemical parameters alone may be insufficient for obtaining a uniformly hydrogen-affected tensile gauge volume in FCC alloys.

Therefore, HEP should not be treated as charging-method-independent material property. The charging route establishes the hydrogen chemical potential, uptake kinetics, depth profile, trap occupancy, and persistence during loading. Consequently, electrochemical, gaseous, pre-charged, and continuously charged conditions can produce different responses even at similar nominal hydrogen contents; conclusions are therefore restricted to the exposure and testing conditions of each study. At the same time, it should be emphasized that no study has yet systematically compared HEP under different charging protocols using the same alloy, specimen

Table 7
Representative studies showing hydrogen-affected mechanical properties of different FCC steels under gaseous charging (mainly pre-charging conditions). Additional details on hydrogen content, strain rate, and sample dimension are provided in Supplementary Table S3.7.

Alloy System	Material Composition	SFE, mJ/m^2	Charging Condition	Charging Parameters	H Content, w. ppm	Response **	References
Alloyed High Mn Steels	Fe–25Mn–10Ni–1.5Cr–0.65C	39	Gaseous	16 MPa, 200 h, 300 °C	13.4	↔	[90]
	Fe–16Mn–10Ni–1.5Cr–0.65C	29.5	Gaseous	16 MPa, 200 h, 300 °C	17.2	↓	[90]
	Fe–29Mn–7Cr–6Si	–	Gaseous	100 MPa, 238 h, 270 °C	27.1	↓	[99]
Fe-Mn-Al-C Steels	Fe–30Mn–6.5Al–0.3C	64 ± 10	Gaseous	10 MPa, 200 h, 270 °C	101	↑	[24]
	Fe–30Mn–0Al–6Si	16	Gaseous	10 MPa, 200 h, 270 °C	9.8	↓	[27]
	Fe–30Mn–2Al–4Si	33	Gaseous	10 MPa, 200 h, 270 °C	11.1	↓	[27]
	Fe–30Mn–3Al–3Si	41	Gaseous	10 MPa, 200 h, 270 °C	14.9	↑	[27]
	Fe–30Mn–6Al–0Si	64	Gaseous	10 MPa, 200 h, 270 °C	31.2	↑	[27]
	Fe–31Mn–9Al–1C	100	Gaseous*	10 MPa, 20 °C, 27 °C	N/A	↓	[89]
Cr-Ni Stainless Steels	ASS 310S	–	Gaseous	100 MPa, 200 h, 270 °C	140	↑	[19]
	ASS 310S	20–40***	Gaseous	100 MPa, 200 h, 270 °C	139	↑	[21]
	ASS 310S	48	Gaseous	11 MPa, 200 h, 270 °C	40	↑	[25]
	ASS 310S	48	Gaseous	0.7 MPa, 200 h, 270 °C	8.4	↑	[25]
TWIP/ TRIP Steels	Fe–23Mn–0.5C	NR	Gaseous	7.3 MPa, 168 h, 150 °C	5.58	↓	[173]

* In-situ gaseous charging, no. prior charging. ** N: Neutral or minimal effect: 0 < HEI < 20%, HEP/ enhancement: 0 > HEI, HE/ embrittlement: % 20 < HEI. *** SFE during dynamic loading, in-situ neutron diffraction under applied stresses of 520–820 MPa. NR: Not reported. Arrows indicate the overall elongation change after H-charging: ↑ improved, ↓ worsened, ↔ negligible.

geometry, hydrogen content, strain rate, and microstructural state. This remains a major gap. Nevertheless, Table 6 and Table 7 together suggest that charging protocol is primarily important experimental variable; it can considerably impact whether hydrogen acts as a beneficial solute, a near-surface modifier, or a crack-promoting species.

7. Opportunities and future research directions

The emerging evidence that hydrogen can act as a beneficial interstitial solute element and improve mechanical performance in certain austenitic steels opens a fundamentally new research space that extends beyond conventional HE mitigation strategies. Rather than treating hydrogen solely as a harmful impurity to be excluded, future efforts should aim to deliberately engineer alloys and microstructures that exploit hydrogen–defect interactions to enhance mechanical performance, while maintaining resistance to catastrophic fracture. This paradigm shift presents several interconnected opportunities for advancing both fundamental understanding and materials design.

A first and critical opportunity lies in systematically mapping hydrogen–microstructure–mechanism relationships. Existing studies demonstrate that hydrogen-enhanced ductilization, twinning, and microbanding occur only within narrow windows of SFE, phase stability, grain size, and hydrogen concentration. However, these windows remain poorly quantified, highly alloy-specific and far from understood. Future research should therefore focus on constructing mechanism maps that correlate hydrogen content, deformation mechanism (slip, twinning, microbanding), and fracture response across a wide compositional space, particularly in Fe–Mn–Al–C and Fe–Cr–Ni systems. Such maps would provide a rational framework for identifying hydrogen-compatible alloy domains rather than relying on isolated case studies.

A second major opportunity concerns the development of advanced in-situ and operando characterization techniques capable of capturing hydrogen–defect interactions during deformation. While post-mortem microscopy and ex-situ diffraction have revealed important trends, they cannot resolve the dynamic coupling between hydrogen transport, local stress evolution, and defect nucleation. Future progress will require increased use of in-situ neutron diffraction, synchrotron X-ray diffraction, environmental TEM, and

correlative microscopy, ideally combined with controlled hydrogen charging during mechanical loading. These approaches are essential to directly observe hydrogen-assisted partial dislocation dissociation, twin embryo stabilization, microband nucleation, and strain localization in real time, phenomena that currently remain inferred rather than directly measured.

From a modeling perspective, there is a clear need for multiscale frameworks that bridge atomistic hydrogen–defect interactions with macroscopic mechanical response. First-principles and molecular dynamics simulations have provided valuable insights into hydrogen effects on SFE, dislocation mobility, and cross-slip, yet their predictions often diverge from experimental observations due to the complex nature of most alloys, particularly those containing aluminum. Future modeling efforts must therefore move beyond idealized binary or ternary systems and incorporate realistic chemical complexity, local compositional fluctuations, and evolving defect structures. Coupling such atomistic insights with crystal plasticity and phase-field models represents a promising route toward predictive descriptions of hydrogen-enhanced plasticity and embrittlement competition.

Beyond mechanism maps and multiscale physical modeling, data-driven approaches may support hypothesis generation and experimental prioritization. The present multi-study dataset, however, is too small and heterogeneous to support a validated predictive alloy-design model because alloy condition, hydrogen charging histories, concentration profile, specimen geometries, and mechanical endpoints are not standardized. Progress will require larger datasets where physics-informed machine learning and active-learning strategies could then be used to identify promising composition–microstructure–exposure–loading windows and select the most informative experiments. Such predictions must be externally validated under controlled, service-relevant conditions and can be used to test and refine, rather than assume, the qualitative response regions proposed in Fig. 18.

A particularly promising research direction lies in alloy design strategies that intentionally leverage hydrogen-enhanced plasticity mechanisms. The reviewed literature suggests that hydrogen-induced solid-solution strengthening, HEDT, and HEMB can be harnessed when martensitic transformation and grain-boundary decohesion are suppressed. Two material families appear especially promising: Fe–Mn–Al–C lightweight steels and stable Fe–Cr–Ni austenitic stainless steels. Representative compositions falling within or near the proposed high-SFE target zone of Fig. 18 include Fe–30Mn–6.5Al–0.3C (SFE $\approx$ 64 mJ/m^2, HEDB/HEMB-dominated enhancement [24]), Fe–25Mn–5.5Al–3Si–1C (SFE $\approx$ 49.5 mJ/m^2, HET/HEDT-dominated enhancement [28]), Fe–30Mn–3Si–3Al and Fe–30Mn–6Al (SFE $\approx$ 41 and 64 mJ/m^2, [27]), and the Fe–24Cr–19Ni family of stable austenitic stainless steels (SFE $\approx$ 40–48 mJ/m^2, HEH-dominated solid-solution strengthening [17,19,21]). In both systems, the SFE can be adjusted through alloying to promote or suppress specific deformation mechanisms. In Fe–Mn–Al–C steels, Mn stabilizes austenite, Al increases stacking fault energy, and C contributes to both austenite stability and precipitation strengthening. In Fe–Cr–Ni stainless steels, Ni stabilizes austenite, while Cr provides corrosion resistance and contributes to hydrogen-service compatibility. Future alloy design should therefore aim to define practical stacking fault energy windows in which hydrogen-assisted planar slip, twinning, or microbanding can enhance work-hardening without activating martensitic transformation, grain boundary decohesion, or severe strain localization. This is particularly important for practical applications such as automotive lightweight structures and hydrogen transport components, where steels may be exposed to in-situ hydrogen during mechanical loading.

A longer-term alloy design opportunity is to develop austenitic steels whose composition and microstructure produce a beneficial response to hydrogen absorbed during sustained service exposure; however, this concept requires validation across realistic hydrogen concentrations, concentration gradients, exposure histories, and loading conditions. An important conceptual broadening of this alloy design perspective is that hydrogen does not necessarily need be introduced during production at all. An alloy system or microstructure that appears suboptimal in the H-free condition could, in principle, be deliberately designed to evolve toward an enhanced strength–ductility state once exposed to a hydrogen-containing service environment. Framed this way, hydrogen-compatible alloy design is not only about excluding or minimizing hydrogen uptake but can also be about engineering a composition and microstructure whose properties evolve favorably as the material approaches a new, hydrogen-influenced equilibrium with its environment. This perspective has established precedents in physical metallurgy, particularly in surface-engineered and environmentally responsive materials whose local composition and properties evolve during processing or service. Examples include deliberately carburized or nitrided surface layers and selective dealloying, where behavior is governed by the evolving local composition rather than solely by the nominal composition established during production. Because the hydrogen concentration relevant to a component can change over time, rapidly in the surrounding environment and, given the comparatively low hydrogen diffusivity of austenite, more slowly within the material itself, the through-thickness or local compositional heterogeneity discussed throughout this review (Sections 3, 5 and 6) should be viewed not only as an experimental confound but also as a potential design opportunity, analogous to deliberately engineered property gradients. Realizing this opportunity will require a much more precise understanding of the different active mechanisms and the critical hydrogen concentration(s) governing the transition between the risk, transition and target zones conceptually presented in Fig. 18, since it is this evolving, spatially and temporally variable hydrogen state, rather than a single nominal bulk content, that will ultimately determine whether a component moves toward an enhanced or a degraded condition over its service life. Realizing this opportunity requires a multidisciplinary research approach spanning several fields of materials science.

Another important aspect concerns the interaction between hydrogen charging conditions and mechanical response. Increasing evidence shows that hydrogen pre-charging (ex-situ) and in-situ charging can lead to fundamentally different deformation and fracture behaviors, even in the same alloy. This highlights the necessity of designing experiments and models that reflect realistic service environments, including cyclic hydrogen exposure (from both an electrochemical and gaseous sources), stress-assisted diffusion, and surface-mediated hydrogen ingress. Consequently, an alloy that exhibits hydrogen-assisted mechanical enhancement under one charging condition may display severe embrittlement under another, despite having a comparable nominal hydrogen content. Understanding how hydrogen distribution, transport kinetics, deformation mechanisms, and microstructural evolution interact under different charging conditions is therefore essential for translating laboratory-scale observations of hydrogen-enhanced ductilization into reliable engineering applications. Addressing this issue requires systematic comparisons using identical alloy compositions,

specimen geometries, microstructures, and strain rates, while varying only the charging protocol. At a minimum, such studies should include: (i) gaseous pre-charging to generate uniform hydrogen, (ii) electrochemical pre-charging to generate near-surface hydrogen gradients, and (iii) in-situ charging using both sources to capture hydrogen ingress during deformation. Only then can the apparent enhancement or degradation be separated from the artifacts of hydrogen distribution and testing geometry.

In addition, translating laboratory observations of HEP to service requires experiments that reproduce the hydrogen chemical potential, pressure, temperature, exposure duration, surface condition, component dimensions, and loading history expected during operation. This is particularly important for austenitic steels, in which low hydrogen diffusivity can produce time-dependent through-thickness concentration gradients, such that laboratory pre-charging may not reproduce the transient or steady-state hydrogen distribution established during long-term service. Future studies should therefore combine long-duration exposure with in-situ testing in high-pressure gaseous hydrogen and characterization of hydrogen uptake, permeation, trapping, and spatial distribution. Any favorable monotonic tensile response must subsequently be evaluated through fracture-toughness, fatigue and fatigue-crack-growth, sustained-load, and multiaxial tests before it can be considered relevant to structural hydrogen service.

Limited evidence from cyclic-loading studies nevertheless indicates that hydrogen may not be also invariably detrimental to fatigue performance. Murakami et al. [174] reported that, in types 304 and 316 L austenitic stainless steels pre-charged with supersaturated internal hydrogen, fatigue-crack growth was retarded and fatigue life increased above a hydrogen-content-dependent threshold, whereas lower hydrogen contents accelerated crack growth. More recently, Zhao et al. [175] reported a dual response during in-situ electrochemical charging of 316 L: fatigue life increased at high stress amplitudes but decreased at low stress amplitudes, while the fatigue limit was reduced relative to that measured in air. These findings show that any beneficial fatigue response is also conditional on hydrogen content and distribution, charging route, loading condition, and deformation mechanism, rather than representing a general improvement in hydrogen compatibility. Although the limited studies discussed above demonstrate that solute hydrogen can be also beneficial under cyclic loading too and retard fatigue-crack growth or delay crack initiation under particular conditions, it remains unresolved whether hydrogen-enhanced twinning or microbanding, beneficial under some monotonic loading conditions, can reliably improve cyclic resistance, or instead promotes crack initiation through localized slip, twin-boundary stress concentration, or hydrogen accumulation under other conditions. Systematic fatigue testing across controlled hydrogen concentrations, charging routes, stress amplitudes, loading frequencies, and microstructures is therefore required, particularly for the alloy families discussed in this work.

Finally, the broader implication of this research extends beyond traditional steels. The concepts discussed here, hydrogen as a solid-solution strengthener, hydrogen-stabilized planar slip, and hydrogen-enhanced interface-mediated plasticity, are directly relevant to high-entropy alloys, medium-entropy alloys, and other complex high–SFE FCC systems. These materials offer expanded compositional freedom and may provide more robust platforms for exploiting hydrogen-enhanced mechanisms while avoiding classical embrittlement pathways. An important and largely unexplored research direction concerns hydrogen-enhanced plasticity mechanisms under cyclic and multiaxial loading conditions. The present review focuses primarily on monotonic tensile behavior; however, austenitic steels in hydrogen service frequently experience cyclic loading, forming operations, and complex stress states.

8. Conclusions

This review has critically examined the evolving role of hydrogen in austenitic steels, moving beyond the long-standing perception of hydrogen as an inherently deleterious element toward a more nuanced and mechanism-based understanding. By integrating experimental observations, theoretical insights, and recent advances in characterization and modeling, it becomes clear that hydrogen's influence on mechanical behavior is not universally embrittling, but strongly dependent on the interplay of alloy chemistry, microstructure, deformation mechanism, and hydrogen charging conditions.

These initially surprising observations appeared contradictory to the established HEDE and HELP embrittlement frameworks, where hydrogen is expected to weaken atomic bonds or promote destructive slip localization. Reconciling this apparent paradox, determining when and why hydrogen transitions from embrittling to enhancing, was a central motivation for this review. As discussed throughout this work, hydrogen-induced modification of SFE may contribute to the transition between beneficial and detrimental responses by shifting deformation toward twinning-dominated behavior or, under some conditions, toward martensitic instability. However, this represents only one possible pathway, and its significance depends on alloy composition, initial SFE, hydrogen uptake, and microstructural state. Other mechanisms, including hydrogen-induced solid-solution strengthening and changes in dislocation mobility and kinetics, may also contribute and can become dominant in a particular alloy system. Accordingly, the observed response should be regarded as the outcome of competing, composition- and microstructure-dependent mechanisms rather than being governed by a universal SFE-based criterion. In addition, most beneficial responses discussed in this review were measured in monotonic tensile tests under specific hydrogen-introduction histories. Limited fatigue studies indicate that beneficial effects may also occur under cyclic loading, but these appear to be conditional and non-monotonic rather than indicative of generally improved hydrogen compatibility. Therefore, based on this work, no broader inference should be made regarding fatigue or fatigue-crack growth, sustained-load cracking, multiaxial behavior, fracture toughness, or long-term service performance without further research and dedicated testing under the relevant exposure and loading conditions.

Experimental observations and atomistic modeling collectively indicate that in stable high–SFE FCC alloy systems, hydrogen can act as an active and beneficial interstitial solute element, contributing to solid-solution strengthening and modifying dislocation-mediated plasticity rather than primarily reducing atomic cohesion or bulk SFE. Proposed, non-exclusive pathways include stabilization of dissociated partial dislocations, suppression of cross-slip, and hydrogen-induced solid-solution strengthening that raises the flow stress, allowing twinning or microbanding to be activated at a lower strain. The relative contribution of these pathways remains

dependent on alloy composition, microstructure, hydrogen state, and testing conditions. Deformation mechanisms such as hydrogen-enhanced densified twinning and hydrogen-enhanced microbanding exemplify how hydrogen can positively facilitate plastic deformation when phase instability and grain-boundary-dominated fracture are avoided. At the same time, this review highlighted the intrinsic duality of hydrogen's role. The same interfaces and defect structures that underpin HEP, twin boundaries, microbands, and their intersections, can also act as hydrogen segregation sites and stress concentrators, potentially promoting crack initiation at higher hydrogen concentrations or under dynamic charging. Consequently, HEP and hydrogen-assisted fracture should be viewed as competing and often coexisting phenomena, rather than mutually exclusive mechanisms.

A key conclusion of this work is that traditional HE frameworks, such as HEDE and HELP, while essential, are insufficient on their own to explain the full spectrum of hydrogen effects observed in modern austenitic steels. Instead, a unified perspective is required, one that explicitly considers local, defect-scale interactions between hydrogen, dislocations, and evolving microstructures, while distinguishing bulk thermodynamic effects from localized kinetic phenomena.

Ultimately, the findings reviewed here support a paradigm shift in alloy design philosophy. Rather than focusing exclusively on hydrogen avoidance, future austenitic steels can be deliberately engineered to operate within hydrogen-compatible regimes, where hydrogen-enhanced strengthening and ductilization mechanisms are activated while classical embrittlement pathways are suppressed. Achieving this goal will require coordinated advances in alloy chemistry, microstructural control, in-situ characterization, and multiscale modeling. If successfully realized, this approach has the potential to transform hydrogen from a long-standing adversary into a controllable and even beneficial contributor in the design of next-generation structural materials for hydrogen-rich environments.

CRediT authorship contribution statement

Vahid Javaheri: Writing – original draft, Conceptualization, Formal analysis, Validation, Visualization, Funding acquisition, Supervision. **Mahsa Barati Mahyari:** Writing – original draft, Writing – review & editing, Formal analysis, Validation, Visualization. **Mohammad Moallemi:** Writing – original draft, Writing – review & editing, Formal analysis, Validation. **Pentti Karjalainen:** Writing – review & editing, Validation, Formal analysis. **Lisa Claeys:** Writing – review & editing, Formal analysis. **Liese Vandewalle:** Writing – review & editing, Formal analysis. **Rebecca Janisch:** Writing – review & editing, Validation, Formal analysis. **Hosni Idrissi:** Writing – review & editing, Validation, Formal analysis. **Yuhei Ogawa:** Writing – review & editing. **Jukka Kömi:** Writing – review & editing, Funding acquisition. **Kim Verbeken:** Writing – review & editing, Conceptualization, Formal analysis, Supervision.

Declaration of competing interest

The authors declare that they have no known competing financial interests or personal relationships that could have appeared to influence the work reported in this paper.

Acknowledgments

Authors affiliated with the University of Oulu gratefully acknowledge the University of Oulu and the Research Council of Finland Profi 352788 for their funding of the H2Future project. The authors also thank Mahmoud Elaraby for his kind help with the SFE calculations presented in Fig. 20.

Declaration of generative AI use

During the preparation of this work, ChatGPT was used for the language editing and grammar and readability improvement. The authors reviewed and edited the output as needed and take full responsibility for the content of the published article.

Appendix A. Supplementary data

Supplementary data to this article can be found online at https://doi.org/10.1016/j.pmatsci.2026.101865.

Data availability

Data will be made available on request.

References

[1] Chen YS, Huang C, Liu PY, Yen HW, Niu R, Burr P, et al. Hydrogen trapping and embrittlement in metals – a review. Int J Hydrogen Energy 2025;136:789–821. https://doi.org/10.1016/j.ijhydene.2024.04.076.
[2] Oriani RA. A mechanistic theory of hydrogen embrittlement of steels. Berichte Der Bunsengesellschaft Für Physikalische Chemie 1972;76:848–57. https://doi.org/10.1002/bbpc.19720760864.
[3] Martin ML, Sofronis P. Hydrogen-induced cracking and blistering in steels: a review. J Nat Gas Sci Eng 2022;101. https://doi.org/10.1016/j.jngse.2022.104547.

[4] Lijie Q, Wuyang C, Huijun M, Jimei X, Peixin G. Hydrogen-facilitated corrosion and stress corrosion cracking of austenitic stainless steel of type 310. Metall Trans A 1993;24:959–62. https://doi.org/10.1007/BF02656517.

[5] Yu H, Díaz A, Lu X, Sun B, Ding Y, Koyama M, et al. Hydrogen embrittlement as a conspicuous material challenge—comprehensive review and future directions. Chem Rev 2024;124:6271–392. https://doi.org/10.1021/acs.chemrev.3c00624.

[6] Koyama M, Akiyama E, Lee Y-K, Raabe D, Tsuzaki K. Overview of hydrogen embrittlement in high-Mn steels. Int J Hydrogen Energy 2017;42:12706–23. https://doi.org/10.1016/j.ijhydene.2017.02.214.

[7] Moallemi M, Kim S-H, Kim S-J. Hydrogen embrittlement in a metastable high Mn TWIP-assisted steel: Correlation between grain size and hydrogen-enhanced ε-martensite. Mater Sci Eng A 2023;885:145595. https://doi.org/10.1016/j.msea.2023.145595.

[8] Bai Y, Momotani Y, Chen MC, Shibata A, Tsuji N. Effect of grain refinement on hydrogen embrittlement behaviors of high-Mn TWIP steel. Mater Sci Eng A 2016;651:935–44. https://doi.org/10.1016/j.msea.2015.11.017.

[9] Kwon YJ, Seo HJ, Kim JN, Lee CS. Effect of grain boundary engineering on hydrogen embrittlement in Fe-Mn-C TWIP steel at various strain rates. Corros Sci 2018;142:213–21. https://doi.org/10.1016/j.corsci.2018.07.028.

[10] Wang D, Lu X, Deng Y, Guo X, Barnoush A. Effect of hydrogen on nanomechanical properties in Fe-22Mn-0.6C TWIP steel revealed by in-situ electrochemical nanoindentation. Acta Mater 2019;166:618–29. https://doi.org/10.1016/j.actamat.2018.12.055.

[11] Louthan MR, Caskey GR, Donovan JA, Rawl DE. Hydrogen embrittlement of metals. Mater Sci Eng 1972;10:357–68. https://doi.org/10.1016/0025-5416(72)90109-7.

[12] Troiano AR. The role of hydrogen and other interstitials in the mechanical behavior of metals. Trans Am Soc Met 1960:54–80.

[13] Birnbaum HK, Sofronis P. Hydrogen-enhanced localized plasticity—a mechanism for hydrogen-related fracture. Mater Sci Eng A 1994;176:191–202. https://doi.org/10.1016/0921-5093(94)90975-X.

[14] Li X, Ma X, Zhang J, Akiyama E, Wang Y, Song X. Review of hydrogen embrittlement in metals: hydrogen diffusion, hydrogen characterization, hydrogen embrittlement mechanism and prevention. Acta Metall Sin (Engl Lett) 2020;33:759–73. 10.1007/s40195-020-01039-7.

[15] Ogawa Y, Shibata A. Refining hydrogen-dislocation interaction model for thermally activated plasticity in Fe-Cr-Ni austenitic steels: Analyzing stress-dependent activation volume. Acta Mater 2026;306. https://doi.org/10.1016/j.actamat.2026.121896.

[16] Ogawa Y, Shibata A. Plastic flow in Fe-Cr-Ni austenitic steel under the presence of solute H: a study via room temperature creep. Acta Mater 2025;285. https://doi.org/10.1016/j.actamat.2024.120659.

[17] Ogawa Y, Takakuwa O, Moriyama J, Nishida H, Tsuzaki K, Shibata A. Phenomenology and mechanisms of hydrogen–induced solid solution–hardening in Fe–Cr–Ni austenitic steels. Mater Trans 2026:MT-M2025161. 10.2320/matertrans.MT-M2025161.

[18] Kim HJ, Cho MK, Kim G, Lee SY, Jo MG, Kim H, et al. Influence of hydrogen absorption on stacking fault of energy of a face-centered cubic high entropy alloy. Met Mater Int 2022;28:2637–45. https://doi.org/10.1007/s12540-021-01163-8.

[19] Ogawa Y, Tanaka M, Fujita T, Shibata A. Thermally activated dislocation motion in hydrogen-alloyed Fe–Cr–Ni austenitic steel revisited via Haasen plot. Int J Hydrogen Energy 2024;74:170–82. https://doi.org/10.1016/j.ijhydene.2024.06.113.

[20] Luo H, Lu W, Fang X, Ponge D, Li Z, Raabe D. Beating hydrogen with its own weapon: Nano-twin gradients enhance embrittlement resistance of a high-entropy alloy. Mater Today 2018;21:1003–9. https://doi.org/10.1016/j.mattod.2018.07.015.

[21] Ito T, Ogawa Y, Gong W, Mao W, Kawasaki T, Okada K, et al. Role of solute hydrogen on mechanical property enhancement in Fe–24Cr–19Ni austenitic steel: an in-situ neutron diffraction study. Acta Mater 2025;287. https://doi.org/10.1016/j.actamat.2025.120767.

[22] Kong Y, Kathayat P, Williamson A, Brown DW, Lawrence SK, Clausen B, et al. Influence of stacking fault energy and hydrogen on deformation mechanisms in high Mn austenitic steels during in-situ tensile testing. Int J Hydrogen Energy 2025;148. https://doi.org/10.1016/j.ijhydene.2025.06.023.

[23] Luo H, Li Z, Raabe D. Hydrogen enhances strength and ductility of an equiatomic high-entropy alloy. Sci Rep 2017;7. https://doi.org/10.1038/s41598-017-10774-4.

[24] Gutierrez-Urrutia I, Ogawa Y, Shibata A. Hydrogen-enhanced microbanding in an austenitic FeMnAlC low-density steel: effect on hydrogen embrittlement resistance. Acta Mater 2024;280. https://doi.org/10.1016/j.actamat.2024.120335.

[25] Ogawa Y, Hosoi H, Tsuzaki K, Redarce T, Takakuwa O, Matsunaga H. Hydrogen, as an alloying element, enables a greater strength-ductility balance in an Fe-Cr-Ni-based, stable austenitic stainless steel. Acta Mater 2020;199:181–92. https://doi.org/10.1016/j.actamat.2020.08.024.

[26] Astafurova EG, Zakharova GG, Maier HJ. Hydrogen-induced twinning in ⟨0 0 1⟩ Hadfield steel single crystals. Scr Mater 2010;63:1189–92. https://doi.org/10.1016/j.scriptamat.2010.08.029.

[27] Yamada K, Koyama M, Kaneko T, Tsuzaki K. Positive and negative effects of hydrogen on tensile behavior in polycrystalline Fe-30Mn-(6 - X)Si-XAl austenitic alloys. Scr Mater 2015;105:54–7. https://doi.org/10.1016/j.scriptamat.2015.05.007.

[28] Lai ZH, Lin YT, Sun YH, Tu JF, Yen HW. Hydrogen-induced ductilization in a novel austenitic l ightweight TWIP steel. Scr Mater 2022;213. https://doi.org/10.1016/j.scriptamat.2022.114629.

[29] Cho L, Kong Y, Kathayat P, Brown DW, Lawrence SK, Clausen B, et al. Influence of hydrogen on deformation and embrittlement mechanisms in a high Mn austenitic steel: In-Situ neutron diffraction and diffraction line profile analysis. Acta Mater 2024;281. https://doi.org/10.1016/j.actamat.2024.120420.

[30] Zhang C, Zhi H, Antonov S, Chen L, Su Y. Hydrogen-enhanced densified twinning (HEDT) in a twinning-induced plasticity (TWIP) steel. Scr Mater 2021;190:108–12. https://doi.org/10.1016/j.scriptamat.2020.08.047.

[31] Sabisch JEC, Sugar JD, Ronevich J, San Marchi C, Medlin DL. Interrogating the effects of hydrogen on the behavior of planar deformation bands in austenitic stainless steel. Metall Mater Trans A 2021;52:1516–25. https://doi.org/10.1007/s11661-021-06170-3.

[32] Zambrano OA. Stacking fault energy maps of Fe-Mn-Al-C-Si steels: effect of temperature, grain size, and variations in compositions. J Eng Mater Technol, Transactions of the ASME 2016;138. https://doi.org/10.1115/1.4033632.

[33] Pierce DT, Jiménez JA, Bentley J, Raabe D, Oskay C, Wittig JE. The influence of manganese content on the stacking fault and austenite/ε-martensite interfacial energies in Fe-Mn-(Al-Si) steels investigated by experiment and theory. Acta Mater 2014;68:238–53. https://doi.org/10.1016/j.actamat.2014.01.001.

[34] Pierce DT, Jiménez JA, Bentley J, Raabe D, Wittig JE. The influence of stacking fault energy on the microstructural and strain-hardening evolution of Fe-Mn-Al-Si steels during tensile deformation. Acta Mater 2015;100:178–90. https://doi.org/10.1016/j.actamat.2015.08.030.

[35] Barrera O, Bombac D, Chen Y, Daff TD, Galindo-Nava E, Gong P, et al. Understanding and mitigating hydrogen embrittlement of steels: a review of experimental, modelling and design progress from atomistic to continuum. J Mater Sci 2018;53:6251–90. https://doi.org/10.1007/s10853-017-1978-5.

[36] Ismer L, Hickel T, Neugebauer J. *Ab initio* study of the solubility and kinetics of hydrogen in austenitic high Mn steels. Phys Rev B 2010;81:094111. https://doi.org/10.1103/PhysRevB.81.094111.

[37] Hüter C, Dang S, Zhang X, Glensk A, Spatschek R. Effects of aluminum on hydrogen solubility and diffusion in deformed fe-mn alloys. Adv Mater Sci Eng 2016;2016:1–9. https://doi.org/10.1155/2016/4287186.

[38] Moriyama J, Yamaguchi M, Takakuwa O. Effects of antagonistic interaction between Cr and Ni on hydrogen solubility in a Fe-Cr-Ni ternary austenitic system: a first-principles calculation. Mater Today Commun 2024;40:110059. https://doi.org/10.1016/j.mtcomm.2024.110059.

[39] Vandewalle L, Depover T, Verbeken K. Current state-of-the-art of hydrogen trapping by carbides: from theory to experiment. Int J Hydrogen Energy 2025;136:888–901. https://doi.org/10.1016/j.ijhydene.2024.03.266.

[40] Oriani RA. The diffusion and trapping of hydrogen in steel. Acta Metall 1970;18:147–57. https://doi.org/10.1016/0001-6160(70)90078-7.

[41] McNabb A, K. Foster P. A new analysis of the diffusion of hydrogen in iron and ferritic steels. Trans Metall Soc AIME 1963;227:618–27.

[42] Krom AHM, Koers RWJ, Bakker A. Hydrogen transport near a blunting crack tip. J Mech Phys Solids 1999;47:971–92. https://doi.org/10.1016/S0022-5096(98)00064-7.

[43] Danilkin SA, Fuess H, Wipf H, Ivanov A, Gavriljuk VG, Delafosse D, et al. Hydrogen vibrations in austenitic fcc Fe-Cr-Mn-Ni steels. Europhysics Letters (EPL) 2003;63:69–75. https://doi.org/10.1209/epl/i2003-00479-1.

[44] Yagodzinskyy Y, Todoshchenko O, Papula S, Hänninen H. Hydrogen solubility and diffusion in austenitic stainless steels studied with thermal desorption spectroscopy. Steel Res Int 2011;82:20–5. https://doi.org/10.1002/srin.201000227.

[45] Hua Z, Zhu S, Zhang Y, Liu Z, Cui T. A method to calculate hydrogen trap binding energy in austenitic stainless steel using local equilibrium model. Int J Hydrogen Energy 2018;43:22676–84. https://doi.org/10.1016/j.ijhydene.2018.10.079.
[46] Atrens A, Fiore NF, Miura K. Dislocation damping and hydrogen pinning in austenitic stainless steels. J Appl Phys 1977;48:4247–51. https://doi.org/10.1063/1.323410.
[47] Bestautte J, Oudriss A, Lenci M, Bechet D, Obadia Z, Feaugas X, et al. A multi-method approach to the study of hydrogen trapping in a maraging stainless steel: the impact of B2-NiAl precipitates and austenite. Corros Sci 2023;224:111509. https://doi.org/10.1016/j.corsci.2023.111509.
[48] Enomoto M, Cheng L, Mizuno H, Watanabe Y, Omura T, Sakai J, et al. Hydrogen absorption into austenitic stainless steels under high-pressure gaseous hydrogen and cathodic charge in aqueous solution. Metall Mater Trans E 2014;1:331–40.
[49] Rousseau C, Oudriss A, Milet R, Feaugas X, El May M, Saintier N, et al. Effect of aging treatment on apparent hydrogen solubility and trapping in a new generation maraging steel. Scr Mater 2020;183:144–8. https://doi.org/10.1016/j.scriptamat.2020.03.013.
[50] Taketomi S, Matsumoto R, Miyazaki N. Atomistic study of hydrogen distribution and diffusion around a {1 1 2}<1 1 1> edge dislocation in alpha iron. Acta Mater 2008;56:3761–9. https://doi.org/10.1016/j.actamat.2008.04.011.
[51] Frappart S, Oudriss A, Feaugas X, Creus J, Bouhattate J, Thébault F, et al. Hydrogen trapping in martensitic steel investigated using electrochemical permeation and thermal desorption spectroscopy. Scr Mater 2011;65:859–62. https://doi.org/10.1016/j.scriptamat.2011.07.042.
[52] Ono K, Meshii M. Hydrogen detrapping from grain boundaries and dislocations in high purity iron. Acta Metall Mater 1992;40:1357–64. https://doi.org/10.1016/0956-7151(92)90436-I.
[53] Hirata K, Iikubo S, Koyama M, Tsuzaki K, Ohtani H. First-principles study on hydrogen diffusivity in BCC, FCC, and HCP iron. Mater Sci Eng A 2018;49:5015–22. https://doi.org/10.1007/s11661-018-4815-9.
[54] Kuhr B, Farkas D, Robertson IM. Atomistic studies of hydrogen effects on grain boundary structure and deformation response in FCC Ni. Comput Mater Sci 2016;122:92–101. https://doi.org/10.1016/j.commatsci.2016.05.014.
[55] He Y, Su Y, Yu H, Chen C. First-principles study of hydrogen trapping and diffusion at grain boundaries in γ-Fe. Int J Hydrogen Energy 2021;46:7589–600. https://doi.org/10.1016/j.ijhydene.2020.11.238.
[56] Suh D-W. Critical Assessment 2: Hydrogen induced fracture in austenitic, high-manganese TWIP steel. J Mater Sci Technol 2014;30:1131–4. https://doi.org/10.1179/1743284714Y.0000000566.
[57] So KH, Kim JS, Chun YS, Park K-T, Lee Y-K, Lee CS. Hydrogen delayed fracture properties and internal hydrogen behavior of a Fe–18Mn–1.5Al–0.6C TWIP steel. ISIJ Int 2009;49:1952–9. https://doi.org/10.2355/isijinternational.49.1952.
[58] Jeong C-G, Trang TTT, Kim Y-S, Jun HJ, Jin H-W, Suh J-Y, et al. Microstructure-strength interplay governing hydrogen embrittlement in micro-alloyed high-Mn steels. Mater Sci Eng A 2026;960:150055. https://doi.org/10.1016/j.msea.2026.150055.
[59] Chun YS, Kim JS, Park K-T, Lee Y-K, Lee CS. Role of ε martensite in tensile properties and hydrogen degradation of high-Mn steels. Mater Sci Eng A 2012;533:87–95. https://doi.org/10.1016/j.msea.2011.11.039.
[60] Xing W, Chen X-Q, Li X, Ma Y, Chen B, Liu K. First-principles study of hydrogen trapping behavior in face centered cubic metals (M=Ni, Cu and Al) with monovacancy. Int J Hydrogen Energy 2020;45:25555–66. https://doi.org/10.1016/j.ijhydene.2020.06.266.
[61] Nazarov R, Hickel T, Neugebauer J. *Ab initio* study of H-vacancy interactions in FCC metals: Implications for the formation of superabundant vacancies. Phys Rev B 2014;89:144108. https://doi.org/10.1103/PhysRevB.89.144108.
[62] Nazarov R, Hickel T, Neugebauer J. First-principles study of the thermodynamics of hydrogen-vacancy interaction in FCC iron. Phys Rev B 2010;82:224104. https://doi.org/10.1103/PhysRevB.82.224104.
[63] Oudriss A, Creus J, Bouhattate J, Conforto E, Berziou C, Savall C, et al. Grain size and grain-boundary effects on diffusion and trapping of hydrogen in pure nickel. Acta Mater 2012;60:6814–28. https://doi.org/10.1016/j.actamat.2012.09.004.
[64] Das BK, Chakraborty P, Lu M, Bonilla MR, Akhmatskaya E. The impact of Mn and Al on the trapping and diffusion of hydrogen in γ-Fe: an atomistic insight. Int J Hydrogen Energy 2024;83:731–44. https://doi.org/10.1016/j.ijhydene.2024.06.322.
[65] Moriyama J, Takakuwa O, Yamaguchi M, Ogawa Y, Tsuzaki K. The contribution of Cr and Ni to hydrogen absorption energy in Fe-Cr-Ni austenitic systems: a first-principles study. Comput Mater Sci 2024;232:112650. https://doi.org/10.1016/j.commatsci.2023.112650.
[66] Brass AM, Chanfreau A. Accelerated diffusion of hydrogen along grain boundaries in nickel. Acta Mater 1996;44:3823–31. https://doi.org/10.1016/1359-6454(95)00446-7.
[67] Boda A, Ali SM. First principles DFT analysis on the diffusion kinetics of hydrogen isotopes through BCC iron (Fe): Role of temperature and surface coverage. Int J Hydrogen Energy 2022;47:31481–98. https://doi.org/10.1016/j.ijhydene.2022.07.055.
[68] Xiukui S, Jian X, Yiyi L. Hydrogen permeation behaviour in austenitic stainless steels. Mater Sci Eng A 1989;114:179–87. https://doi.org/10.1016/0921-5093(89)90857-5.
[69] Takai K, Kitamura M. Hydrogen dragging by moving dislocation and enhanced lattice defect formation in 316l and 304 stainless steels. Mater Fabr, ASME 2013. https://doi.org/10.1115/PVP2013-97231.
[70] Nibur KA, Somerday BP, Balch DK, San MC. The role of localized deformation in hydrogen-assisted crack propagation in 21Cr–6Ni–9Mn stainless steel. Acta Mater 2009;57:3795–809. https://doi.org/10.1016/j.actamat.2009.04.027.
[71] Zhang L, An B, Fukuyama S, Iijima T, Yokogawa K. Characterization of hydrogen-induced crack initiation in metastable austenitic stainless steels during deformation. J Appl Phys 2010;108. https://doi.org/10.1063/1.3477321.
[72] Schuster G, Altstetter C. Fatigue of stainless steel in hydrogen. Metall Trans A 1983;14:2085–90. https://doi.org/10.1007/BF02662375.
[73] Holzworth ML, Louthan MR. Hydrogen-induced phase transformations in type 304L stainless steels. Corrosion 1968;24:110–24. https://doi.org/10.5006/0010-9312-24.4.110.
[74] Zhou XW, Nowak C, Skelton RS, Foster ME, Ronevich JA, San Marchi C, et al. An Fe–Ni–Cr–H interatomic potential and predictions of hydrogen-affected stacking fault energies in austenitic stainless steels. Int J Hydrogen Energy 2022;47:651–65. https://doi.org/10.1016/j.ijhydene.2021.09.261.
[75] Pontini AE, Daniel Hermida' J. X-RAY diffraction measurement of the stacking fault energy r eduction induced by hydrogen in an AISI 304 steel. Scr Mater, vol. 37. 1997. 10.1016/S1359-6462(97)00332-1.
[76] Inoue A, Hosoya Y, Masumoto T. The effect of hydrogen on crack propagation behavior and microstructures around cracks in austenitic stainless steels. Trans Iron Steel Inst Jpn 1979;19:170–8. https://doi.org/10.2355/isijinternational1966.19.170.
[77] Robertson IM. The effect of hydrogen on dislocation dynamics. Eng Fract Mech 1999;64:649–73. https://doi.org/10.1016/S0013-7944(99)00094-6.
[78] Ferreira PJ, Robertson IM, Birnbaum HK. Influence of hydrogen on the stacking-fault energy of an austenitic stainless steel. Mater Sci Forum 1996;207–209:93–6. https://doi.org/10.4028/www.scientific.net/MSF.207-209.93.
[79] Hermida JD, Roviglione A. Stacking fault energy decrease in austenitic stainless steels induced by hydrogen pairs formation. Scr Mater 1998;39:1145–9. https://doi.org/10.1016/S1359-6462(98)00285-1.
[80] Lawrence SK, Pokharel R, Clausen B, Brown DW, San Marchi C, O'Brien MK, et al. In Situ X-ray diffraction investigation of hydrogen effects on deformation-induced phase transformation in forged and additively manufactured 304L stainless steels. JOM 2023;75:2287–98. https://doi.org/10.1007/s11837-023-05787-6.
[81] Gibbs PJ, Hough PD, Thürmer K, Somerday BP, San Marchi C, Zimmerman JA. Stacking fault energy based alloy screening for hydrogen compatibility. JOM 2020;72:1982–92. https://doi.org/10.1007/s11837-020-04106-7.
[82] Li Y, He Y, Liu S, Wang Y, Ma X. First-principles study the effect of hydrogen atoms on the generalized stacking fault energy in γ-Fe. Int J Hydrogen Energy 2024;82:1446–54. https://doi.org/10.1016/j.ijhydene.2024.07.431.
[83] He Y, Li Y, Zhao X, Yu H, Chen C. Effect of hydrogen atom and hydrogen filled vacancies on stacking fault energy in γ-Fe by first-principles calculations. Int J Hydrogen Energy 2019;44:17136–45. https://doi.org/10.1016/j.ijhydene.2019.04.229.
[84] Tang Y, El-Awady JA. Atomistic simulations of the interactions of hydrogen with dislocations in FCC metals. Phys Rev B 2012;86:174102. https://doi.org/10.1103/PhysRevB.86.174102.

[85] Jin W-L, Cao J-L, Li J-X. Combined effects of Mn, C, and H on the stacking fault energy in austenitic Mn steels. Steel Res Int 2021;92. https://doi.org/10.1002/srin.202000550.
[86] Movchan DN, Shanina BD, Gavriljuk VG. Hydrogen effect on thermodynamic stability of γ- and ε-phases in a Fe–Cr–Mn solid solution. Int J Hydrogen Energy 2013;38:8471–7. https://doi.org/10.1016/j.ijhydene.2013.04.145.
[87] Xie Z, Wang Y, Lu C, Dai L. Sluggish hydrogen diffusion and hydrogen decreasing stacking fault energy in a high-entropy alloy. Mater Today Commun 2021;26:101902. https://doi.org/10.1016/j.mtcomm.2020.101902.
[88] Shi H, Nandy S, Cheng H, Sun B, Ponge D. In-situ investigation of the interaction between hydrogen and stacking faults in a bulk austenitic steel. Acta Mater 2024;262. https://doi.org/10.1016/j.actamat.2023.119441.
[89] Michler T, San Marchi C, Naumann J, Weber S, Martin M. Hydrogen environment embrittlement of stable austenitic steels. Int J Hydrogen Energy 2012;37:16231–46. https://doi.org/10.1016/j.ijhydene.2012.08.071.
[90] Zhou C, Tang D, Zhang K, Wu F, Lin P, Jin Y, et al. Effect of manganese content on the hydrogen embrittlement of twinning-induced plasticity (TWIP) steels under hydrogen charging and hydrogen environment. Mater Sci Eng A 2022;861:144289. https://doi.org/10.1016/j.msea.2022.144289.
[91] Elkot MN, Sun B, Zhou X, Ponge D, Raabe D. Hydrogen-assisted decohesion associated with nanosized grain boundary κ-carbides in a high-Mn lightweight steel. Acta Mater 2022;241. https://doi.org/10.1016/j.actamat.2022.118392.
[92] Koyama M, Akiyama E, Sawaguchi T, Raabe D, Tsuzaki K. Hydrogen-induced cracking at grain and twin boundaries in an Fe-Mn-C austenitic steel. Scr Mater 2012;66:459–62. https://doi.org/10.1016/j.scriptamat.2011.12.015.
[93] Park I-J, Jeong K-H, Jung J-G, Lee CS, Lee Y-K. The mechanism of enhanced resistance to the hydrogen delayed fracture in Al-added Fe–18Mn–0.6C twinning-induced plasticity steels. Int J Hydrogen Energy 2012;37:9925–32. https://doi.org/10.1016/j.ijhydene.2012.03.100.
[94] Moallemi M, Kim S-J, Cho H-J, Kim SH, Javaheri V. Design considerations for hydrogen embrittlement resistance: the influence of dislocation density and substructures on hydrogen-assisted cracking in high-Mn TWIP steel. Mater Des 2025;256:114298. https://doi.org/10.1016/j.matdes.2025.114298.
[95] Moallemi M, Cho HJ, Kim SJ. The adverse effect of grain refinement on hydrogen embrittlement in a high Mn austenitic steel. Mater Sci Eng A 2024;916. https://doi.org/10.1016/j.msea.2024.147367.
[96] Koyama M, Akiyama E, Tsuzaki K. Hydrogen embrittlement in a Fe–Mn–C ternary twinning-Induced plasticity steel. Corros Sci 2012;54:1–4. https://doi.org/10.1016/j.corsci.2011.09.022.
[97] Koyama M, Akiyama E, Tsuzaki K, Raabe D. Hydrogen-assisted failure in a twinning-induced plasticity steel studied under in situ hydrogen charging by electron channeling contrast imaging. Acta Mater 2013;61:4607–18. https://doi.org/10.1016/j.actamat.2013.04.030.
[98] Wang D, Lu X, Wan D, Guo X, Johnsen R. Effect of hydrogen on the embrittlement susceptibility of Fe–22Mn-0.6C TWIP steel revealed by in-situ tensile tests. Mater Sci Eng A 2021;802:140638. https://doi.org/10.1016/j.msea.2020.140638.
[99] Khanchandani H, Ponge D, Zaefferer S, Gault B. Hydrogen-induced hardening of a high-manganese twinning induced plasticity steel. Materialia 2023;28:101776. https://doi.org/10.1016/j.mtla.2023.101776.
[100] Hao C, Koyama M, Akiyama E. Quantitative evaluation of hydrogen effects on evolutions of deformation-induced ε-martensite and damage in a high-Mn steel. metallurgical and materials transactions a 2020;51:6184–94. 10.1007/s11661-020-06021-7.
[101] Fu H, Wang W, Zhao H, Jin F, Li J. Study of hydrogen-induced delayed fracture in high-Mn T WIP/TRIP steels during in situ electrochemical hydrogen-charging: Role of microstructure and strain rate in crack initiation and propagation. Corros Sci 2020;162:108191. https://doi.org/10.1016/j.corsci.2019.108191.
[102] Park I-J, Jung J-G, Jo SY, Lee S-M, Lee Y-K. The effect of pre-strain on the resistance to hydrogen embrittlement in 316L austenitic stainless steel. Mater Trans 2014;55:964–70. https://doi.org/10.2320/matertrans.M2014036.
[103] Mao LY, Luo ZA, Huang C, Zhang XM. Hydrogen embrittlement behavior in interstitial Mn–N austenitic stainless steel. Int J Hydrogen Energy 2022;47:36716–32. https://doi.org/10.1016/j.ijhydene.2022.08.211.
[104] Xiong Y, Guo X, Dong H. Impact of size and distribution of k-carbides on the hydrogen embrittlement and trapping behaviors of a Fe-Mn-Al-C low-density steel. Materials 2024;17. https://doi.org/10.3390/ma17112698.
[105] Koyama M, Springer H, Merzlikin SV, Tsuzaki K, Akiyama E, Raabe D. Hydrogen embrittlement associated with strain localization in a precipitation-hardened Fe-Mn-Al-C light weight austenitic steel. Int J Hydrogen Energy 2014;39:4634–46. https://doi.org/10.1016/j.ijhydene.2013.12.171.
[106] Lee SY, Gao Z, Choi JH, Zhao Y, Wang P, Murakami K, et al. A novel specimen geometry for an improved estimation of hydrogen effects on the tensile behavior of face-centered cubic alloys. Scr Mater 2026;280. https://doi.org/10.1016/j.scriptamat.2026.117361.
[107] Christian JW, Mahajan S. Deformation twinning. Prog Mater Sci 1995;39:1–157. https://doi.org/10.1016/0079-6425(94)00007-7.
[108] Venables JA. Deformation twinning in face-centred cubic metals. Phil Mag 1961;6:379–96. https://doi.org/10.1080/14786436108235892.
[109] Cohen JB, Weertman J. A dislocation model for twinning in FCC metals. Acta Metall 1963;11:996–8. https://doi.org/10.1016/0001-6160(63)90074-9.
[110] Mahajan S, Chin GY. Formation of deformation twins in FCC crystals. Acta Metall 1973;21:1353–63. https://doi.org/10.1016/0001-6160(73)90085-0.
[111] Idrissi H, Renard K, Ryelandt L, Schryvers D, Jacques PJ. On the mechanism of twin formation in Fe–Mn–C TWIP steels. Acta Mater 2010;58:2464–76. https://doi.org/10.1016/j.actamat.2009.12.032.
[112] Idrissi H, Renard K, Schryvers D, Jacques PJ. TEM investigation of the formation mechanism of deformation twins in Fe–Mn–Si–Al TWIP steels. Phil Mag 2013;93:4378–91. https://doi.org/10.1080/14786435.2013.832837.
[113] Mahato B, Shee SK, Sahu T, Ghosh Chowdhury S, Sahu P, Porter DA, et al. An effective stacking fault energy viewpoint on the formation of extended defects and their contribution to strain hardening in a Fe–Mn–Si–Al twinning-induced plasticity steel. Acta Mater 2015;86:69–79. https://doi.org/10.1016/j.actamat.2014.12.015.
[114] Ghiasabadi Farahani M, Kim JH, Jaskari M, Karjalainen LP, Sahu P. Newer insights into the discrimination of pole mechanisms of twinning in a face-centered cubic high-Mn steel. Materialia 2022;21:101349. https://doi.org/10.1016/j.mtla.2022.101349.
[115] Ding L, Hilhorst A, Idrissi H, Jacques PJ. Potential TRIP/TWIP coupled effects in equiatomic CrCoNi medium-entropy alloy. Acta Mater 2022;234:118049. https://doi.org/10.1016/j.actamat.2022.118049.
[116] Ghiasabadi Farahani M, Barati Rizi M, Aghaahmadi M, Kang J-H, Pallaspuro S, Karjalainen LP, et al. Activation of different twinning mechanisms and their contributions to mechanical behavior of a face-centered cubic Co-based high-entropy alloy. Acta Mater 2025;285:120665. https://doi.org/10.1016/j.actamat.2024.120665.
[117] Chateau JP, Delafosse D, Magnin T. Numerical simulations of hydrogen–dislocation interactions in FCC stainless steels. Acta Mater 2002;50:1507–22. https://doi.org/10.1016/S1359-6454(02)00008-3.
[118] Delafosse D, Magnin T. Hydrogen induced plasticity in stress corrosion cracking of engineering systems. Eng Fract Mech 2001;68:693–729. https://doi.org/10.1016/S0013-7944(00)00121-1.
[119] Mubarak AA. The elastic, electronic and magnetism structure of the MAl and M 3 Al (M=Fe and Ni) alloy with and without hydrogen atoms. J Magn Magn Mater 2016;401:816–22. https://doi.org/10.1016/j.jmmm.2015.11.015.
[120] León-Cázares FD, Zhou X, Kagay B, Sugar JD, Alleman C, Ronevich J, et al. Hydrogen effects on the deformation and slip localization in a single crystal austenitic stainless steel. Int J Plast 2024;180:104074. https://doi.org/10.1016/j.ijplas.2024.104074.
[121] Gutierrez-Urrutia I, Shibata A, Tsuzaki K. Microstructural study of microbands in a Fe-30Mn-6.5Al-0.3C low-density steel deformed at cryogenic temperature by combined electron channeling contrast imaging and electron backscatter diffraction. Acta Mater 2022;233. https://doi.org/10.1016/j.actamat.2022.117980.
[122] Yoo JD, Park KT. Microband-induced plasticity in a high Mn-Al-C light steel. Mater Sci Eng A 2008;496:417–24. https://doi.org/10.1016/j.msea.2008.05.042.
[123] Hughes DA, Liu Q, Chrzan DC, Hansen N. Scaling of microstructural parameters: misorientations of deformation induced boundaries. Acta Mater 1997;233. https://doi.org/10.1016/S1359-6454(96)00153-X.
[124] Abraham DP, Altstetter CJ. The effect of hydrogen on the yield and flow stress of an austenitic stainless steel. Metall Mater Trans A 1995;26:2849–58. https://doi.org/10.1007/BF02669643.

[125] Boniszewski T, Smith GC. The influence of hydrogen on the plastic deformation ductility, and fracture of nickel in tension. Acta Metall 1963;11:165–78. https://doi.org/10.1016/0001-6160(63)90209-8.
[126] Slater JC. Atomic radii in crystals. J Chem Phys 1964;41:3199–204. https://doi.org/10.1063/1.1725697.
[127] Fu P, Zheng Z, Yang W, Yang H. Influence of carbon addition on mechanical properties of Fe–Mn–C twinning-induced plasticity steels. J Iron Steel Res Int 2022; 29:1446–54. https://doi.org/10.1007/s42243-021-00688-x.
[128] Kusakin P, Belyakov A, Molodov DA, Kaibyshev R. On the effect of chemical composition on yield strength of TWIP steels. Mater Sci Eng A 2017;687:82–4. https://doi.org/10.1016/j.msea.2017.01.080.
[129] Ogawa Y, Takakuwa O, Tsuzaki K. Solid-solution hardening by hydrogen in Fe–Cr–Ni-based austenitic steel: Temperature and strain rate effects. Mater Sci Eng A 2023;879:145281. https://doi.org/10.1016/j.msea.2023.145281.
[130] Macadre A, Nakada N, Tsuchiyama T, Takaki S. Critical grain size to limit the hydrogen-induced ductility drop in a metastable austenitic steel. Int J Hydrogen Energy 2015;40:10697–703. https://doi.org/10.1016/j.ijhydene.2015.06.111.
[131] Fan YH, Zhang B, Wang JQ, Han EH, Ke W. Effect of grain refinement on the hydrogen embrittlement of 304 austenitic stainless steel. J Mater Sci Technol 2019;35:2213–9. https://doi.org/10.1016/j.jmst.2019.03.043.
[132] Zan N, Ding H, Guo X, Tang Z, Bleck W. Effects of grain size on hydrogen embrittlement in a Fe-22Mn-0.6C TWIP steel. Int J Hydrogen Energy 2015;40: 10687–96. https://doi.org/10.1016/j.ijhydene.2015.06.112.
[133] Park IJ, Lee S min, Jeon H hee, Lee YK. The advantage of grain refinement in the hydrogen embrittlement of Fe-18Mn-0.6C twinning-induced plasticity steel. Corros Sci 2015;93:63–9. 10.1016/j.corsci.2015.01.012.
[134] Noh HS, Kang JH, Kim SJ. Effect of grain size on hydrogen embrittlement in stable austenitic high-Mn TWIP and high-N stainless steels. Int J Hydrogen Energy 2019;44:25076–90. https://doi.org/10.1016/j.ijhydene.2019.07.227.
[135] Zhao C, Wu W, Deng J, Yu M, Peng Y, Wang X, et al. Hydrogen-induced delayed fracture behavior of notched 316L austenitic stainless steel: Role of grain refinement. Eng Fail Anal 2024;166. https://doi.org/10.1016/j.engfailanal.2024.108880.
[136] Wang Y, Han J, Zhao Y, Xie H, Li X, Dou D, et al. Grain refinement's effect on hydrogen embrittlement of 304 austenitic stainless steel: a comparative investigation of hydrogen in-situ charging vs. pre-charging. Int J Hydrogen Energy 2024;78:22–39. https://doi.org/10.1016/j.ijhydene.2024.06.224.
[137] Zhang C, Han Y, Teng H, Liu H, Xie C, Su Y. Enhancement of hydrogen embrittlement resistance in high manganese steel under in-situ electrochemical hydrogen charging by regulating the grain size and distribution. Int J Hydrogen Energy 2024;82:968–78. https://doi.org/10.1016/j.ijhydene.2024.08.002.
[138] Saeed-Akbari A, Imlau J, Prahl U, Bleck W. Derivation and variation in composition-dependent stacking fault energy maps based on subregular solution model in high-manganese steels. Metall Mater Trans A 2009;40:3076–90. https://doi.org/10.1007/s11661-009-0050-8.
[139] Hanson JP, Bagri A, Lind J, Kenesei P, Suter RM, Gradečak S, et al. Crystallographic character of grain boundaries resistant to hydrogen-assisted fracture in Ni-base alloy 725. Nat Commun 2018;9:3386. https://doi.org/10.1038/s41467-018-05549-y.
[140] Bechtle S, Kumar M, Somerday BP, Launey ME, Ritchie RO. Grain-boundary engineering markedly reduces susceptibility to intergranular hydrogen embrittlement in metallic materials. Acta Mater 2009;57:4148–57. https://doi.org/10.1016/j.actamat.2009.05.012.
[141] Kwon YJ, Jung SP, Lee BJ, Lee CS. Grain boundary engineering approach to improve hydrogen embrittlement resistance in Fe-Mn-C TWIP steel. Int J Hydrogen Energy 2018;43:10129–40. https://doi.org/10.1016/j.ijhydene.2018.04.048.
[142] Cheng WC, Cheng CY, Hsu CW, Laughlin DE. Phase transformation of the L12 phase to kappa-carbide after spinodal decomposition and ordering in an Fe-C-Mn-Al austenitic steel. Mater Sci Eng A 2015;642:128–35. https://doi.org/10.1016/j.msea.2015.06.096.
[143] Bartlett LN, Van Aken DC, Medvedeva J, Isheim D, Medvedeva NI, Song K. An Atom probe study of kappa carbide precipitation and the effect of silicon addition. Metall Mater Trans A 2014;45:2421–35. https://doi.org/10.1007/s11661-014-2187-3.
[144] Mou Y, Lei K, Li J, Guo X, Fan J, Hu C, et al. Recent advances in κ-carbide precipitation behavior and its influence on mechanical properties in austenite-based Fe-Mn-Al-C lightweight steels. Materials 2026;19:727. https://doi.org/10.3390/ma19040727.
[145] Timmerscheidt TA, Dey P, Bogdanovski D, von Appen J, Hickel T, Neugebauer J, et al. The role of κ-carbides as hydrogen traps in high-Mn steels. Metals (Basel) 2017;7. https://doi.org/10.3390/met7070264.
[146] Liao H, Wakeda M, Shibata A, Ohmura T. First-principles study of hydrogen segregation in ε-, η-and θ-carbides in bcc-Fe: Effects of elastic strain and local charge density. Int J Hydrogen Energy 2026;214:153715. https://doi.org/10.1016/j.ijhydene.2026.153715.
[147] Shankar RV. Some observations on the hydrogen embrittlement of Fe3Al-Fe 3AlC intermetallic compounds. Mater Res Bull 2004;39:169–74. https://doi.org/10.1016/j.materresbull.2003.10.006.
[148] Witkowska M, Chronowska-Przywara K, Kowalska J, Zielińska-Lipiec A. Microstructure and texture evolution of X85MnAl29-9 steel during aging. Materials 2024;17:5646. https://doi.org/10.3390/ma17225646.
[149] Bai S bin, Chen Y an, Liu X, Lu H hu, Bai P kang, Li D zhao, et al. Research status and development prospect of Fe–Mn–C–Al system low-density steels. Mater Res Technol 2023;25:1537–59. 10.1016/j.jmrt.2023.06.037.
[150] Breuer J, Grün A, Sommer F, Mittemeijer EJ. Enthalpy of formation of B2-Fe_{1-x} al_x and B2-$(Ni,Fe)_{1-x}Al_x$. Metall Mater Trans B 2001;32:913–8. https://doi.org/10.1007/s11663-001-0077-8.
[151] Kim SH, Kim H, Kim NJ. Brittle intermetallic compound makes ultrastrong low-density steel with large ductility. Nature 2015;518:77–9. https://doi.org/10.1038/nature14144.
[152] Yang MX, Yuan FP, Xie QG, Wang YD, Ma E, Wu XL. Strain hardening in Fe-16Mn-10Al-0.86C-5Ni high specific strength steel. Acta Mater 2016;109:213–22. https://doi.org/10.1016/j.actamat.2016.02.044.
[153] Sohn SS, Lee BJ, Lee S, Kim NJ, Kwak JH. Effect of annealing temperature on microstructural modification and tensile properties in 0.35 C-3.5 Mn-5.8 Al lightweight steel. Acta Mater 2013;61:5050–66. https://doi.org/10.1016/j.actamat.2013.04.038.
[154] Fu CL, Painter GS. First principles investigation of hydrogen embrittlement in FeAl. J Mater Res 1991;6:719–23. https://doi.org/10.1557/JMR.1991.0719.
[155] Bartlett L, Van Aken D. High manganese and aluminum steels for the military and transportation industry. JOM 2014;66:1770–84. https://doi.org/10.1007/s11837-014-1068-y.
[156] Li X, Zhang J, Fu Q, Akiyama E, Song X, Shen S, et al. Hydrogen embrittlement of high strength steam turbine last stage blade steels: Comparison between PH17-4 steel and PH13-8Mo steel. Mater Sci Eng A 2019;742:353–63. https://doi.org/10.1016/j.msea.2018.10.086.
[157] Niu M, Kong H, Zhou B, Wang W, Jiao Z. Intermetallic-precipitation-strengthened steels, Advanced Multicomponent Alloys. Materials Horizons: From Nature to Nanomaterials 2022:247–65. https://doi.org/10.1007/978-981-19-4743-8_10.
[158] Jasen PV, González EA, Luna R, Brizuela G, Juan A. The hydrogen effect in the electronic structure and bonding of the B2 FeAl alloy with a Fe vacancy. Int J Hydrogen Energy 2009;34:9591–5. https://doi.org/10.1016/j.ijhydene.2009.10.014.
[159] Fu CL, Wang X. The effect of electronic structure on the defect properties of FeAl. Mater Sci Eng A 1997;239–240:761–8. https://doi.org/10.1016/S0921-5093(97)00664-3.
[160] Zhang G, Yang F, Hu M, Liu L, Luo Z, Tang T. Nucleation and growth of H blisters in stacking fault on B2–FeAl 100 planes. RSC Adv 2017;7:43933–7. https://doi.org/10.1039/C7RA08368H.
[161] Yoo J, Jo MC, Kim DW, Song H, Koo M, Sohn SS, et al. Effects of Cu addition on resistance to hydrogen embrittlement in 1 GPa-grade duplex lightweight steels. Acta Mater 2020;196:370–83. https://doi.org/10.1016/j.actamat.2020.06.051.
[162] Lee D-H, Jung JY, Lee KH, Lee SY, Zhao Y, Lau KB, et al. Distinct effects of in-situ and ex-situ hydrogen charging methods on the mechanical behavior of CoCrFeNi high-entropy alloy fabricated by laser-powder bed fusion. J Alloy Compd 2023;940:168858. https://doi.org/10.1016/j.jallcom.2023.168858.
[163] Lee SI, Lee JM, Lee SY, Kim HJ, Suh JY, Shim JH, et al. Tensile and fracture behaviors of austenitic high-manganese steels subject to different hydrogen embrittlement test methods. Mater Sci Eng A 2019;766. https://doi.org/10.1016/j.msea.2019.138367.
[164] Yun HS, Jeon SK, Lee Y-K, Park JS, Nahm SH. Effect of precharging methods on the hydrogen embrittlement of 304 stainless steel. Int J Hydrogen Energy 2024; 50:175–88. https://doi.org/10.1016/j.ijhydene.2023.09.073.

[165] Zhao Y, Park JM, Lee DH, Song EJ, Suh JY, Ramamurty U, et al. Influences of hydrogen charging method on the hydrogen distribution and nanomechanical properties of face-centered cubic high-entropy alloy: a comparative study. Scr Mater 2019;168:76–80. https://doi.org/10.1016/j.scriptamat.2019.04.025.
[166] Lee SY, Hwang B. Hydrogen embrittlement of three high-manganese steels tested by different hydrogen charging methods. J Korean Inst Met Mater 2017;55:695–702. https://doi.org/10.3365/KJMM.2017.55.10.695.
[167] Shin SH, Oh DK, Kim SG, Hwang B. Notch tensile behavior of 304L and 316L stainless steels under in-situ and ex-situ electrochemical hydrogen charging. J Mater Res Technol 2025;36:9158–67. https://doi.org/10.1016/j.jmrt.2025.05.132.
[168] Mao LY, Luo ZA, Huang C, Zhou HY, Zhang XM. Exploring the hydrogen embrittlement behavior in nickel-economized austenitic stainless steel: investigating the role of manganese in modifying hydrogen-induced crack mechanisms. Corros Sci 2024;226:111691. https://doi.org/10.1016/j.corsci.2023.111691.
[169] Chen L, Lee S-J, De Cooman BC. Mechanical properties of H-charged Fe–18Mn–1.5Al–0.6C TWIP steel. ISIJ Int 2012;52:1670–7. https://doi.org/10.2355/isijinternational.52.1670.
[170] Lee S-M, Park I-J, Jung J-G, Lee Y-K. The effect of Si on hydrogen embrittlement of Fe-18Mn-0.6C-XSi twinning-induced plasticity steels. Acta Mater 2016;103:264–72. https://doi.org/10.1016/j.actamat.2015.10.015.
[171] Khedr M, Li W, Zhu X, Zhou P, Gao S, Jin X. Improving hydrogen embrittlement resistance of Hadfield steel by thermo-mechanical flash-treatment. Mater Sci Eng A 2018;712:133–9. https://doi.org/10.1016/j.msea.2017.11.036.
[172] Bai Y, Tian Y, Gao S, Shibata A, Tsuji N. Hydrogen embrittlement behaviors of ultrafine-grained 22Mn–0.6C austenitic twinning induced plasticity steel. J Mater Res 2017;32:4592–604. https://doi.org/10.1557/jmr.2017.351.
[173] Bal B, Koyama M, Gerstein G, Maier HJ, Tsuzaki K. Effect of strain rate on hydrogen embrittlement susceptibility of twinning-induced plasticity steel pre-charged with high-pressure hydrogen gas. Int J Hydrogen Energy 2016;41:15362–72. https://doi.org/10.1016/j.ijhydene.2016.06.259.
[174] Murakami Y, Kanezaki T, Mine Y. Hydrogen effect against hydrogen embrittlement. Metall Mater Trans A 2010;41:2548–62. https://doi.org/10.1007/s11661-010-0275-6.
[175] Zhao C, Deng L, Wu S, Wu W, Peng Y, Wang X, et al. Dual role of hydrogen in fatigue life of 316L austenitic stainless steel. Int J Fatigue 2025;198:108975. https://doi.org/10.1016/j.ijfatigue.2025.108975.